Investigation of transition to turbulence at low Reynolds numbers using Implicit Large Eddy Simulations with a Discontinuous Galerkin method

by

Alejandra Uranga

B.S., Florida Institute of Technology (2004)
M.A.Sc., University of Victoria, BC, Canada (2006)

Submitted to the Department of Aeronautics and Astronautics
in partial fulfillment of the requirements for the degree of

Doctor of Philosophy

at the

MASSACHUSETTS INSTITUTE OF TECHNOLOGY

February 2011

Author .....
Department of Aeronautics and Astronautics
September 30, 2010

Certified by .....
Jaime Peraire
Professor of Aeronautics and Astronautics
Thesis Supervisor

Certified by .....
Mark Drela
Terry J. Kohler Professor of Fluid Dynamics
Thesis Supervisor

Certified by .....
Per-Olof Persson
Assistant Professor of Mathematics
University of California, Berkeley
Thesis Committee

Accepted by .....
Eytan H. Modiano
Associate Professor of Aeronautics and Astronautics
Chair, Department Committee on Graduate Students

Investigation of transition to turbulence at low Reynolds numbers using Implicit Large Eddy Simulations with a Discontinuous Galerkin method

by

Alejandra Uranga

Submitted to the Department of Aeronautics and Astronautics
on September 30, 2010, in partial fulfillment of the
requirements for the degree of
Doctor of Philosophy

Abstract

The present work predicts the formation of laminar separation bubbles at low Reynolds numbers and the related transition to turbulence. In addition to being one of the first Implicit Large Eddy Simulation studies using a high-order Discontinuous Galerkin method, unique attention is given to the boundary layer characteristics thus contributing to the understanding of low Reynolds number flows and the related separation-induced transition. Furthermore, a preliminary transition model suitable for such flows is introduced and its underlying concept proven valid.

The flow around an SD7003 infinite wing at an angle of attack of 4° is first considered at Reynolds numbers of 10,000, 22,000, and 60,000. At the lowest Reynolds number studied, the flow remains laminar and two dimensional with a periodic vortex shedding. For higher Reynolds numbers, the flow is highly unsteady and exhibits a separation bubble on the upper surface over which flow transitions to turbulence. Tollmien-Schlichting waves are observed in the boundary layer upstream of separation, and their streamwise amplification factor shows they are responsible for transition.

The major effects of cross-flow on low Reynolds number transition are studied by comparing the flows over the same infinite wing at different sweep angles. Projecting the results along a common two-dimensional equivalent direction, it is established that the cross-flow *cannot* be decoupled from the streamwise evolution at intermediate sweep angles due to strong non-linear interactions that take place after the laminar boundary layer separates. Hence, for separation-induced transition at low Reynolds numbers, it is not possible to treat streamwise and cross-flow instabilities independently for wings with sweep angles between about 10° and 40°, and predicting the mixed transition cannot be reduced to treating the disturbances of each component separately. An important presumption to be adopted in the study of unsteady flows for MAVs and animal locomotion is thus that the type of transition (TS dominated, cross-flow dominated, or mixed) is *a priori* unknown as soon as the flow is slightly misaligned with the wing's chord.

Thesis Supervisor: Jaime Peraire
Title: Professor of Aeronautics and Astronautics

Thesis Supervisor: Mark Drela
Title: Terry J. Kohler Professor of Fluid Dynamics

to uncertainty

"I am an old man now, and when I die and go to heaven there are two matters on which I hope for enlightenment. One is quantum electrodynamics, and the other is the turbulent motion of fluids. And about the former I am rather optimistic."

Horace Lamb, 1932 address to the British Association for the Advancement of Science

Acknowledgments

I came to Cambridge and to MIT for the challenge and the enrichment brought on by change. There have been ups and downs, frustrations and achievements, thrilling moments and drowning feelings, but above all I have found a sense of fulfillment—not only intellectually. I have also had the immense pleasure of getting to know some amazing people and sharing part of their lives.

My gratitude goes to Jaime Peraire for his teachings, encouragements, and for relating to me as a whole and independent human being; your energy, interest, and good humor have made this period of my life a great one. You have been the greatest advisor I could have had, an unwavering mentor, and a close friend.

The research co-supervision and classroom teachings of Mark Drela have made me a more balanced thinker and greatly enhanced both my understanding and intuition of aerodynamics; your contribution to my work has been invaluable. Your enthusiasm for all that you do is contagious, and I am thankful for the chance of being close by.

This numerical work owes a lot to Per-Olof Person, the main developer of the computational code. Thank you for your great contributions to my understanding of all things numerics, and for always being available to share your views and skepticism.

The present thesis greatly benefited from the valuable comments of my readers, David Darmofal and Youssef Marzouk. I would like to thank David in particular for his thoroughness and the fruitful discussions around the writing of this document.

I would like to acknowledge the financial support provided by the Air Force Office of Scientific Research under the Multi-University Research Initiative "Biologically Inspired Flight." I am also thankful for the scholarship provided by Mexico's National Council for Science and Technology (CONACYT). This research was supported in part by the National Science Foundation through TeraGrid resources provided by the Texas Advanced Computing Center, the National Center for Supercomputing Applications, and the Louisiana Optical Network Initiative. It also used the Lawrencium computational cluster resource provided by the IT Division at the Lawrence Berkeley National Laboratory (supported by the Director, Office of Science, Office of Basic Energy Sciences, of the U.S. Department of Energy under Contract No. DE-AC02-05CH11231) as well as resources of the National Energy Research Scientific Computing Center (supported by the Office of Science of the U.S. Department of Energy under Contract No. DE-AC03-76SF00098).

Throughout my teaching assistance experiences, I learned from the eagerness of the students and from every single one of their questions: this might sound strange, but they have taught me a lot, and in some ways more than I taught them. At the same time, I was extremely fortunate to work with Tony Patera, who taught me by example how to teach with particular care and dedication.

Many thanks go to my colleagues and friends, Josh Krakos and Jeff Chambers, for helping make my experience through quals such a memorable one. I am also indebted to the people in and around my lab for sharing knowledge and thoughts about matters both related and unrelated to work, in particular Hemant Chaurasia, Pritesh Mody, and David Willis.

While my work (research, classes, teaching) has been my life for the past years, my life is not my work. I thank Emily Israeli for her cheerfulness and firm presence throughout and beyond my first years here. Britt Bille Rasmussen has been here in some of the best and some of the worst moments, and for her unyielding friendship and character I am most grateful. I would not have made it through it all without the support of Amy: you taught me in your own way what caring takes, what integrity makes, and the meaning of the word trust; thank you for so bluntly believing in me and sticking through it all.

Finally, I wish to thank what cannot be acknowledged. I would not have wanted to go thought it all without Julien; we have grown together and yet managed to remain independent. One of the greatest satisfactions throughout my life has been to walk the roads with you, not out of necessity but out of pleasure.

Contents

List of Figures

List of Tables

Nomenclature

Letters

c	Wing chord
C_D	Drag coefficient
C_f	Chord-wise skin friction coefficient
C_L	Lift coefficient
C_p	Pressure coefficient
E	Total energy per unit mass
H	Two-dimensional equivalent shape factor, $H = \delta^*/\theta$
H_{11}	Streamwise boundary layer shape factor, $H_{11} = \delta_1^*/\theta_{11}$
n	Local normal coordinate, *i.e.* perpendicular to the wing's surface
$\hat{n}$	Local normal unit vector, *i.e.* perpendicular to the wing's surface
n_e	Boundary layer edge location, *i.e.* distance from the wall to the boundary layer edge
N	Amplification factor of boundary layer disturbances
N_1	Streamwise amplification factor
N_2	Cross-flow amplification factor
p	Static pressure
Pr	Prandtl number, $Pr = \mu\, c_p/\kappa$
q	Q-criterion
Re	Reynolds number based on chord and free-stream speed, $Re = U_\infty c/\nu$
$\hat{s}_1$	Local boundary layer streamwise unit vector, $\hat{s}_1 = \vec{u}_e^*/u_e$
$\hat{s}_2$	Local boundary layer cross-flow unit vector, $\hat{s}_2 = \hat{s}_1 \times \hat{n}$
t	Physical time
t^*	Non-dimensional time, $t^* = t\, U_\infty/c$
U_∞	Free-stream flow speed
$\vec{u}$	Flow velocity
$\vec{u}^*$	Boundary layer pseudo-velocity

$\vec{u}_e^*$	Boundary layer edge pseudo-velocity
u_e	Boundary layer edge pseudo-velocity magnitude, $u_e = \lvert\vec{u}_e^*\rvert$
u_1	Boundary layer streamwise pseudo-velocity
u_2	Boundary layer cross-flow pseudo-velocity
u_i	Velocity component in direction x_i
u_τ	Wall-friction velocity, $u_\tau = \sqrt{\tau_w/\rho}$
x_i	Computational coordinate i
x_r	Reattachment location
x_{sep}	Separation location
x_{tr}	Transition location
x	Chord-wise direction
y	Span-wise direction
z	Direction perpendicular to the chord-wise and span-wise directions

Symbols

α	Angle of attack
γ	Fluid specific heat ratio
δ	Boundary layer thickness
δ^*	Two-dimensional equivalent boundary layer displacement thickness
δ_1^*	Streamwise boundary layer displacement thickness, $\int_0^{n_e} (1 - u_1/u_e)\, dn$
δ_2^*	Cross-flow boundary layer displacement thickness, $\int_0^{n_e} (0 - u_2/u_e)\, dn$
Δt	Physical time step
Δt^*	Non-dimensional time step, $\Delta t^* = \Delta t\ U_\infty/c$
θ	Two-dimensional equivalent boundary layer momentum thickness
θ_{11}	Streamwise boundary layer momentum thickness, $\int_0^{n_e} (1 - u_1/u_e)\, u_1/u_e\, dn$
θ_{ij}	Boundary layer momentum thickness tensor, $\int_0^{n_e} (u_{e_i}/u_e - u_i/u_e)\, u_j/u_e\, dn$
Λ	Wing sweep angle
μ	Dynamic viscosity coefficient
ν	Kinematic viscosity coefficient, $\nu = \mu/\rho$
ρ	Fluid density
τ_w	Wall shear stress, $\tau_w = {}^1\!/_2\, \rho\, U_\infty^2 C_f$
$\vec{\omega}$	Flow vorticity, $\vec{\omega} = \nabla \times \vec{u}$

Subscripts

1	In the streamwise direction, *i.e.* in the local direction of the inviscid stream-line at the boundary layer edge
2	In the cross-flow direction, *i.e.* in the direction perpendicular to both the streamwise direction and the normal to the foil
c	In the span-wise direction
i	In the direction i
r	Reattachment
sep	Separation
tr	Transition
x	In the chord-wise direction
y	In the span-wise direction, *i.e.* along the leading edge line
∞	Relative to the free-stream direction

Acronyms

CF	Cross-flow
CFD	Computational Fluid Dynamics
DG	Discontinuous Galerkin
DNS	Direct Numerical Simulation
ILES	Implicit Large Eddy Simulation
KH	Kelvin-Helmholtz
LES	Large Eddy Simulation
LSB	Laminar separation bubble
MAV	Micro-Air Vehicle
RANS	Reynolds-Averaged Navier-Stokes
TS	Tollmien-Schlichting

Chapter 1

Introduction

Interest in autonomous Unmanned Air Vehicles (UAVs), particularly Micro-Air Vehicles (MAVs[1]), has grown considerably in the last decades stimulated by the miniaturization of technology and the advancements in micro systems. The use of MAVs is especially attractive for law-enforcement and military applications, such as reconnaissance, surveillance and rescue missions.

The recent years have also seen a growing interest in animal locomotion. The physics of fish swimming, birds flying, and insects flapping has been studied both by engineers and by biologists, and the trend is to go beyond qualitative explanations by seeking a more quantitative understanding of the phenomena involved. As for MAVs, the flow falls in the so-called low Reynolds number regime, with Reynolds numbers between 10,000 and 100,000 (Shyy, 2008). Animal locomotion is interesting from the point of view of design of small flying vehicles, and also from a fundamental physics and engineering perspective. Design strategies can be inspired by nature, even when the aim is not to reproduce the exact flight of an animal. Furthermore, the field of fundamental fluid mechanics can benefit from the study of the complex flows involved.

1.1 Motivation

At the low Reynolds numbers encountered in MAVs and animal locomotion, the boundary layer over the body remains laminar over large distances and is thus prone to separation, a phenomenon which is detrimental to aerodynamic performance. Computational design strategies for low Reynolds number flying and swimming vehicles,

[1] An MAV was formally defined by the Defense Advanced Research Projects Agency (DARPA) as any flying vehicle whose dimensions are no larger than 15cm. In general, they weigh a couple hundred grams.

as well as for model airplane and glider design, hence rely on the accurate prediction of separation. Furthermore separation often induces transition to turbulence, which in turn can induce re-attachment. Separation, transition, and reattachment can take place over a significantly short distance, producing a separation bubble which can fluctuate in size and position. Thus, the prediction of separation and transition is of crucial importance in low Reynolds number flows.

This is very different from large-airplane aerodynamics in which the boundary layer transitions very close to the leading edge, and hence the location of predicted transition has little effect on the overall performance of the airfoil or wing under consideration. However, the computational drag prediction of high Reynolds number flows for wing and airplane design has been found to fail significantly for configurations where flow separation is present, even in small, limited regions. This has been observed during the Drag Prediction Workshop series (Lalin et al., 2005; Vassberg et al., 2008) and similar efforts. Thus, the ability to predict separation and the associated transition is fundamental for the advancement of Computational Fluid Dynamics (CFD) techniques, for both low and high Reynolds number applications.

There are widely accepted ways of predicting fully laminar and fully turbulent flows that are commonly used for design purposes, in particular methods that rely on the Reynolds-Averaged Navier-Stokes (RANS) equations and associated turbulence closure models. On the other hand, there is no single reliable, computationally affordable, way of simulating transition. While methods such as Direct Numerical Simulation (DNS) and Large Eddy Simulation (LES) are capable of accurately predicting transition, they are still too expensive to be used for design purposes and will remain so for still several decades (Spalart, 2009). Thus, a general, and practical, way of predicting transition in the RANS context is much needed.

Motivated both by newer, low Reynolds number design requirements and by the limitations of classical aerodynamic predictions, the research community is now looking for reliable ways of predicting transition. Not limited to external flow problems, there has also been significant interest from the turbo-machinery community.

As pointed out by Abu-Ghannam and Shaw (1980), transition to turbulence is a complex physical process influenced by a variety of factors, including the flow Reynolds and Mach numbers, free-stream turbulence, pressure gradient, and surface characteristics (roughness, curvature, temperature). It is thus particularly difficult to model transition for a wide variety of flows.

From another point of view, the prediction of low Reynolds number flows around MAVs and vehicles inspired by fish swimming, or the flapping flight of bats, represents

a significant challenge for CFD. The flows encountered are highly unstable, with laminar, transitional, and turbulent regions. Furthermore, transition can occur not only along boundary layers, but also along free shear layers as when separation is present.

1.2 Approach

An in-depth investigation of the low Reynolds number, low Mach number flow around a rectangular, infinite, SD7003 wing at an angle of attack of 4° is carried out. The SD7003 profile is chosen since it is characterized by the formation of a laminar separation bubble along its upper surface which is present across a range of Reynolds numbers and angles of attack, and has been the subject of several studies.

First, the flow at Reynolds numbers of 10,000, 22,000, and 60,000 is studied with a free-stream velocity vector that lies in the plane of the SD7003 profile. Thus, the free-stream is perpendicular to the wing's leading-edge line and an un-swept wing is simulated. The lowest velocity regime represents a flow that remains laminar along the wing, while the two latter are characterized by transition along a laminar separation bubble. Except at $Re = 22,000$, extensive experimental data and numerical simulations are available for comparison. In the second part, a span-wise velocity component is added to the free-stream velocity in order to simulate a wing at different sweep angles and study transition in the presence of cross-flow instabilities.

In all cases, both the general flow features (force time histories, vortex shedding, average pressure and skin friction) and the transition process are examined. Furthermore, the evolution of boundary layer disturbances and their amplification is obtained from both classical stability analysis by tracking velocity fluctuations, and as predicted by a transition model that we propose and which is based on a transport equation for the amplification factor N of disturbances.

The accurate simulation of transition to turbulence requires low numerical dispersion and dissipation. Thus, the use of a high-order Discontinuous Galerkin (DG) finite element method is used since it combines high accuracy with unstructured grids for the geometric flexibility required by practical applications.

Furthermore, several studies have shown that transition can be predicted by means of Large Eddy Simulations (LES) (see for instance Zang et al., 1993). We follow the Implicit LES (ILES) approach in which the unresolved small eddies are accounted for by means of numerical dissipation: no subgrid-scale model is employed and the full (unfiltered) compressible Navier-Stokes equations are solved. This approach has

been successfully used by Visbal and collaborators (Galbraith and Visbal, 2008; Visbal et al., 2009; Garmann and Visbal, 2009; Visbal, 2009) using a sixth-order compact difference method for the simulation of the flow around an SD7003 airfoil. To the author's knowledge, together with preliminary results presented earlier (Uranga et al., 2009), the present investigation is the first attempt at using a DG method for unsteady, three-dimensional Large Eddy Simulations.

1.3 Scope

As motivated previously, the present work focuses on two important aspects related to low Reynolds number flows which require further understanding, namely the transition mechanism and related problem of transition prediction, and the feasibility of numerical simulations to predict the flows involved.

With respect to the latter, the high-order DG method is used and expanded for the simulation of transitional and turbulent flows, and the feasibility of an ILES approach for flow simulations using a DG method is confirmed. Not all numerical methods provide the adequate dissipation (see Appendix C and Grinstein et al., 2007b), and the ILES approach needs to be evaluated given the intrinsic numerical dissipation of the particular DG method employed. Thus, a major question addressed in the present work is whether DG can provide a reliable (*i.e.* accurate and robust) test-base for transition modeling calibration and testing.

We also evaluate the accuracy that can be obtained using a number of degrees-of-freedom that is at least close to acceptable for design computations, in particular whether the boundary layer can be resolved with sufficient accuracy for stability analysis. In other words, to be suitable for use in design, the simulation technique should not require the resolution of the details of the flow phenomena involved in transition, and yet be able to predict the location of transition with sufficient accuracy. This is assessed by closely looking at the transition process and the required spatial and temporal resolutions.

The second major objective of the present work is to advance towards the development of a transition modeling approach suitable for design. The knowledge of the fundamental flow physics encountered at these regimes is still quite limited, and hence the development of a transition prediction method for low Reynolds number flows is necessarily accompanied by a study and an understanding of the fundamental flow phenomena involved, such as the formation of laminar separation bubbles and the mechanisms involved in the transition to turbulence. Thus, the present work includes

a study of the transition which takes place along a laminar separation bubble in low Reynolds number flows. In particular, we investigate the effects of the cross-flow present over swept wings in this regime which are for the most part unknown.

The aim is not to fully understand every aspect of separation-induced transition, but to know enough to determine which features play the most prominent role and hence need to be properly incorporated in any successful transition model. Once that is done, we evaluate the applicability of a transition model for unsteady, three-dimensional flow proposed by M. Drela[2] which uses a transport equation for the linear amplification factor N of disturbances and amounts to a generalization of the two-dimensional, steady procedure used in XFOIL (Drela, 2002). It is designed to model the amplification of Tollmien-Schlichting (TS) waves, and as such assumes they are the dominant mechanism of transition—which the present work establishes to be the case in separation-induced transition at low Reynolds numbers over unswept wings. The N evolution is evaluated *a posteriori* using a time-average of the unsteady ILES simulations as the mean base flow.

The TS transition model does not directly take into account the growth of cross-flow instabilities and hence considering the flow for several wing sweep angles is done in order to eventually devise simple modifications to the model equation that would take into account the influence of cross-flow on transition. Modifying the transition model equation is however outside the scope of the present research, as is the actual coupling with a RANS transition model.

The proposed transition equation is compatible with turbulence models for RANS closure commonly used today via either a trip term, or via a limiting function for the turbulent production terms. However, its implementation in an unstructured code constitutes a challenge in itself since it relies on boundary layer integral parameters which need to be computed. We determine which thresholds are appropriate (*e.g.* to define the boundary layer edge), and which boundary layer resolution and integration accuracy is needed.

In what follows, the reader is first introduced to the background considerations relevant to the present study while a detailed summary of the works reported in the published literature is provided. The methodology chapter describes the computational methods employed including how the boundary layer and transition process are studied, and gives the form of the transition model equation proposed. The next two chapters discuss the results for an un-swept wing at three different Reynolds numbers, followed by those for wings with varying sweep angles at Reynolds 60,000. Finally,

[2]personal communication, fall 2006

a summary of results and contributions are presented together with avenues for further work. Additional considerations which might be of interest to some readers are provided in the appendices.

Chapter 2

Background

This chapter is devoted to providing a summary of the published works that are related to our problem and to the research objectives. The aim is also to give an overview of the relevant physical and numerical aspects of the present research. This knowledge constitutes the basis for the understanding of the present work's motivation, challenges, and contributions.

We start by giving a description of transition and of flow stability theory, before looking at the specifics of transition in laminar separation bubbles and the effects of cross-flow. This is followed by a review of the different transition prediction techniques that have been reported in the literature. Some fundamental aspects of the Large Eddy Simulation approach are then reviewed, before describing work that has been done in turbulence and transition prediction using Discontinuous Galerkin methods. Finally, an overview of published research results on the low Reynolds number flow around SD7003 airfoils and wings is provided.

2.1 The Physics of Transition to Turbulence

Transition to turbulence significantly modifies the major characteristics and behavior of a flow. For instance, turbulent flows generate larger wall friction than laminar flows due to the increased momentum transfer and dissipation. On the other hand, a laminar boundary layer has a much greater tendency to separate in the presence of an adverse pressure gradient than its turbulent counterpart. Thus, a very important—and mostly unresolved—problem in fluid mechanics is that of transition. Under what circumstances does a laminar flow become turbulent? Where, or at what moment, does transition take place? What physical mechanisms are responsible for transition?

Throughout this work, we are careful to differentiate between the *critical* Reynolds number and the *transition* Reynolds number. The latter refers to the location where the flow becomes turbulent, which is what is generally measured in experiments; it corresponds to what we call here transition location. The former on the other hand refers to the location where the flow first becomes unstable, and is usually determined by a stability analysis. The difference between these two values is the transition length which can vary significantly between flows.

2.1.1 Stages of Transition

The textbooks by Schlichting and Gersten (2000) and by White (1991) describe in detail the stages of transition along a flat plate boundary layer in low free-stream turbulence, as illustrated in Figure 2-1. The first stage starts at the critical Reynolds number and corresponds to the development of unstable two-dimensional Tollmien-Schlichting (TS) waves which travel in the mean flow direction and are amplified as they move downstream. The onset and development of these waves is the object of primary stability theories. Further downstream, the TS waves become three-dimensional and the flow starts showing span-wise variations. This is accompanied by the formation of vortical structures, called Λ structures, whose development is studied by secondary stability theory. The development of three-dimensional waves is followed by the appearance of turbulent spots, and starting at this location the flow becomes alternatively laminar and turbulent, a phenomena called *intermittency*. The turbulent spots convect downstream, disperse, coalesce, and eventually encompass all of the boundary layer at the transition Reynolds number: the boundary layer is then fully turbulent.

The above description corresponds to the process of *natural transition*, which is most commonly observed in external flows over smooth walls and with low free-stream turbulence. Another type of boundary layer transition is known as *bypass transition*, and is usually observed in internal gas turbine flows that are characterized by high levels of free-stream turbulence (turbulence intensity of 0.5% or more). In this case, the linear instability region is by-passed without the appearance of linearly growing TS waves, and transition is achieved as soon as the local Reynolds number is high enough to allow turbulent flow.

Among the factors that most strongly influence transition are the free-stream turbulence, the wall roughness, and the pressure gradient. The presence of either free-stream turbulence or wall roughness introduces perturbations into the boundary

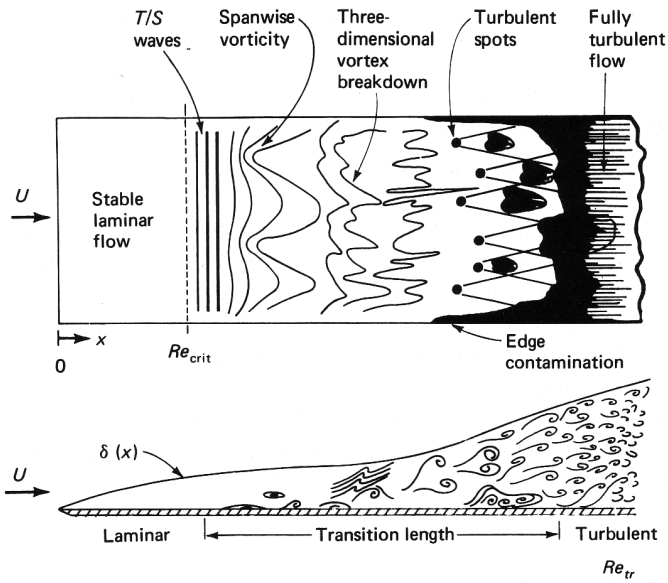

Figure 2-1: Illustration of the flat plate boundary layer transition process [Figure from White (1991)]

layer and hence tends to induce transition. Certain disturbances are more efficient than others at triggering transition, a phenomena known as boundary layer *receptivity* (Saric et al., 2002).

In the presence of a favorable pressure gradient (pressure decrease), the flow is accelerated and the transition location moves downstream. On the other hand, an adverse pressure gradient (pressure increase) decelerates the flow and destabilizes the boundary layer thus inducing transition at lower Reynolds numbers. If the pressure gradient is large enough (*e.g.* as measured relative to the boundary layer inertia), the boundary layer can separate before transition takes place. This can occur for instance at low Reynolds numbers, and is discussed in Section 2.3; in this case transition is very rapid, with little or no turbulent spot formation (LeBlanc et al., 1989).

2.1.2 Transition in Three-Dimensional Boundary Layers

The flow around a swept wing is an example of flow in which transition can take place along a three-dimensional boundary layer. In addition to the transition process corresponding to the growth of TS waves in essentially two-dimensional flows, transition in three-dimensional cases can be triggered by cross-flow (CF) instabilities. The CF waves travel in a direction which is close to orthogonal to the streamwise direction, *i.e.* almost span-wise. A phenomena often encountered is the appearance of standing perturbation vortices, also called zero-Hertz modes due to the fact that they have

zero angular frequency and hence are stationary. Section 2.4 provides more details.

Thus, transition can occur due to the growth of TS wave, CF instabilities, or a combination of both known as mixed transition. Both TS-type and CF-type transitions can be modeled by tracking the amplification factor of the disturbances (see summary of previous works in Section 2.5.2), but the non-linear interaction of TS and CF instabilities at the later stages of growth close to transition is not well understood. Furthermore, very little is known about the effects of cross-flow on transition at low Reynolds numbers, a deficiency the present works starts to address.

2.2 Mathematical Description: Stability Theory

It is important to be aware that stability theory does not try to establish when the flow actually becomes turbulent. Rather, it aims at determining whether small perturbations would grow, which is a necessary condition for transition. The discussion in this section is mainly based on the books by Schlichting and Gersten (2000); White (1991); Drazin and Reed (1981); and Cebeci (2004).

The first attempts at applying stability considerations to fluid flows date back to the late eighteen hundreds and the theoretical studies of Kelvin (1871) and Rayleigh (1879, 1880), at which time stability methods were already used to assess the stability of dynamical systems of rigid bodies. The idea is to add a small perturbation into a known solution of the equations of motion, neglect products of small perturbations to obtain a linear system, assume the perturbations can be expressed as a linear superposition of independent time-evolving modes of the form e^{st}, and calculate the complex variable s from the linearized equations. The system is then *unstable* when the real part of s of *any* mode is positive indicating exponential growth of an infinitesimal disturbance. On the other hand, if *all* the disturbances die away (s having a negative real part), the system is considered *stable*.

Note that the small perturbation assumption of stability theory, by which quadratic terms in the perturbation quantities can be neglected and hence the governing equations linearized, is justified by the fact that the first perturbations that appear on a (perfectly) laminar flow are necessarily small.

2.2.1 Primary (Linear) Stability Theory

In primary stability theory, the starting point is a basic flow which is laminar and satisfies the governing Navier-Stokes equations. A small, two-dimensional perturbation

is superimposed on this basic flow, and the governing equations linearized.

It is also assumed that the basic flow is steady and *parallel*, *i.e.* the only non-vanishing velocity component U (in the direction x) is only a function of the transverse direction (*e.g.* the direction n normal to the wall). The parallel flow assumption is exact for fully developed flows inside ducts of constant cross-section, and a good approximation for boundary layers in which x-derivatives are negligible compared to n-derivatives.

In order to satisfy the continuity equation, a perturbation stream function $\psi(x, n, t)$ is defined such that the flow disturbances u', v' introduced into the basic laminar flow $U(n)$ are given by

$$u' = \frac{\partial \psi}{\partial n} \quad , \quad v' = -\frac{\partial \psi}{\partial x} \ . \tag{2.1}$$

The perturbations are assumed to be the superposition of independent eigenmodes of the form

$$\psi(x, n, t) = \phi(n)\, e^{i(\alpha x - \omega t)} \ , \tag{2.2}$$

in which $\phi(n)$ is the eigenfunction, α or ω the eigenvalue, and the exponent term the amplitude function. Here we choose to approach the problem from the point of view of temporal stability to determine whether the small disturbances grow or decay in time. Thus, the parameter α is real and the perturbation wavelength of the mode is $\lambda = 2\pi/\alpha$. The complex parameter $\omega = \omega_r + i\,\omega_i$ describes the frequency ω_r and the amplification factor ω_i of the mode. Thus, the amplitude of the temporal mode is $e^{\omega_i t}$ and the perturbation wave is damped (stable) when $\omega_i < 0$ and amplified (unstable) when $\omega_i > 0$. It is convenient to introduce a third parameter, $c = \omega/\alpha = c_r + i\,c_i$, which characterizes the phase velocity c_r in the x-direction.

This whole procedure (detailed in Appendix B) yields the Orr-Sommerfeld equation which can be non-dimensionalized by taking the boundary layer edge velocity U_e as the characteristic velocity, and some measure of the boundary layer thickness d (usually the displacement thickness δ^*) as the characteristic length, to give

$$(U - c)\left(\phi'' - \alpha^2\phi\right) - U''\phi = -\frac{i}{\alpha Re}\left(\phi'''' - 2\alpha^2\phi'' + \alpha^4\phi\right) \ , \tag{2.3}$$

where $Re = U_e\, d\,/\,\nu$ is the characteristic Reynolds number and the prime indicates derivatives with respect to n.

The corresponding boundary conditions for a boundary layer are given by the no-slip condition at the wall located at $n = 0$, and the vanishing of disturbances infinitely far from the wall. Both of these conditions translate into vanishing perturbation

velocities, that is

$$\phi = 0 \ , \ \phi' = 0 \quad \text{at} \quad n = 0 \ , \ n \to \infty \ . \tag{2.4}$$

The Orr-Sommerfeld equation (2.3) was derived by Orr (1907) and Sommerfeld (1908) and is the starting point of the stability theory of laminar parallel flows. Together with its homogeneous boundary conditions it forms an eigenvalue problem, with parameters α, c, Re, and eigenfunctions $\phi(n)$. Solving the stability problem corresponds to finding the solutions of this equation and thus determining whether the amplification factor ω_i is positive (unstable flow) or negative (stable flow).

Temporal versus Spatial Stability

The Orr-Sommerfeld equation can be solved for the temporal growth (in temporal stability theory) to determine ω, or for the spatial growth (spatial stability theory) to determine α. In the former, α is taken to be real and ω is complex, and the amplitude of the disturbances grows in time as $e^{\omega_i t}$ (*i.e.* instability when $\omega_i > 0$). In the latter, ω is taken to be real and α complex, and the disturbance amplitude varies with x as $e^{-\alpha_i x}$ (*i.e.* instability when $\alpha_i < 0$).

Gaster (1962) compared the amplification rates for disturbances growing in time to disturbances growing spatially for the same wave number, and showed that for small amplification rates both spatially-growing and temporally-growing frequencies are equal to a high order approximation. In other words, the temporally- and spatially-evolving disturbances are equivalent, and one can choose either approach to study the stability of linear modes.

Inviscid Stability

When the Reynolds number becomes infinitely large, the flow is inviscid and the Orr-Sommerfeld equation (2.3) simplifies to the second order equation

$$(U - c)\left(\phi'' - \alpha^2 \phi\right) - U''\phi = 0 \ , \tag{2.5}$$

or equivalently, for $c \neq U$,

$$\phi'' - \left(\frac{U''}{U - c} + \alpha^2\right)\phi = 0 \ , \tag{2.6}$$

which is known as the Rayleigh equation as a reference to Lord Rayleigh who first studied it (Rayleigh, 1879, 1880), and can be solved analytically for some simple

$U(n)$ profiles. For an external flow, the boundary conditions impose $v' = 0$ at the wall (non-penetration) and the unperturbed far-field, *i.e.* $\phi = 0$ at $n = 0$ and $n \to \infty$.

Here, we limit ourselves to giving some fundamental conclusions of inviscid stability that are useful in the understanding of the cases studied in the present work. For a detailed discussion of inviscid stability, see Drazin and Reed (1981).

In an inviscid flow, the velocity profile must have an inflection point for it to be unstable (Rayleigh, 1879, 1880): this necessary condition for inviscid stability is known as the point of inflection criterion. In the presence of an adverse pressure gradient, a boundary layer profile has an inflection point and can be unstable, while it is inviscidly stable in favorable pressure gradients (Schlichting and Gersten, 2000). At this point it is important to note that stability is closely related to the curvature of a velocity profile. Therefore, in order to make correct stability predictions, both the velocity profile $U(n)$ and its curvature $U'' = d^2U/dn^2$ must be known accurately.

Similarly, free shear layers between parallel streams can be inviscidly unstable: this is known as Kelvin-Helmholtz instability—named after Helmholtz (1868) who first observed the phenomena and after Kelvin (1871) who solved the associated stability problem. It is observed in the presence of two streams with same velocity and different densities when the fluid on top has higher density than the fluid below, or at the interface of two streams of same density but different velocities as occurs for instance in viscous flows with a vorticity gradient (see Drazin and Reed (1981) for the mathematical derivations). Of particular interest to us is when this instability occurs after a boundary layer separates.

Viscous Stability

While the study of the stability of inviscid flows led early to significant results, progress in understanding viscous flows was much slower. For instance, it was assumed since Rayleigh's work and for a long time that any velocity profile without an inflection point was stable (a legacy of the point of inflection criterion), and viscous cases such as channel flow and boundary layers in favorable pressure gradients were deemed stable. It was only 40 years later that Prandtl (1921) showed that viscosity could have a destabilizing effect, and the analytical study of the Orr-Sommerfeld equation was performed shortly after by his students Tollmien (1929) and Schlichting (1933). It took yet more than another decade for the results of stability theory to be verified experimentally, when H.L. Dryden and his co-workers at the National Bureau of Standards were able to observe TS waves. Numerical solutions of the Orr-

Sommerfeld equation were obtained only in the 1960s and 1970s (Kurtz and Candrall, 1962; Kaplan, 1964; Wazzan et al., 1968; Jordinson, 1970, 1971).

The main result of viscous stability analysis is that viscosity can have both a stabilizing effect (when viscosity damps disturbances) and a destabilizing one (as in the case of a boundary layer with no inflection point whose velocity profile is inviscidly stable but viscously unstable). Thus

- the flow is stable when it is very viscous, *i.e.* below the critical Reynolds number Re_{crit}: the dominant effect of viscosity is then energy dissipation and perturbations are damped;
- certain perturbations are unstable at intermediate Reynolds numbers: viscosity has a destabilizing effect which can be seen as the result of momentum diffusion;
- the flow can be stable above a certain Reynolds number; it tends to be governed by the Rayleigh equation and is stable if the velocity profile has no inflection.

The boundary of the region where instabilities are amplified is known as the *neutral curve* and corresponds to $c_i = 0$ in temporal stability theory. The neutral curves for different frequencies, ω_i, are plotted in a $\alpha\delta^*$ versus Reynolds number Re_{δ^*} plane as shown in Figure 2-2, and are also referred to as *thumb curves* due to their shape. The spatial stability theory leads to similarly-shapped curves in the $\omega\nu/U_e^2 - Re_{\delta^*}$ plane for different values of α_i.

Outside of the region delimited by a neutral curve, the flow is stable and disturbances are damped. At large Reynolds numbers, laminar velocity profiles with

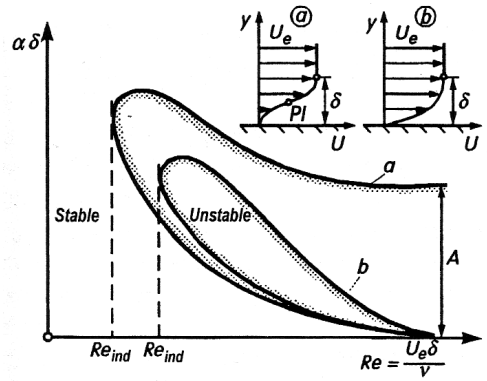

Figure 2-2: Illustration of neutral stability curves: neutral stability defines a range of Reynolds numbers and wave lengths over which instability may occur. Profile (a) has a point of inflection and hence is subject to inviscid instability at large Reynolds number. Profile (b) has no point of inflection and hence is stable in the limit of large Reynolds number. [Figure from Schlichting and Gersten (2000)]

no point of inflection (inviscidly stable) correspond to a closed neutral curve as illustrated in Figure 2-2. The critical Reynolds number corresponds to the left-most point of the neutral curve, and below it no disturbances are amplified. The growth rates of unstable disturbances are given by the points enclosed by the neutral curve, with maximum growth corresponding to the inner-most point inside the curve.

It is important to note that the Orr-Sommerfeld equation is particularly sensitive to the numerical procedure employed, which explains why it could only be solved computationally in the 1960s. As explained by Schlichting and Gersten (2000), this is due to the fact that the solution $\phi(n)$ varies strongly with n both near the wall (viscous part) and near the critical layer where $U - c = 0$ (due to the inviscid contribution and the singular point of the Rayleigh equation). Another way to see this is by looking directly at the Orr-Sommerfeld equation (2.3): the coefficient of highest order derivative ϕ'''' is the small factor $1/Re$ and hence ϕ'''' variations are hard to resolve. Similar complications arise when trying to solve the equation analytically.

For boundary layers, stability computations are complicated even further by the fact that one of the boundaries lies at infinity. Indeed, the basic boundary layer flow $U(n)$ is not an exact solution of the Navier-Stokes equations since variations in the free-stream x-direction are not exactly null.

2.2.2 Secondary Stability Theory

Primary stability theory deals with the initial, linear growth of instabilities in a laminar basic flow. Secondary stability theory aims at predicting the onset of three-dimensional perturbations, starting from the perturbed, two-dimensional, flow obtained from primary stability. In other words, the solution of the primary stability calculations is taken as the basic flow over which three-dimensional perturbations are superimposed, the growth of which is studied through a procedure similar to that followed in primary stability analysis. Details can be found in the works by Schlichting and Gersten (2000); Drazin and Reed (1981); Cebeci (2004); Herbert (1988).

Secondary stability theory is important for determining where the flow transitions. However, transition prediction can usually be solely based on primary stability considerations: the actual transition location can be correlated to the initial linear disturbance growth since the non-linear breakdown is very fast compared to the linear growth. In a laminar separation bubble over an airfoil, the non-linear growth occurs over a very short distance of the order of a couple of percents of the chord (LeBlanc et al., 1989), and is thus not relevant for the problems considered here.

2.3 Transition in Laminar Separation Bubbles

As explained previously, laminar boundary layers tend to separate under adverse pressure gradient conditions much easier than turbulent boundary layer which carry more energy and momentum. As a result, the formation of a laminar separation bubble (LSB)—illustrated in Figure 2-3—is a phenomena often encountered in low Reynolds number flows. Studies of the transition to turbulence in conjunction with an LSB (Alam and Sandham, 2000; Lang et al., 2004) provide the scenario summarized by Hain et al. (2009) as follows:

- in the attached flow, the magnitude of Tollmien-Schlichting (TS) waves is amplified, as in classical scenarios of natural transition;
- as the laminar flow encounters an adverse pressure gradient, the flow separates;
- in the separated shear layer, TS waves are further amplified, leading to Kelvin-Helmholtz (KH) instability, the development of three-dimensional vortices, and eventually to the breakdown to turbulence in the free shear layer;
- the now turbulent flow reattaches to the wall, thus closing the separation bubble.

A laminar separation bubble can thus form on the suction side of airfoils at low Reynolds numbers and large angles of attack, when the stable vortex street observed at somewhat lower angles or lower Reynolds numbers becomes unstable and causes the separated boundary layer to reattach. This occurs for the SD7003 infinite wings studied here, for which at a Reynolds number of 60,000 an LSB is present on the upper surface of the foil, but is not observed at a lower Reynolds number of 10,000 when the separated shear layer does not reattach.

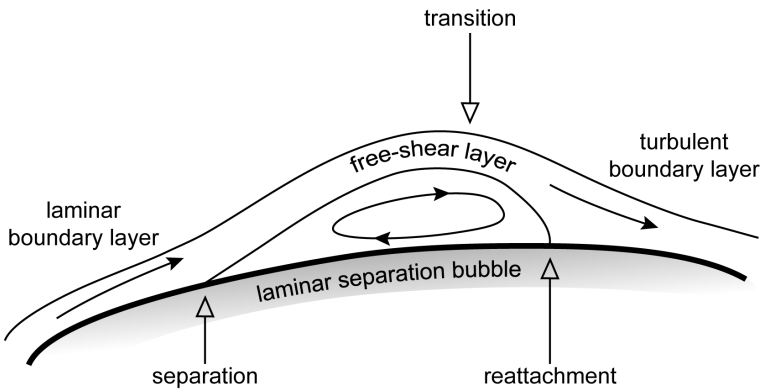

Figure 2-3: Illustration of the flow structure in a laminar separation bubble.

The transition location along a separation bubble determines the bubble's size: rapid transition induces rapid reattachment, while delayed transition results in a longer separation bubble. In turn, aerodynamic performance is strongly influenced by the length of the separation region. Hence, the accurate prediction of transition location is crucial in low Reynolds number flows, especially when an LSB is present.

2.4 Cross-Flow and Transition

The nature of cross-flow over swept wings is explained by Reed and Saric (1989, 1996); Reshotko (1994). Near the leading edge, the combination of pressure gradient and sweep deflects the inviscid streamlines inward (*i.e.* away from the tip of a backwards-sweep wing), and then outwards near the trailing edge, as show in the left-hand side of Figure 2-4. The boundary layer flow carries less momentum and hence this deflection is larger near the wall, which results in a secondary flow perpendicular to the inviscid streamline direction, known as cross-flow. Hence, the cross-flow velocity is zero both at the boundary layer edge and at the wall as illustrated in Figure 2-4, such that the cross-flow profile has an inflection point and is inviscidly unstable. Disturbances in the form of cross-flow vortices propagate, which rotate all in the same direction close to the inviscid streamline direction and have a span-wise periodicity of the same order as the boundary layer thickness (about twice or three times the thickness). Relative to these, counter-rotating Görtler-vortex instabilities are negligible when the sweep angle is large compared to $Re^{-1/2}$, that is for even moderately-swept wings.

The mathematical basis of cross-flow instability was developed in the 1950s by Gregory et al. (1955) through an Orr-Sommerfeld type solution, and also by Owen and Randall (1952) who derived a transition criteria for cross-flow instabilities as

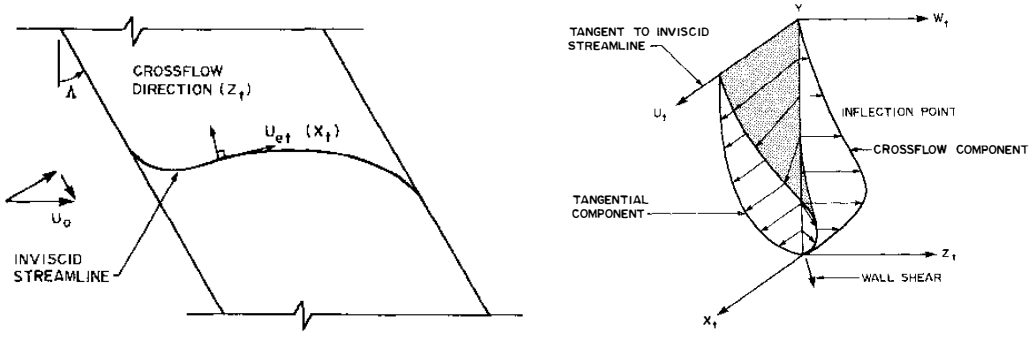

Figure 2-4: Schematic of swept wing's (left) inviscid streamline, and (right) velocity components in the boundary layer. [Figures from Reed and Saric (1989)]

the location where the cross-flow Reynolds number $Re_{CF} = W_{\max}\delta_{10}/\nu$ reaches 150, where δ_{10} denotes the distance from the wall to the point where the cross-flow velocity reaches 10% of its maximum value $W_{\max}$ (point above the maximum).

The parameters which are important in cross-flow stability studies are the height of the inflection point (related to inviscid stability), the velocity gradient at this point (larger shear stress at inflection resulting in more unstable profiles), and the maximum cross-flow velocity (linked to the streamline curvature responsible for the cross-flow).

A finding which is of particular importance to transition prediction is provided by Strokowsky and Orszag (1977): when the cross-flow is unstable, the boundary layer stability characteristics are very close to those of the cross-flow alone (*i.e.* irrespective of the streamwise flow); when the cross-flow is stable, the stability characteristics are essentially those of the streamwise profile. Hence, the stability of the cross-flow and streamwise profiles can usually be considered separately, except in regions where interactions are important as for instance in the leading edge region (Reshotko, 1994).

As Reed and Saric (1996) point out, cross-flow instability is usually dominant near the leading edge where pressure gradients are important, and the shift between cross-flow and streamwise (Tolmien-Schlichting) instability occurs when the cross-flow profiles become S-shaped and hence highly stable. The authors point out that in this region where the prevalent mechanism switches, e^N envelope methods need to be used carefully (*e.g.* decay can be confused with large growth factors), and that critical factors for transition due to cross-flow instability can be very large. Furthermore, non-linear saturation of disturbance amplitude can be observed before transition occurs and hence methods based on linear stability do not work well to predict cross-flow dominated transition (Arnal, 1994; Reed and Saric, 1996; Saric et al., 2003).

Another important consideration related to transition prediction is that, due to the large streamwise velocity gradients close to the wall and the related substantial momentum exchanges, small fluctuations in the cross-flow or in the normal velocity can lead to large steamwise disturbances which soon become too large for non-linear interactions to be neglected (Saric et al., 2003). This can occur even close to the attachment line which divides the flow between the branch that follows the upper surface and the one that follows the lower surface. Thus, a flow can transition due to the growth of streamwise instabilities over swept wings and yet be destabilized by cross-flow fluctuations. Therefore, we deem important to device a transition method that takes into account the fact that the cross-flow disturbs the streamwise profile even when the TS waves are the most significantly amplified disturbances.

2.5 Transition Prediction

While the modeling of turbulence has been the subject of a significant number of studies for many years, the prediction and modeling of transition has only received substantial attention in the last couple of decades. No single approach to transition simulation has found widespread use and applicability for general CFD applications.

The different approaches reported in the literature on transition prediction fall into three main categories: use of correlations, use of semi-empirical methods based on linear stability, and use of low-Reynolds number turbulence models. In addition, some authors make use of an intermittency factor function to blend fully-laminar and fully-turbulent methods. A summary of the characteristics of each approach is given here with a selection of previously published literature.

2.5.1 Empirical Correlations

The first approach ever used to account for transition in aerodynamic flows is the use of empirical correlation methods, which usually provide a way of determining the boundary layer momentum thickness Reynolds number, Re_θ, at transition. The popular Abu-Ghannam and Shaw (1980) correlations predict the start and the end of the transition process, as well as the boundary layer development along the transition region, given as input the free-stream turbulence level and velocity distribution.

While correlations are computationally inexpensive and can be very useful *e.g.* for coupling potential-flow codes to boundary-layer computations, they lack in generality and can only be expected to provide accurate predictions for the types of flows for which they were derived. Furthermore, as Menter et al. (2006) point out, they cannot be easily incorporated into standard CFD techniques due to such difficulties as defining the boundary layer edge, integrating boundary layer parameters on unstructured grids and parallel computations, and the use of non-local information.

2.5.2 Linear Stability and the e^N Method

Though the actual transition to turbulence depends on considerations not taken into account by primary (linear) stability theory, the transition location can be related to the amplification of linear disturbances by assuming that breakdown to turbulence is inevitable past a given amplification. This is the basis for the very successful and affordable transition prediction e^N method introduced independently and almost simultaneously by Ingen (1956) and by Smith and Gamberoni (1956). By solving the

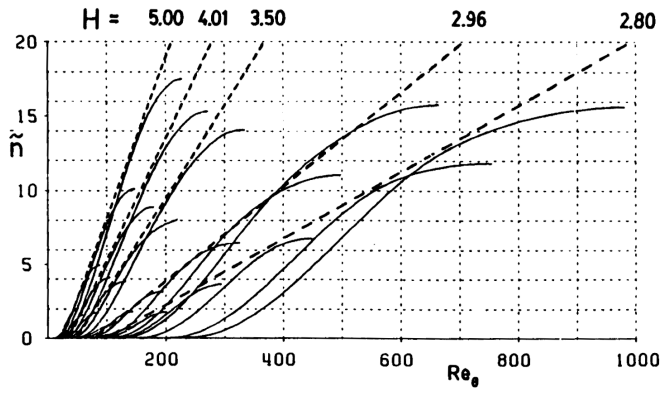

Figure 2-5: Envelope method for e^N: curves of spatial amplification calculated from the Orr-Sommerfeld equation, and their envelopes (dotted lines) for different shape factors; $\tilde{n}$ on the vertical axis is the amplification factor which we call here N. [Figure from Drela and Giles (1987)]

Orr-Sommerfeld equation, the ratio of the amplitude of a disturbances to its initial amplitude is calculated for a range of frequencies, and transition is taken to occur when the amplitude of the single most amplified disturbance reaches a certain critical amplification factor N_{crit}, called the critical N-factor

The e^N method is categorized as a semi-empirical method due to the determination of the critical N-factor via empirical correlations or experimental observation, with measured values between 7.8 and 10. The value of $N_{crit} = 9$ being the most commonly used, the method was known as the e^9 method for many years.

As originally proposed, this method requires the computation of the amplification factor evolution for all the possible disturbance frequencies. In order to decrease the computational cost, envelope methods were developed by Gleyzes et al. (1985) and by Drela and Giles (1987) which approximate with straight lines the envelopes of integrated amplification rates for a given frequency. Thus, a family of amplification curves is reduced to a line which is the locus of $\max(N)$ versus Re_θ for a given boundary layer shape parameter (dotted lines in Figure 2-5). In this manner, the computational cost is reduced from that of computing all the amplification curves, to that of computing a single line slope for the envelope.

Envelope methods have been, and are still, widely and successfully used for engineering applications, for instance in the code XFOIL (Drela, 2002). Their success might be linked to the fact that the uncertainty in the value of N_{crit} is of the same order of magnitude as the approximation made when using an envelope method relative to the solution of the Orr-Sommerfeld equation.

It is important to keep in mind that the e^N method, being based on linear stability

theory, is particularly appropriate for predicting transition in flows where the linear growth of TS waves is the dominant transition mechanism, which "happens to be the case in a vast majority of airfoil applications" (Drela, 2002). It cannot predict transition due to non-linear effects such as high free-stream turbulence or surface roughness. To partly address this limitation, Mack (1977a,b) proposed the correlation

$$N_{crit} = -8.43 - 2.4 \ln(Tu)$$

between the critical amplification and the free-stream turbulence intensity Tu; it has proved very successful even though it reduces the free-stream disturbance to its turbulence intensity only, thus not taking into account the boundary layer receptivity.

Separated Flows in Boundary-Layer Codes. Some authors have extended the e^N method to account for separation-induced transition. To simulate flows over airfoils with an LSB, Dini et al. (1992) employ a database of stability characteristics of velocity profiles, with Falkner-Skan self-similar profiles for the attached flow regions and a more general family of profiles for separated flow regions. Shum and Marsden (1994) developed a two-dimensional model for the analysis of boundary layers in LSBs based on the simple bubble model of Horton (1967); the bubble calculation uses the model downstream of separation and transition is determined by an e^N method.

Coupling with Navier-Stokes Codes. Coupling the e^N method for transition prediction to Navier-Stokes codes has some inherent difficulties. First, it requires tracking the amplification factor of disturbances along streamlines which are hard to identify in three-dimensional flows. Furthermore, Navier-Stokes solvers are not usually accurate enough to evaluate stability equations through laminar boundary layer parameters (Stock and Haase, 1999; Radespiel et al., 1991, 2007), since the boundary layer needs to be resolved with high accuracy—for the velocity profile and its curvature—in order for stability computations to be reliable.

In spite of these issues, some researchers have coupled the e^N method with Navier-Stokes codes by addressing the different problems in one way or another. Most of the approaches that have been reported involve the coupling of Navier-Stokes computations with a stability module that either solves the stability equations, relies on a stability database, uses an envelope method, or calls a boundary layer code as an intermediate step. An early attempt was made by Cebeci (1989) who designed a viscous-inviscid method for low-Reynolds number flows around airfoils. More recently,

substantial efforts have been made by German Aerospace researchers at DLR to couple the e^N method with low-order finite-volume RANS solvers (Stock and Haase, 1999; Stock, 2002; Radespiel et al., 1991; Nebel et al., 2003; Krimmelbein et al., 2005; Radespiel et al., 2007; Yuan et al., 2005, 2007; Krumbein, 2006); most employ the assumption of constant pressure in the direction normal to the wall and Bernoulli's formula to determine the boundary layer edge location.

Treatment of Cross-Flow Instabilities. The e^N method being so successful at predicting TS-type transition, several authors have extended it for the prediction of transition due to cross-flow (CF) instabilities over three-dimensional geometries.

Krumbein (2006) of DLR coupled a RANS solver with a laminar boundary layer code, and two e^N databases in order to predict transition due to TS (represented by N_{TS}), CF (represented by N_{CF}), and mixed (interacting TS and CF) instabilities over wings. The difficulty in predicting mixed transition is addressed via different stability boundaries in the N_{TS}-N_{CF} plane. If laminar separation is detected, transition is simply fixed at the separation point; this was shown to work well for relatively high Reynolds number flows (2 to 11 millions) in which separation occurs over a small spatial length—but this is not usually the case for low-Reynolds number flows.

Similarly, Krimmelbein and Radespiel (2009) employed an empirical approach in which the values of N_{crit} are reduced in the N_{TS}-N_{CF} plane by assuming a linear decay of N_{TS} with increasing N_{CF}, if either of the two N-factors is above unity, in order to represent a mixed-type transition (see also Nebel et al., 2003; Krimmelbein et al., 2005).

2.5.3 Standard and Low-Reynolds Number Turbulence Models

Attempts at predicting transition using solely standard RANS turbulence models have been unsatisfactory, in particular when separation is present (see for instance Ekaterinaris and Menter, 1994). In view of this, several authors have proposed modifications or additions to standard models in order to treat low Reynolds number flows. For instance Wilcox (1994) proposed changes to his k-ω model, including viscous modifications such that $k \sim n^2$ as a wall is approached, the addition of two transition-specific coefficients and of a way to trigger transition at a desired location. Nürnberger and Greza (2002) proposed an extension of the SA model (Spalart and Allmaras, 1994) for low-Reynolds number flows in periodic domains, which includes

the use of the transition correlation of Drela (1995).

A major shortcoming of low Reynolds number RANS models is that they can only distinguish the magnitude and an average frequency of perturbations, and hence cannot discern the range of frequencies that destabilizes the boundary layer, nor determine which perturbations actually cause transition. Their purpose is to predict transitional flows using calibration coefficients as much as needed, rather than to try to predict the onset and mechanism of transition. Furthermore, it has often been found that low Reynolds number models cannot predict transition for a wide variety of flows (Savill, 1993; Menter et al., 2006). Another disadvantage is the sensitivity of model variables to far-field values and initial profiles (Abid, 1993; Zheng et al., 1998).

With respect to the limitations associated with separated flow simulations, Probst and Radespiel (2008) point out that the Boussinesq approximation (eddy-viscosity concept) cannot account for effects observed in flows with separation, such as Reynolds stress anisotropy, local non-equilibrium, and streamline curvature. Their solution is to use a Reynolds stress model (RSM) with an intermittency factor as a blending function between laminar and turbulent RANS coefficients.

2.5.4 Use of the Intermittency Factor

In order to represent the transition length, many authors have combined laminar and turbulent regions of the flow using the intermittency factor γ, which is defined as the fraction of the time any point spends in turbulent flow and can be computed via a function specification (*e.g.* that by Dhawan and Narasimha, 1958) or via a transport equation. It quantifies the existence of turbulent spots ($\gamma = 0$ in laminar flow, $\gamma = 1$ in fully turbulent flow), but requires the specification of the onset of transition by another method such as an e^N-type approach. It has been used to modify RANS models by replacing the eddy viscosity μ_t with $\gamma\mu_t$, while other quantities are taken as linear combinations of laminar and turbulent parts, *e.g.* $\overline{f} = (1-\gamma)\,\overline{f}_\ell + \gamma\,\overline{f}_t$.

Of particular interest to us is the work by Lian and Shyy (2007) who employ a RANS k-ω solver coupled with an envelope e^N method based on Drela and Giles (1987), with their own intermittency function tailored for simulating low Reynolds number flows with separation. They study the two-dimensional flow around an SD7003 profile with good comparison with experimental measurements. As mentioned previously, they assume constant pressure in the direction normal to the wall and use Bernoulli's formula to determine the location of the boundary layer edge.

There is an intrinsic limitation in an approach that treats the overall flow as

a linear combination of laminar and turbulent parts, namely the lack of interaction between turbulent spots and laminar flow pointed out by Steelant and Dick (1996). In particular, laminar flows are found to separate as soon as an adverse pressure gradient is encountered. Of all the reported methods that make use of the intermittency factor, only Menter et al. (2006) have tested the resulting transition prediction capability in conjunction with laminar separation bubbles and they obtain good results when incorporating a modification designed for separation-induced transition. Another advantage of their approach is that it is local and meant to be easily coupled with general CFD methods.

Another efficient coupling with CFD codes is the transition approach proposed by Warren and Hassan (1998) who treat non-turbulent fluctuations in a manner similar to the turbulent fluctuations by introducing an effective eddy viscosity

$$\mu = \mu_\ell + [(1-\gamma)\,\mu_{\ell t} + \gamma \mu_t]$$

which involves the laminar (molecular) viscosity μ_ℓ, the eddy-viscosity μ_t, as well as a viscosity that represents non-turbulent fluctuations and is linked to the turbulence model variables by $\mu_{\ell t} = C_\mu\,\rho\,k\,\tau$. Their method is not designed to predict mixed transition, and the application to high Reynolds number flows where either TS or CF instabilities dominate seem to produce accurate results. However, it requires *a priori* knowledge of the dominant transition mechanism, which is not possible for all flows.

2.5.5 Other Approaches

Inspired by the works of Mayle and Schulz (1997), Walters and Leylek (2004) proposed a different kind of RANS model to account for transitional flows. It is a three-equation model which adds to a traditional k-ϵ model an equation for a laminar kinetic energy variable, which is meant to represent the growth of non-turbulent, streamwise fluctuations present in the pre-transitional regime and functions as a source term for the turbulent kinetic energy. The model was successfully tested for turbulent channel flow and bypass transition applications. However, this model does not seem to be applicable to separation-induced transition.

In his three-dimensional study of the low Reynolds number flow around an SD7003 airfoil, Tang (2006) avoided predicting transition altogether and simply set the transition location to "the point where the tangential velocity adjacent to the surface reverses direction for the second time after the laminar separation." It is doubtful that this procedure would prove accurate for a wider variety of flows.

2.6 Large Eddy Simulation

On the one end of the spectrum of numerical simulation techniques for turbulent flows is the approach based on the Reynolds-Averaged Navier-Stokes (RANS) equations which employs turbulence closure models to represent all the motion scales. For unsteady flows, Unsteady RANS (URANS) simulations have been used, but it is not clear what this approach actually solves for since phase-averaging is not well defined (Lesieur et al., 2005). Fluctuations are smoothed out by Reynolds averaging and hence RANS/URANS methods do not normally allow for the accurate prediction of instantaneous and statistical quantities.

On the other end of the spectrum is the Direct Numerical Simulation (DNS) method which resolves all the flow scales down to the smallest dynamically significant scale (the Kolmogorov scale) and involves no modeling approximation. Its computational cost remains prohibitive for most flows of engineering and design interest, in particular for complex geometries, flows at moderate to high Reynolds numbers, and even simple but unsteady low Reynolds number cases.

An intermediate approach, still accurate and yet more affordable, is to perform Large Eddy Simulations (LES). While it is estimated that LES type simulations will not be feasible for industrial applications (*e.g.* flow over an aircraft) before the second half of the century, they can be extremely useful for simpler flows.

In an LES, the large-scale motions are resolved while the small scales are modeled. The principle justifying this approach is the fact that the larger scales, because of their size and strength, carry most of the flow energy while being responsible for most of the transport, and therefore should be simulated precisely (*i.e.* resolved). On the other hand, the small scales have relatively little influence on the mean flow and thus can be approximated (*i.e.* modeled). Furthermore, small scales tend to be more homogeneous and isotropic and hence are easier to model for a wide variety of flows than the large scales.

Because of the non-linear nature of the Navier-Stokes equations, all turbulent scales are dynamically coupled. Thus, for the resolved scales to be dynamically accurate, the effect of unresolved, subgrid scales needs to be taken into account, either with a subgrid scale (SGS) model as in the standard (explicit) LES approach, or via numerical dissipation as in the Implicit LES (ILES) method.

A peculiarity of the LES approach is that grid refinement is linked to modeling since the size of the smallest resolved eddies corresponds to the grid size. Refining the grid results in "large scale" motions containing smaller eddies, and hence the aim

of grid refinement is to provide richer structures (physical resolution): the solution will show more and more features as the resolution is increased. On the contrary, in a RANS approach, the goal of grid refinement is numerical accuracy (Spalart, 2000).

Another aspect to keep in mind is that the LES method relies on the premise that small scales are close to homogeneous and isotropic and have little influence on the mean flow. In order for this to hold in a strict mathematical sense, the cut-off between resolved and subgrid scales should be located in the inertial subrange where the energy cascade decays as $k^{-5/3}$ (see Appendix A). This is an imperative requirement only when using scale invariance models (Meneveau and Katz, 2000), and LES has successfully been applied with different cut-off levels.

2.6.1 Limitations of Explicit LES

A major assumption intrinsic to explicit LES is that the numerical error related to the numerical technique employed is small compared to the resolution error resulting from the fact that not all significant scales are resolved (see Appendix C for more on the sources of error in LES). However, numerical stabilization is of a dissipative and dispersive nature, and the truncation errors in a typical LES are of the same order of magnitude as the subgrid-scale terms (Sagaut, 2007; Hirt, 1969; Ghosal, 1996).

Through a theoretical analysis of isentropic turbulence, Ghosal (1996) shows that the magnitude of dispersive errors of a high-order (up to eighth) central finite-difference scheme is larger than the subgrid-scale forcing term, and that the numerical error dominates the subgrid-scale contribution at all resolved scales. This has been confirmed by numerical experiments (Sagaut, 2007). It is also possible that partial cancellations occur between numerical and modeling errors for some flows, thus resulting in a more accurate solution when lower-order methods are employed, but counting on random error cancelation cannot be considered a sensible approach.

2.6.2 Implicit LES

An alternative to the use of subgrid-scale models is to take advantage of the numerical dissipation of the solution scheme to account for the dissipation that would take place in the unresolved scales. As Grinstein et al. (2007b) point out, the ILES development and success has emphasized the importance of using numerical methods that inherit the relevant properties of real physical flows rather than simply considering them as approximations. The aim is to provide the viscous effect of the unresolved scales on the large-scale motions without explicitly resolving these small scales, thus "captur-

ing physics with numerics" in a manner similar to what is done in shock capturing techniques (Grinstein et al., 2007a).

The first ILES approach was introduced by J. Boris and his collaborators at the Naval Research Laboratory (NRL) who termed it Monotone Integrated LES (MILES) as a reference to the use of monotone (positive-preserving) convection algorithms (Boris, 1990). Boris (2007) explains that the "MILES approach evolved more as a growing realization than an invention". He gives arguments for why the MILES approach (and other ILES) should work, and details some important physical considerations: the cut-off level should be in the inertial range of the energy cascade (see Appendix A) in order to warranty that the energy contained in the unresolved scales is small enough and that all energy-producing eddies are resolved (more details in Appendix C). Furthermore, one cannot expect to accurately resolve features that are, by the grid coarseness, necessarily under-resolved, but one can reasonably demand that resolved features be simulated accurately: the algorithm is to "do minimal damage to the larger wavelengths while still incorporating, at least qualitatively, most of the local and global effects of the unresolved turbulence" (Boris, 1990).

While the above are qualitative considerations, several authors have made use of modified equation analysis (MEA) to identify and quantify the errors of a numerical algorithm: it is possible to show that a numerical method solves a certain differential equation more accurately than the original equation, and that "leading-order truncation error terms introduced provide implicit SGS models similar in form to those of conventional mixed SGS models" (Drikakis et al., 2007). Again, more details are provided in Appendix C.

The absence of an explicit subgrid-scale model equation also makes the ILES approach easy to implement (Grinstein et al., 2007c). Furthermore, the lack of an extra equation to solve reduces the computational cost, and hence one could use a somewhat slightly finer mesh instead. As Boris (1990) puts it, "a factor of two increase in the spatial resolution of [an implicit] LES model will bring more improvement in the accuracy of the well-resolved scales than all the work in the world on the subgrid model of a more coarsely resolved LES."

Finally, it is important to note that different numerical algorithms (and implementations) provide different implicit subgrid-scale models and result in different effects on the resolved scales, similarly to the use of different explicit SGS models; hence different algorithms will likely be suited for different types of flow. As stated by Grinstein et al. (2007b), "in principle, the lack of parameters in the ILES approach implies the increased generality and predictive capabilities of the ILES approach. In

practice, we believe it is important to quantify the limits of applicability of this approach by continuing with testing and making efforts to understand its foundations."

2.7 Transition and Turbulence Prediction with a DG Method

High-order methods are particularly suited for transition and turbulence simulations. They provide low diffusion error, which allows for the use of fewer grid points and degrees-of-freedom than low-order methods to resolve a given length scale. In addition, they have the advantage of having a low dispersion error, which refers to the error in the representation of waves (phase errors for instance) introduced by time marching. This is important for accurate long time integrations for which dispersion would for instance affect the turbulent spectrum.

The introduction of high-order methods for fluid flow computations is relatively recent, and for most of the past 40 years the numerical simulation of turbulent flows has been dominated by second-order-accurate finite-volume methods for which accuracy is closely linked to the number of grid points and hence to the computational cost. The alternative of high-order finite-volume methods requires complex reconstructions. The finite-difference method does not have this disadvantage, but its dependence on structured grids makes it ill-suited to handle complex geometries.

The Discontinuous Galerkin (DG) method provides many of the advantages of finite-element methods while retaining the main strengths of finite-volume methods for conservation laws. In particular, it relies upon a strong mathematical foundation, allows for high-order implementations, and is able to handle complex geometries and grid adaptation with unstructured grids. Furthermore, it provides local conservation and a stable discretization of the convective operator.

On the other hand, the DG method requires significantly more operations per degree-of-freedom than finite differences and low order finite volumes. This is only partly offset by the use of high-order representations of the solutions, with typically third to fifth order polynomials used in practice. Much needs to be done to make the DG method a serious contender to established CFD techniques, both in terms of numerical schemes and of implementation, but the advantages of DG and the potential for resolving some of the main limitations of other methods for fluid flow computations seem to justify the effort.

The DG method was first introduced by Reed and Hill (1973) for the solution of

a linear transport equation. Some of the milestones that have contributed towards the successful use of DG for fluid flow problems include the following. Chavent and Cockburn (1989) first introduced the finite-volume technique of slope-limiting to treat hyperbolic systems with DG, and Cockburn and Shu (1991, 2001) presented a DG method using Runge-Kutta time stepping (RKDG). A generalization of the RKDG approach for convection-diffusion systems is due to Bassi and Rebay (1997), with a further improvement embedded in the Local DG (LDG) method by Cockburn and Shu (1998) in which stability is achieved at the expense of compactness. This loss motivated Peraire and Persson (2008) to derive a more efficient Compact DG (CDG) technique. Bassi and Rebay (2000) also improved their method for better stability and to preserve a compact stencil. The last couple of years have seen an effort at reducing the number of degrees-of-freedom of the DG method and taking advantage of super-convergence properties, with the emergence of Hybridized DG (HDG) and Embedded DG (EDG) methods (Cockburn et al., 2008, 2009; Nguyen et al., 2009).

2.7.1 RANS with DG

The DG method having only been applied to fluid flow problems in the last couple of decades, there are few published results on turbulent flows. Another reason lies in the robustness challenges that a DG implementation for RANS poses: high-order procedures are even more sensitive than low-order simulations to under-resolution and numerical artifacts because of the very low intrinsic dissipation.

Bassi et al. (2005) applied a DG method with polynomials of order at most two (for up to third-order spatial discretizations) and a k-ω turbulence model to study two-dimensional, high Reynolds number applications. They obtained good results with relatively coarse computational grids proving the effectiveness of the method, but found it to be "a challenging task because of the extreme stiffness of the problem. In practice it is mandatory to supplement the RANS and turbulence model equations with some form of limiting of the magnitude of the computed turbulent quantities in order to prevent the blow-up of the simulation." This can happen for instance when the eddy viscosity becomes negative, thus resulting in energy production rather than the intended dissipation. Among the modifications to the original turbulence model that had to be made are the use of $\ln(\omega)$ as the model variable instead of ω, setting the turbulent kinetic energy to $\max(0, k)$ in the source terms, and imposing realizability conditions to ensure that normal turbulent stresses remain positive.

Landmann et al. (2006, 2008) used the form of the $k-\ln(\omega)$ method of Bassi et al. (2005), as well as the SA model by Spalart and Allmaras (1994) with a hard limiting on the model variable. They provide results for the two-dimensional simulations of both laminar (circular cylinder and airfoil) and turbulent (flat plate with prescribed transition and airfoil) cases. With the use of polynomials of order one through three, they obtain good agreement with previously published results.

Following an approach that was used for shock capturing by Persson and Peraire (2006), Nguyen et al. (2007) performed two-dimensional DG RANS simulations with the SA model by introducing an artificial viscosity approach. They identified the fast change in curvature of the eddy viscosity profile that occurs at the boundary layer edge as one of the reasons artificial viscosity is required, since the thickness of this region scales like the laminar viscosity and hence cannot be adequately resolved. As the authors point out, the result of the artificial diffusion is to modify the profiles of eddy viscosity at a location where it tends to zero and hence the effect on the overall solution is minor. The turbulent suppression and trip terms of the SA model are not implemented, and hence the simulations are fully turbulent with results given for a flat plate, circular cylinder, and airfoil flows in subsonic and transonic regimes.

An alternative approach to using the SA model with DG is proposed by Oliver and Darmofal (2009) and consists of modifying the model equation. Some terms are revised in order to prevent them from becoming negative with positive eddy viscosity values, and additional changes are introduced when the eddy viscosity becomes negative. Again, no trip term is implemented and fully turbulent, two-dimensional results are provided for the flow around airfoils. The authors point to the turbulence model regularity as a determining factor for optimal accuracy and note that additional smoothness of turbulence models would significantly improve the robustness and accuracy of high-order RANS simulations.

Kessler (2007) observes that, since the solution is represented by high-order polynomials in each grid cell, it has some structure within the cell, and hence the implementation of physically and numerically sound limiting procedures such as the ones commonly employed in finite-volume methods is not straight-forward. He suggests that a turbulence model may need to be developed specifically for DG methods and take advantage, for instance, of the availability of high-order derivatives.

2.7.2 LES with DG

The DG method has only been used for (LES) by a couple of groups. Collis (2002), Ramakrishnan and Collis (2004) use a Variational Multi-Scale (VMS) LES method with DG spatial discretization to simulate three-dimensional, fully-developed, channel flows with no subgrid-scale model (*i.e.* ILES or coarse DNS). They then consider LES with a constant-coefficient Smagorinsky subgrid-scale model, and with a constant coefficient Smagorisky variant of the VMS model for a channel. The authors acknowledge the fact that computing turbulence statistics from a DG method is non-trivial, but show that the prediction of low-order statistics (mean and root mean square quantities) can be accomplished using fewer degrees-of-freedom with DG than with traditional low-order methods. They also note that the numerical dissipation in low-order upwind finite-differences and finite-volume methods tend to suppress turbulent fluctuations, and point out as future research the need to study the role of subgrid-scale modeling in DG discretizations.

Sengupta and Mashayek (2007) used a DG spectral method for two-dimensional LES of channel flow using the dynamic subgrid-scale model of Germano et al. (1991). They also performed DNS runs and compared the results to previous studies. Xu et al. (2007) employed a DG spectral method for DNS and LES with the Smagorinsky model for the two-dimensional simulations of a mixing layer and a back-facing step.

In the author's knowledge, at the time when the first results of the present work were presented (Uranga et al., 2009), no attempts had been reported of the use of DG with an Implicit LES approach for non-periodic, fully three-dimensional flows. The only three-dimensional simulation published was for a periodic, fully developed, channel flow by Collis and collaborators.

2.8 Flow Around SD7003 Airfoils and Wings

We now turn to review some of the published research involving the SD7003 airfoil used in the present work and summarized in Table 2.1. This profile, shown in Figure 2-6, has a maximum thickness of 8.51% and camber of 1.46%, and Selig et al. (1989, 1995) provide detailed experimental measurements of velocity profiles, drag, lift, and moment coefficients at Reynolds numbers ranging from 60,000 to 300,000.

Low Reynolds number studies of laminar-separation bubbles (LSB) on airfoils and wings have extensively made use of the SD7003 profile since it exhibits an LSB on the upper surface that is present over a range of Reynolds numbers and angles of attack.

It was designed by Selig's group (Selig et al., 1989, 1995) for use in model gliders with low Reynolds number flows that are prone to laminar separation. In order to minimize the effects of separation, moderately adverse pressure gradients upstream of the separation point amplify the Tollmien-Schlichting (TS) disturbances so that transition takes place rapidly after separation and the flow reattaches.

The flow around a rectangular SD7003 wing at Reynolds number 60,000 and 4° angle of attack has been studied experimentally using particle-image velocimetry (PIV) by several groups, thus providing a good database for validation. Ol et al. (2005) give a comparison between results obtained at three different facilities: the tow tank at the Institute for Aerospace Research (IAR) of the National Research Council of Canada, the Technical University of Braunschweig (TU-BS) low-noise wind tunnel, and the Air Force Research Laboratory (AFRL) free-surface water tunnel. The comparison focuses on contours of mean velocity and Reynolds stresses, as well as on separation, transition, and reattachment locations. The results from IAR and TU-BS compare well, but the separation bubble of the AFRL experiments is located significantly closer to the leading edge: the difference in separation location between AFRL and IAR is of 45%, while the difference between IAR and TU-BS is less than 10%. The authors suggested that this may be due to the true angle of attack of the wing in the AFRL experiments being slightly larger than the prescribed 4°. Results for angles of attack of 8° and 11° obtained at the AFRL water tunnel are also provided.

Three-dimensional Implicit Large Eddy Simulations (ILES) were carried out by M. Visbal and collaborators (Galbraith and Visbal, 2008; Visbal et al., 2009) using a high-order compact-differences code and well-resolved grids. They studied the flow at a Reynolds number of 60,000 and six different angles of attack between 2° and 14°, and also at varying Reynolds numbers between 10,000 and 90,000 for an 8° angle of attack. They observed that the LSB decreases in size and moves closer to the leading edge with either increasing angle of attack or increasing Reynolds number, while no transition takes place for Reynolds numbers of and below 40,000. In the cases when

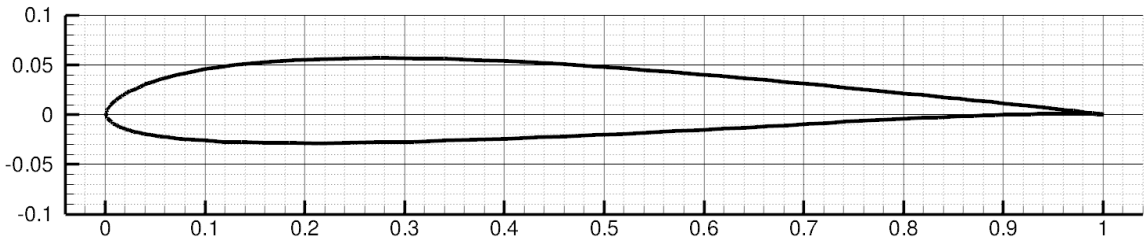

Figure 2-6: SD7003 airfoil.

Table 2.1: Previous studies of low Reynolds number flow around an SD7003 airfoil.

Reynolds Number	Angle of Attack	References
10,000; 30,000	8°	Galbraith and Visbal (2008); Visbal et al. (2009)
60,000	4°	Ol et al. (2005); Tang (2006); Yuan et al. (2007); Lian and Shyy (2007); Galbraith and Visbal (2008); Visbal et al. (2009); Qin et al. (2009)
	8°, 11°	Ol et al. (2005); Windte and Radespiel (2008); Galbraith and Visbal (2008); Visbal et al. (2009)
	2°, 6°, 14°	Galbraith and Visbal (2008); Visbal et al. (2009)
66,000	2°, 4°, 8°	Hain et al. (2009)
90,000	8°	Galbraith and Visbal (2008); Visbal et al. (2009)

transition did occur, they noted that span-wise coherent structures were present in the separated shear layer which break down due to span-wise instabilities. As expected, the size of the turbulent flow structures decreases as the Reynolds number increases.

An in-depth stability study for the $Re = 60,000$ case at 4° angle of attack is described in another paper by Visbal's group (Qin et al., 2009). Using as base flow the time-averaged flow of unsteady ILES, the assumption of parallel flow (over the small streamwise distance that encloses the LSB) and a smooth spline fitting of the velocity profiles, it is shown that the flow is indeed unstable in the presence of small disturbances. These disturbances are found to be confined to the LSB, and have maximum magnitude and maximum gradient at the center of the bubble, which is consistent with the Reynolds stress contours presented by Visbal et al. (2009).

This flow at $Re = 60,000$ and angle of attack of 4° was also studied computationally by Tang (2006) and by Lian and Shyy (2007), with good agreement with experimental studies. Tang (2006) employed three different turbulence models in RANS simulations as well as an LES calculation; as indicated earlier (section 2.5.5), no transition model is used with the RANS computations and transition is set to the location where "the tangential velocity adjacent to the surface reverses direction for the second time after laminar separation." Lian and Shyy (2007) make use of the standard k-ω model in conjunction with an e^N transition module and provides values for lift and drag coefficients unavailable from PIV experiments.

Hain et al. (2009) conducted an extensive experimental investigation using time-resolved particle-image-velocimetry (TR-PIV) measurements on the 66,000 Reynolds number flow around an SD7003 rectangular wing at angles of attack of 2°, 4°, 8°. The

focus is on the dynamics of laminar separation and on the transition mechanism, and they show that transition is dominated by Kelvin-Helmholtz (KH) instabilities that are responsible for vortex growth and breakdown to turbulence in the separated shear layer. For some cases, they observe that the instabilities that grow after separation and the instabilities that grow before separation have almost the same most unstable frequency. They thus conclude that the TS waves trigger transition, which explains why the length of the LSB is sensitive to the magnitude of the TS waves at separation. Note that the authors consider TS and KH waves to be different phenomena, while actually KH instabilities are a subset of TS instabilities; the Orr-Sommerfeld equation predicts both, whether the flow is attached (known as TS modes) or separated (known as KH modes).

Chapter 3

Methodology

The present chapter provides a description of the computational approach used for solving the three-dimensional, unsteady, compressible Navier-Stokes equations with the Discontinuous Galerkin method. Details on the time-stepping procedure and computational grids are given, as well as on how the boundary layer is analyzed and the transition mechanism established. Finally, a brief description of the form of a proposed transition model equation is given.

3.1 Governing Equations

The motion of a compressible Newtonian fluid is governed by the Navier-Stokes equations which express the conservation of mass, momentum, and energy as

$$\frac{\partial \rho}{\partial t} + \frac{\partial}{\partial x_i}\left(\rho u_i\right) = 0 \tag{3.1}$$

$$\frac{\partial}{\partial t}\left(\rho u_i\right) + \frac{\partial}{\partial x_j}\left(\rho u_i u_j\right) = -\frac{\partial p}{\partial x_i} + \frac{\partial \tau_{ij}}{\partial x_j} \quad \text{for} \quad i \in \{1,2,3\} \tag{3.2}$$

$$\frac{\partial}{\partial t}(\rho E) + \frac{\partial}{\partial x_j}\left[u_j\left(\rho E + p\right)\right] = \frac{\partial}{\partial x_j}(u_i \tau_{ji}) + \frac{\partial q_j}{\partial x_j} \tag{3.3}$$

where the viscous stress tensor, τ_{ij}, and the heat flux, q_i, are defined by

$$\tau_{ij} \equiv \mu\left[\left(\frac{\partial u_i}{\partial x_j} + \frac{\partial u_j}{\partial x_i}\right) - \frac{2}{3}\frac{\partial u_k}{\partial x_k}\delta_{ij}\right] \tag{3.4}$$

$$q_j = \frac{\mu}{Pr}\frac{\partial}{\partial x_j}\left(E + \frac{p}{\rho} - \frac{1}{2}u_k u_k\right) . \tag{3.5}$$

In the above equations, ρ denotes the fluid density, u_i is the velocity component in the direction x_i, p the static pressure, E the total energy per unit mass, μ the dynamic viscosity coefficient, and Pr the flow Prandtl number assumed constant. In order to close the system, the ideal gas equation of state is used in its form

$$p = (\gamma - 1)\rho \left(E - \frac{1}{2} u_k u_k \right) . \tag{3.6}$$

The specific heat ratio is set to $\gamma = 1.4$ and the Prandtl number to $Pr = 0.72$. Moreover, the kinematic viscosity, $\nu = \mu/\rho$, is assumed to be constant since only low Mach number flows are considered.

In the present work we follow the Implicit Large Eddy Simulation (ILES) approach, and the unresolved small eddies are accounted for by means of the numerical dissipation. Hence, no subgrid-scale model is employed and the full (unfiltered) compressible Navier-Stokes equations are solved. This approach is described and motivated in detail in Section 2.6.2 and has been successfully used by Visbal and collaborators using a sixth-order compact difference method for the simulation of low Reynolds number flows around an SD7003 airfoil (Galbraith and Visbal, 2008; Visbal et al., 2009; Garmann and Visbal, 2009; Visbal, 2009).

3.2 High-Order Discontinuous Galerkin Method

The modeling equations (3.1)–(3.6) are solved using a high-order Discontinuous Galerkin method implemented in the computational code *3DG*. This framework solves time-dependent systems of conservation laws of the form

$$\begin{cases} \dfrac{\partial \mathbf{u}}{\partial t} + \nabla \cdot \mathbf{F}^{(i)}(\mathbf{u}) - \nabla \cdot \mathbf{F}^{(v)}(\mathbf{u}, \mathbf{q}) = \mathbf{S}(\mathbf{u}, \mathbf{q}) \\ \mathbf{q} - \nabla \mathbf{u} = 0 \end{cases} \tag{3.7}$$

in a domain Ω, with conserved state variables $\mathbf{u}$, inviscid flux function $\mathbf{F}^{(i)}$, viscous flux function $\mathbf{F}^{(v)}$, and source term $\mathbf{S}$. In the case of the three-dimensional, unsteady,

compressible Navier-Stokes equations,

$$\mathbf{u} = \begin{bmatrix} \rho \\ \rho u_1 \\ \rho u_2 \\ \rho u_3 \\ \rho E \end{bmatrix}, \ \mathbf{F}_i^{(i)} = \begin{bmatrix} \rho u_i \\ \rho u_i u_1 + \delta_{i1} p \\ \rho u_i u_2 + \delta_{i2} p \\ \rho u_i u_3 + \delta_{i3} p \\ \rho u_i \left(E + p/\rho \right) \end{bmatrix}, \ \mathbf{F}_i^{(v)} = \begin{bmatrix} 0 \\ \tau_{i1} \\ \tau_{i2} \\ \tau_{i3} \\ u_k \tau_{ik} + \frac{\mu\gamma}{Pr} \frac{\partial e}{\partial x_i} \end{bmatrix}, \ \mathbf{S} = \begin{bmatrix} 0 \\ 0 \\ 0 \\ 0 \\ 0 \end{bmatrix}, \tag{3.8}$$

where $e = E - u_k u_k/2$ is the internal energy per unit mass.

Following the finite element procedure, we consider a triangulation $\mathcal{T}_h$ of the spatial domain Ω and introduce the finite element spaces

$$\begin{aligned} V_h &= \{ v \in [L^2(\Omega)]^m \mid v|_K \in [\mathcal{P}_p(K)]^m, \ \ \forall K \in \mathcal{T}_h \} , \\ \Sigma_h &= \{ r \in [L^2(\Omega)]^{dm} \mid r|_K \in [\mathcal{P}_p(K)]^{dm}, \ \ \forall K \in \mathcal{T}_h \} , \end{aligned}$$

where $\mathcal{P}_p(K)$ is the space of polynomial functions of degree at most $p \geq 0$ on the tetrahedral element K, m is the dimension of $\mathbf{u}$ and number of states, and d is the spatial dimension. In the case of three-dimensional simulations, $d = 3$ and $m = 5$. Curved elements are handled by iso-parametric mapping to a straight master (reference) element in which the polynomials are defined.

The DG formulation is then of the form: find $\mathbf{u}_h \in V_h$ and $\mathbf{q}_h \in \Sigma_h$ such that for all $K \in \mathcal{T}_h$,

$$\begin{aligned} \int_K \mathbf{q}_h \cdot \mathbf{r} \, dx &= - \int_K \mathbf{u}_h \nabla \cdot \mathbf{r} \, dx + \int_{\partial K} \hat{\mathbf{u}} \, \mathbf{r} \cdot \mathbf{n} \, ds \qquad \forall \mathbf{r} \in [\mathcal{P}_p(K)]^{dm} , \\ \int_K \frac{\partial \mathbf{u}_h}{\partial t} \mathbf{v} \, dx - \int_K [\mathbf{F}^{(i)}(\mathbf{u}_h) - \mathbf{F}^{(v)}(\mathbf{u}_h, \mathbf{q}_h)] \cdot \nabla \mathbf{v} \, dx & \\ = \int_K \mathbf{S}(\mathbf{u}_h, \mathbf{q}_h) \mathbf{v} \, dx - \int_{\partial K} [\hat{\mathbf{F}}^{(i)} - \hat{\mathbf{F}}^{(v)}] \cdot \mathbf{n} \, \mathbf{v} \, ds \qquad & \forall \mathbf{v} \in [\mathcal{P}_p(K)]^m . \end{aligned}$$

Here, the numerical fluxes $\hat{\mathbf{F}}^{(i)}$, $\hat{\mathbf{F}}^{(v)}$ and $\hat{\mathbf{u}}$ are approximations to $\mathbf{F}^{(i)}$, $\mathbf{F}^{(v)}$ and $\mathbf{u}$, respectively, on the boundary ∂K of the element K. The DG formulation is complete once these numerical fluxes are specified in terms of $\mathbf{q}_h$ and $\mathbf{u}_h$, and the boundary conditions set.

The inviscid flux $\hat{\mathbf{F}}^{(i)}$ is determined using Roe's scheme (Roe, 1981) and provides the numerical dissipation needed for ILES. The viscous flux $\hat{\mathbf{F}}^{(v)}$ is calculated using the Compact Discontinuous Galerkin (CDG) method introduced by Peraire and Persson (2008): by choosing the numerical flux $\hat{\mathbf{u}}$ to be a function of $\mathbf{u}_h$ and not $\mathbf{q}_h$,

the additional $\mathbf{q}_h$ variables can be eliminated after discretization at element level. This results in a system involving only the degrees of freedom corresponding to the conserved variables $\mathbf{u}_h$. The final result is a system of coupled ordinary differential equations of the form

$$\boldsymbol{M}\dot{\boldsymbol{u}} = \boldsymbol{R}(\boldsymbol{u}) \ , \tag{3.9}$$

where $\boldsymbol{u}$ is a vector containing the degrees of freedom associated with $\mathbf{u}_h$, and $\dot{\boldsymbol{u}}$ denotes its time derivative. Here, $\boldsymbol{M}$ is the mass matrix and $\boldsymbol{R}$ is the residual vector which is a nonlinear function of $\boldsymbol{u}$. Nodal basis expansions are used to represent $\mathbf{u}_h$ inside each element.

The system (3.9) is linearized using Newton's method and the resulting linear system solved using Conjugate Gradient Squared (CGS) preconditioned by incomplete factorizations (ILU) following Persson and Peraire (2008). The code is parallelized using a domain-decomposition approach with block-wise ILU factorizations, the details of which can be found in the paper by Persson (2009).

3.3 Computational Grids

The flow around a rectangular, constant-chord, wing with an SD7003 airfoil profile at an angle of attack of 4° and free-stream Mach number of 0.2 is considered. Unless otherwise specified, the wing span-to-chord ratio is set to 0.2 following the findings of Galbraith and Visbal (2008). The axes are set with x being the chord-wise direction and y the span-wise direction, such that the leading-edge is located along the line $x = 0$, $z = 0$.

From the wing's leading-edge line, the domain extends 4.3 chord lengths upstream, 7.4 chord lengths downstream, 5.9 chord lengths above, and 6.0 chord lengths below. Thus, if we denote by c the chord length, the domain has the range [-4.3c , 7.4c] $\times$ [0 , 0.2c] $\times$ [-6.0c , 5.9c] along the chord-wise, span-wise, and vertical directions, respectively.

The computational domain has periodic boundary conditions along the span-wise direction in order to simulate an infinite wing. The wing's surface is represented by a non-slip, adiabatic boundary condition, while a free-stream type boundary condition employing Roe's approximate Riemann solver is imposed at the outer edges (far-field) of the computational domain.

We use the term *high-order nodes* to refer to all the nodes used in the numerical procedure at which the variable states are computed, so as to differentiate them

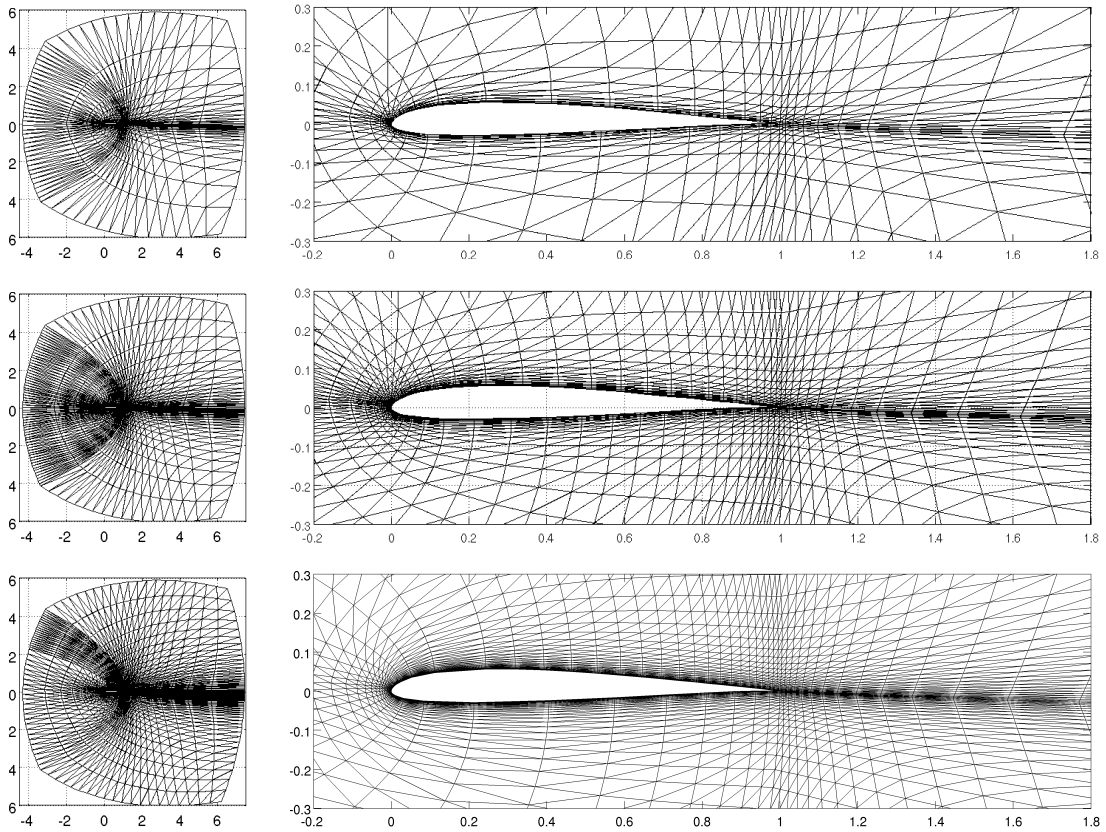

Figure 3-1: Span-wise view of the coarse (top: grid 1), medium (middle: grid 2), and fine (bottom: grid 3) computational grids: domain (left) and closer foil view (right).

from the nodes at the corners of each tetrahedral element. Note that the number of high-order nodes is equal to the number of degrees-of-freedom per state.

The grids are constructed by extruding a two-dimensional structured C-mesh around the profile which is generated from a rectangular grid by conformal transformations. To obtain curved elements that are aligned with the geometry boundaries and do not intersect, a fine structured grid is generated and the high-order nodes of the computational mesh placed at the mesh points of this fine grid. Note that this fine grid is such that the number of subdivisions in each direction is compatible with the number of high-order nodes required for a given polynomial order. The tetrahedral connectivities of the computational mesh are then obtained directly from the cartesian topology of the fine structured grid by splitting each cartesian cell into six tetrahedrals. The boundaries are thus represented accurately and a high-order mesh appropriate for DG computations obtained.

In order to investigate how much spatial resolution is needed to capture the transition to turbulence that occurs along the separation bubble, three computational grids

Table 3.1: Characteristics of the computational grids employed for the unswept wing.

Grid and polynomial order	Number of elements	Number of high-order nodes	Number of unique high-order nodes upper surface	span-wise
grid 1, $p = 3$	21,504	430,080	61	13
grid 2, $p = 3$	52,800	1,056,000	108	13
grid 2, $p = 4$		1,848,000	144	17
grid 3, $p = 4$	85,500	2,992,500	162	21

are considered: a coarse grid (hereafter referred to as grid 1) with 21,504 tetrahedral elements, a medium grid (grid 2) with 52,800 elements, and a fine grid (grid 3) with 85,500 elements. Figure 3-1 shows the computational grids on a planar cut along the span-wise direction.

Table 3.1 summarizes the characteristics of the different grids employed. For grid 1, third-order polynomials ($p = 3$) are employed for a fourth-order accurate method in space, thus giving 430,080 high-order nodes. For grid 2, both third-order and fourth-order ($p = 4$) polynomials are used, resulting in two refinement levels: one with 1,056,000 high-order nodes and the other one with 1,848,000. In the span-wise direction, both grids 1 and 2 have 4 elements, thus providing 13 and 17 unique nodes along the span at $p = 3$ and $p = 4$, respectively. Grid 3 has 15% more points than grid 2 in each direction (around the foil, radially, and along the span), and we use it with $p = 4$ for a total of 2,992,500 high-order nodes. Note that the factor of 1.15 in grid spacing h corresponds to a factor of 2 in the convergence rate h^{p+1} of the DG method for smooth problems with $p = 4$.

Throughout this work, $p = 3$ is used whenever no polynomial order is specified.

3.4 Time Stepping and Averaging Procedure

Time stepping is performed with a two-stage, A-stable, third-order accurate diagonal implicit Runge-Kutta (DIRK) method (Alexander, 1977). This allows to take large time steps chosen based on physical time accuracy considerations and not on numerical stability factors. Unless otherwise specified, the simulations are performed with a non-dimensional time step of $dt^* = dt \times U_\infty/c = 0.01$, and the solution is saved every 5 steps ($\Delta t^* = 0.05$) for computing statistics and other post-processing tasks.

For all the cases considered, the flow is initialized to a uniform field at the far-field conditions. The initial transient is over by $t^* = 15$ as estimated from the temporal

evolution of the forces on the wing. Hence, unless otherwise specified, the average fields, turbulence correlations, and statistics are computed by averaging the solution over a non-dimensional time interval of 10 which corresponds to 200 solutions with $t^* \in [15, 25]$, and then performing a spatial average over 20 span-wise planes (unless otherwise specified) since the domain is span-wise periodic.

For the spatial averaging, the solution is interpolated (to an order compatible with the polynomial order being used so as to avoid introducing interpolation errors) at 20 x-z planes equally-spaced along the span and then these 20 interpolated planar solutions are averaged.

3.5 Angle of Attack for Comparisons with XFOIL

XFOIL (Drela, 2002) is a two-dimensional, steady, potential flow solver with an interactive boundary layer coupling and an e^N envelope method for transition prediction (Drela and Giles, 1987). It was developed for the design and analysis of subsonic airfoils, and has been extensively validated and used as reference for the study of a wide variety of airfoils.

The Navier-Stokes methods apply the specified free-stream angle $\alpha = 4^\circ$ at the domain's outer inflow boundary. The missing vortex upwash at the inlet due to the airfoil's presence gives a decrease in the effective angle of attack seen by the airfoil by the amount, in radians,

$$\Delta\alpha = -\frac{C_L}{4\pi\, r/c}$$

where C_L is the airfoil lift coefficient and r/c is the distance-to-chord ratio between the inlet boundary and the wing's lift centroid, such that the higher-order y-doublet far-field term is exactly zero. The distance between the airfoil's leading edge and the center of lift can be approximated using the moment coefficient C_M by

$$\frac{x_L}{c} = \frac{1}{4} - \frac{C_M}{C_L}\ .$$

The domain extends $4.3\,c$ upstream of the leading edge, and hence $r/c = 4.3 + x_L/c$. Note that the $\Delta\alpha$ correction is only significant when the domain inflow boundary is close to the foil as in the present work.

Since XFOIL fully accounts for the farfield vortex, it has been run at the smaller angle of attack $\alpha_{XFOIL} = \alpha + \Delta\alpha$ in order to give a more correct comparison to the Navier-Stokes results. As an approximation, the lift and moment coefficients for com-

Table 3.2: Angle of attack correction, $\Delta\alpha$, and angle of attack for XFOIL computations, α_{XFOIL}, for the three Reynolds numbers considered.

Reynolds Number	$C_L(4°)$	$C_M(4°)$	x_L/c	$\Delta\alpha$	α_{XFOIL}
$10,000$	0.2842	-0.0167	0.3088	$-0.2812°$	$3.72°$
$22,000$	0.4083	-0.0466	0.3641	$-0.3991°$	$3.60°$
$60,000$	0.6370	-0.0347	0.3045	$-0.6308°$	$3.37°$

puting $\Delta\alpha$ are obtained from XFOIL at the nominal 4° angle of attack. Table 3.2 gives the angle of attack correction and effective angle of attack for the different Reynolds numbers considered in the present work; these are the result of an approximation and the exact inflow boundary conditions for the present simulations have their own uncertainty. The critical amplification factor in XFOIL is set to $N_{crit} = 7$ unless otherwise specified.

Alternatively, one can perform an inviscid simulation and then set XFOIL to match the inviscid lift coefficient. A two-dimensional Euler run on grid 2 resulted in an average value of $C_L = 0.6680$ which requires the angle of attack in XFOIL to be 3.83°. However, using this value for the different Reynolds numbers considered here did not provide a better agreement than using the angle of attack to α_{XFOIL}.

No tailoring of XFOIL (angle of attack, N_{crit} value, changing correlations for separated flow) allowed us to obtain the same pressure and friction forces of the present simulations. This indicates that the flows involved are significantly different from the ones encountered in typical high Reynolds numbers aerodynamic applications for which XFOIL has proven to be a reference for many years. In particular, some of the cases studied here exhibit strong three-dimensional and unsteady effects which are outside the domain of applicability of XFOIL. Hence, whenever comparisons with XFOIL's results are given, it is important to keep in mind that such a comparisons provide merely a preliminary check.

3.6 Visualizing Vortical Structures: Q-Criterion

A systematic way of identifying vortical coherent structures in a flow is to use the q-criterion proposed by Dubeif and Delcayre (2000) and defined as

$$q \equiv \frac{1}{2}\left(\Omega_{ij}\Omega_{ij} - S_{ij}S_{ij}\right) , \tag{3.10}$$

where Ω_{ij} and S_{ij} are the anti-symmetric and symmetric parts of the velocity gradient, respectively, that is

$$\Omega_{ij} \equiv \frac{1}{2}\left(\frac{\partial u_i}{\partial x_j} - \frac{\partial u_j}{\partial x_i}\right) \quad \text{and} \quad S_{ij} \equiv \frac{1}{2}\left(\frac{\partial u_i}{\partial x_j} + \frac{\partial u_j}{\partial x_i}\right) \ .$$

The q-criterion represents the balance between the rate of vorticity $\Omega_{ij}\Omega_{ij}$ and the rate of strain $S_{ij}S_{ij}$. In the core of a vortex, $q > 0$ since vorticity increases as the center of the vortex is approached. Thus, regions of positive q-criterion correspond to vortical structures[1]. In the present work iso-surfaces of positive q are used to visualize these structures, with the velocity gradients computed consistently with the DG method (*i.e.* using the variables $\mathbf{q}$) to preserve the order of accuracy.

3.7 Boundary Layer Analysis

In order to compute the boundary layer integral quantities, we first obtain the pseudo-velocity profile by integrating the flow vorticity, namely

$$\vec{u}^*(x,n) = \int_0^n \vec{\omega} \times \hat{n}\, dn \ . \tag{3.11}$$

Here $\vec{u}^*$ denotes the pseudo-velocity, $\vec{\omega}$ the flow vorticity vector, $\hat{n}$ the unit vector normal to the airfoil at the location considered, and n the local coordinate along $\hat{n}$ with the wall located at $n = 0$. The reason for using this pseudo-velocity profile instead of the flow velocity is that it always asymptotes outside the boundary layer, even with strong curvature, thus making the edge of the boundary layer a well defined location.

The edge n_e of the boundary layer is then taken to be the location where *both* the magnitudes of vorticity, $|\vec{\omega}|$, and of vorticity's normal variation, $|\partial\vec{\omega}/\partial n|$, are below a certain threshold, namely

$$\begin{cases} |\vec{\omega}|\, n < \epsilon_0 |\vec{u}^*| \,, \\ \left|\dfrac{d\vec{\omega}}{dn}\right| n^2 < \epsilon_1 |\vec{u}^*| \,. \end{cases} \tag{3.12}$$

[1] For an incompressible flow, the q-criterion can be written using the flow vorticity ω as

$$q = \frac{1}{4}\left(\omega^2 - 2S_{ij}S_{ij}\right) = \frac{1}{2}\frac{\nabla^2 p}{\rho}$$

which shows the relation to the low pressure region at the center of a vortex.

The edge velocity is then $\vec{u}_e^* = \vec{u}^*(n_e)$ and has the magnitude $u_e = |\vec{u}_e^*|$. The values $\epsilon_0 = 0.01$ and $\epsilon_1 = 0.1$ were found to allow for a robust and systematic detection of the boundary layer edge for the simulations reported in the present work.

Local streamwise and cross-flow unit vectors are then defined as, respectively,

$$\hat{s}_1 \equiv \vec{u}_e^*/u_e \quad \text{and} \quad \hat{s}_2 \equiv \hat{s}_1 \times \hat{n} \ . \tag{3.13}$$

Thus, the streamwise and cross-flow velocity profiles are respectively given by

$$u_1(x,n) = \vec{u}^*(x,n) \cdot \hat{s}_1 \quad \text{and} \quad u_2(x,n) = \vec{u}^*(x,n) \cdot \hat{s}_2 \ . \tag{3.14}$$

The boundary layer streamwise displacement and momentum thicknesses are then

$$\delta_1^* = \int_0^{n_e} \left(1 - \frac{u_1}{u_e}\right) dn \tag{3.15}$$

$$\theta_{11} = \int_0^{n_e} \left(1 - \frac{u_1}{u_e}\right) \frac{u_1}{u_e} \, dn \tag{3.16}$$

with the streamwise shape factor

$$H_{11} = \delta_1^*/\theta_{11} \ . \tag{3.17}$$

Note that the boundary layer analysis relies on quantities at points along lines normal to the foil's surface. These are obtained by interpolating within the grid's tetrahedral elements in a manner consistent with the order of the polynomials being used in order to preserve the accuracy of the method. Moreover, as many stations along the foil chord are employed as there are unique grid nodes, and about 100 points inside the boundary layer along the normal are taken.

3.8 Transition Mechanism

In order to identify which mechanism is responsible for transition to turbulence, we compute the fluctuating streamwise pseudo-velocity

$$u_1'(x,t) = u_1(x,t) - \overline{u}_1(x) \ ,$$

in which the over-line denotes a temporal average. The increase in perturbation amplitude of disturbances along the chord-wise direction is then quantified by computing

the amplification A_1 of streamwise perturbations at any location x along the chord, that is

$$A_1(x) = \frac{1}{\overline{u_e}(x)\sqrt{n_e(x)}} \sqrt{\int_0^{n_e} \overline{u_1'^{\,2}}\, dn} \quad . \tag{3.18}$$

The amplification factor N_1 of the streamwise perturbations is then

$$N_1(x) = \ln\left(\frac{A_1(x)}{A_{1_0}}\right) \quad , \tag{3.19}$$

in which A_{1_0} is the amplification at the onset of transition, or equivalently

$$e^{N_1} = \frac{A_1(x)}{A_{1_0}} \quad .$$

Similarly, the amplification of cross-flow instabilities can be assessed by computing

$$A_2(x) = \frac{1}{\overline{u_e}(x)\sqrt{n_e(x)}} \sqrt{\int_0^{n_e} \overline{u_2'^{\,2}}\, dn} \tag{3.20}$$

to which corresponds the cross-flow amplification factor

$$N_2(x) = \ln\left(\frac{A_2(x)}{A_{2_0}}\right) \quad . \tag{3.21}$$

3.9 Transition Model

When the growth of unstable TS waves is the mechanism that drives transition to turbulence, the location where transition takes place can be predicted by following the growth of the amplification factor N of disturbances. As was discussed in Section 2.5.2, the successful e^N method relies on this idea but are not easily coupled with Navier-Stokes codes.

We are interested in devising a way to predict transition in Navier-Stokes codes without having to resolve all the flow features that are responsible for the breakdown to turbulence. In other words, we wish to be able to predict transition with computational grids that are much coarser than what LES and DNS require. In particular, we are looking for a transition prediction technique that can be efficiently coupled with RANS type codes.

A way to achieve this goal is to introduce an additional equation to be solved in

RANS simulations which accounts for transition. M. Drela has proposed[2] the simple idea of tracking the amplification factor N of disturbances within the boundary layer through a transport equation, which can be coupled with standard turbulence models through either a trip term, or a production-limiting coefficient, based on N. This approach, as proposed by M. Drela, is summarized here.

The equation for the amplification factor N has the form of a standard transport equation and reads

$$\frac{\partial N}{\partial t} + \nabla_s \cdot (\vec{u}_c\, N) = \nu_N \nabla_s^2 N + \frac{|\vec{u}_c|}{\theta_{11}} f\left(H_{11}, Re_{\theta_{11}}\right) , \tag{3.22}$$

in which θ_{11} and H_{11} are the streamwise momentum thickness and shape factor, respectively, computed through the boundary layer analysis, and $Re_{\theta_{11}}$ the Reynolds number based on θ_{11}. Note that N is a function of time and of the local streamwise and cross-flow directions, that is $N = N(s_1, s_2, t)$. The convection velocity of unstable waves, $\vec{u}_c$, is taken to be a fraction of the boundary layer edge velocity, that is

$$\vec{u}_c \equiv k_c\, \vec{u}_e \tag{3.23}$$

for $0 < k_c \leq 1$. The symbol ∇_s represents the surface gradient operator

$$\nabla_s \equiv \hat{s}_1 \frac{\partial}{\partial s_1} + \hat{s}_2 \frac{\partial}{\partial s_2} . \tag{3.24}$$

The left-hand-side of the transport equation (3.22) accounts for convection, and the first term on the right-hand-side represents diffusion through a viscosity coefficient ν_N which provides stabilization and can be expressed in a manner consistent with dimensional analysis as

$$\nu_N = \epsilon_N\, |\vec{u}_c|\, \Delta_{grid} , \tag{3.25}$$

where Δ_{grid} is a measure of grid spacing and ϵ_N has a small non-dimensional value. The source term (second term on the right-hand side) models the growth of streamwise TS disturbances and the function $f\left(H_1, Re_\theta\right)$ represents the e^N envelope proposed by Drela and Giles (1987), namely

$$f\left(H_{11}, Re_\theta\right) = \frac{dN}{dRe_\theta}\left(H_{11}\right) \frac{m(H_{11}) + 1}{2}\, \ell(H_{11}) \tag{3.26}$$

in which the functions dN/dRe_θ, m, and ℓ are given by empirical correlations.

[2] personal communication during the fall 2006

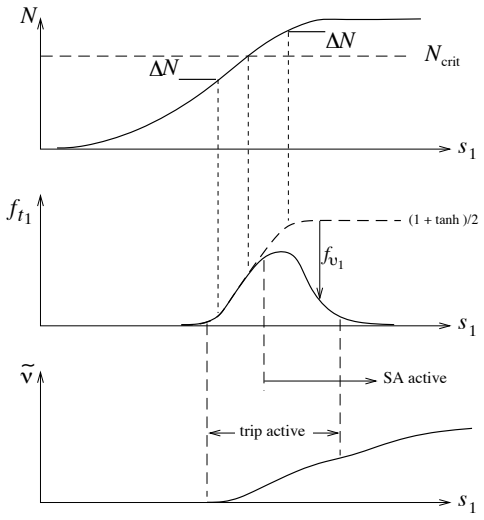

Figure 3-2: Expected streamwise evolution of amplification factor N, trip term for SA model f_{t_1}, and model variable $\tilde{\nu}$. [Figure by M. Drela]

The boundary condition for the transport equation sets $N = 0$ at any outflow cell, that is on any element for which $\vec{u}_c \cdot \hat{n} > 0$ on all its faces of outward normal $\hat{n}$. This is actually an initial condition which in practice sets zero amplification at the stagnation point, from which point on the amplification growth is tracked.

The transition equation (3.22) can be coupled with the SA RANS turbulence model of Spalart and Allmaras (1994) by setting the trip term to

$$f_{t_1} = c'_{t_1} (1 - f_{v_1}) \left[1 + \tanh \frac{N - N_{crit}}{\Delta N} \right] \left[1 - \frac{n}{n_e} \right] \tag{3.27}$$

when the local normal coordinate n is in the range $[0, n_e]$. The SA model consists on an equation for the model variable $\tilde{\nu}$ which is related to the eddy viscosity. A schematic of the expected streamwise evolutions of N, f_{t_1}, and $\tilde{\nu}$ can be seen in Figure 3-2. Note that the form of (3.27) ensures that the trip term is only effectively active over a region close to the location where N reaches the critical amplification factor N_{crit}.

This approach has the disadvantage of using boundary layer integral parameters, which can be difficult to obtain in unstructured codes. However, it does rely on a systematic and accurate way to determine the boundary layer edge (see Section 3.7) and can be easily coupled with standard turbulence models for RANS simulations.

Cross-flow instabilities could be treated in the same way, and one could have a two-equation transition model with equations for the amplification factors N_{TS} and N_{CF} of TS waves and cross-flow disturbances. However, no correlation exists which

could be used as a source term to represent the growth of cross-flow waves. One might instead attempt to find a correction for the streamwise source (3.26) that would account for the influence of the boundary layer cross-flow velocity on the stability of the streamwise velocity profile and thus model mixed transition. This is however outside the scope of the present research.

Chapter 4

Flow Around an Infinite Wing

In the present chapter, results are presented for the flow around a stationary infinite SD7003 wing at an angle of attack of 4°, for Reynolds numbers of 10,000, 22,000, and 60,000 with a free-stream velocity perpendicular to the leading edge line. For each case, a grid study is performed in order to ensure that the average quantities are converged, significant flow features (instantaneous and average) are described, and the average boundary layer on the upper surface of the wing is analysed.

As expected, the chord-wise extent of separation decreases while both separation and transition move upstream as the Reynolds number is increased. Some comparisons with previously published results are provided, and it is established that the transition that takes place along the laminar separation bubble at $Re = 22,000$ and $Re = 60,000$ is a natural one resulting from the growth of linear Tollmien-Schlichting waves. Sections 4.1–4.3 constitute the contents of a journal paper that has been accepted for publication (Uranga et al., 2010). An additional section looks at the N-factor evolution predicted by the proposed transition model equation.

4.1 Laminar Regime: $Re = 10,000$

The first case considered is the flow at a Reynolds number of 10,000. In this regime, the flow is found to be fundamentally two-dimensional with little variation along the span-wise direction and periodic vortex shedding. Comparison is made with a two-dimensional simulation performed on a grid with the same resolution as a span-wise plane of the three-dimensional grid 2. While the instantaneous forces of Figure 4-1 differ slightly in magnitude, with smaller amplitudes for the three-dimensional case due to three-dimensional alleviation, the shedding period and average values are es-

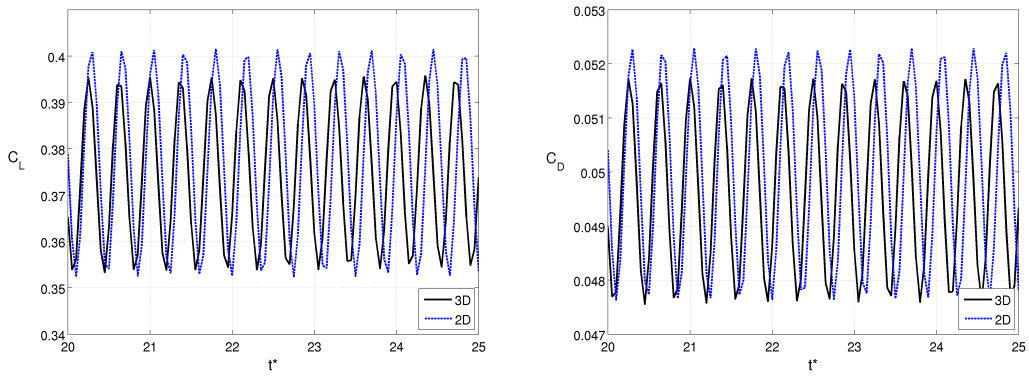

Figure 4-1: Time variation of lift (left) and drag (right) coefficients at $Re = 10,000$ on grid 2: comparison of 2D and 3D simulations.

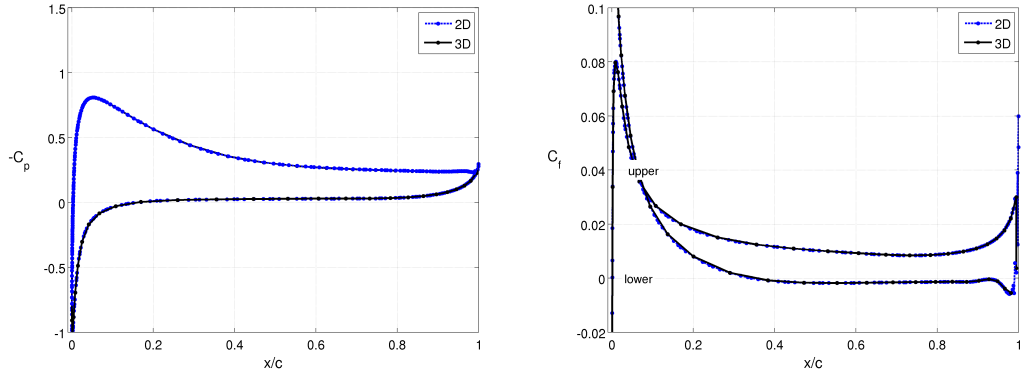

Figure 4-2: Average pressure coefficient (left) and chord-wise skin friction coefficient (right) at $Re = 10,000$ on grid 2: comparison of 2D and 3D simulations.

Table 4.1: Average flow results at Reynolds 10,000.

Source	Separation x_{sep}/c	Transition x_{tr}/c	Reattachment x_r/c	C_L	C_D
XFOIL at 3.72°, $N_{crit} = 7$	0.3543	-	-	0.2711	0.04578
grid 1	0.3658	0.9371	-	0.3824	0.04999
difference with grid 2	2.8%	−0.1%	-	2.2%	0.64%
grid 2, 2D	0.3451	0.9384	-	0.3755	0.04978
difference with grid 2	−3.0%	0%	-	0.32%	0.22%
grid 2	0.3557	0.9384	-	0.3743	0.04967
difference with XFOIL	0.39%	-	-	38%	8.5%

sentially the same. The average lift coefficient is 0.3743, the average drag coefficient is 0.04967, while the average span-wise force coefficient is of the order of 10^{-6}. The difference in lift and drag coefficients of the two-dimensional simulations relative to the three-dimensional run is less than 0.32% and 0.23%, respectively. Furthermore, the 2D and 3D curves for average pressure and chord-wise skin friction coefficients are undistinguishable as can be seen in Figure 4-2.

Note that the force coefficients are those of the time-averaged flow, and not exactly equal to the average of the force time variations; that is, the flow time average is computed first and then the forces of that time-averaged flow are evaluated. The difference in values between these two ways of obtaining force averages is usually insignificant (a couple percent or less). We choose this approach so as to be consistent with the rest of the analysis (wall stresses, boundary layer quantities) which considers the time-averaged flow. Furthermore, this is closer to what would be obtained from a

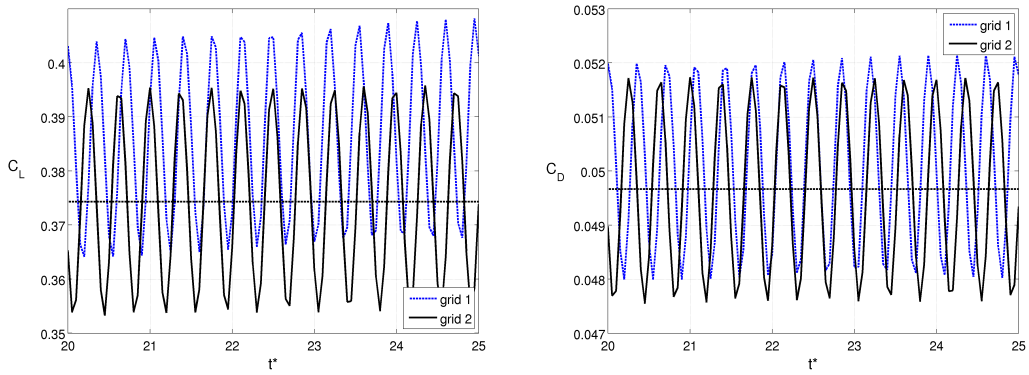

Figure 4-3: Time variation of lift (left) and drag (right) coefficients at $Re = 10,000$: comparison between grids 1 and 2. The dotted horizontal line indicates the average values for grid 2.

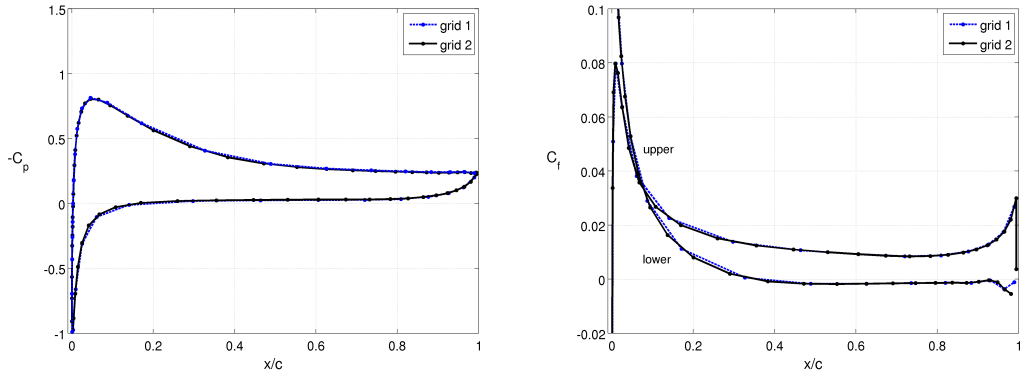

Figure 4-4: Average pressure coefficient (left) and chord-wise skin friction coefficient (right) at $Re = 10,000$ on grid 2: comparison between grids 1 and 2.

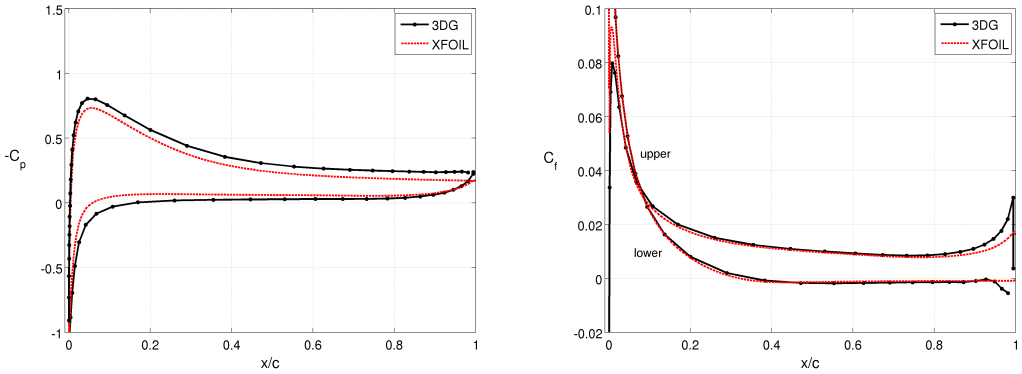

Figure 4-5: Average pressure coefficient (left) and chord-wise skin friction coefficient (right) at $Re = 10,000$ on grid 2. The dashed lines give XFOIL predictions at 3.72° angle of attack, $N_{crit} = 7$.

RANS simulation, towards which the transition model we start developing is targeted.

The effect of grid resolution is assessed by comparing the results obtained on grids 1 and 2. No significant difference is observed on average quantities, and the pressure and skin friction coefficient plots for the two grids fall on top of each other (Figure 4-4), while the average lift and drag coefficients for grid 1 differ by only 2.2% and 0.64%, respectively, from those for grid 2. On the other hand, there is a small but appreciable difference in the time history of the forces of Figure 4-3. Thus, grid 2 has sufficient resolution to capture the *mean* flow characteristics at $Re = 10,000$ even though the time-varying features are not fully accounted for.

Furthermore, undistinguishable pressure and skin friction curves are obtained when performing a spatial average over 10 span-wise planes instead of over 20 gives, or when averaging over 100 solutions instead of over 200. The statistics obtained with 200 solutions and 20 span-wise planes at this regime are thus properly converged.

Figures 4-5 shows the average pressure and chord-wise skin friction coefficients, together with the results predicted by XFOIL (Drela, 2002) at an angle of attack of 3.72° as justified in Section 3.5. The similarity with XFOIL provides a good check for the present simulations, but the two approaches may not correspond to precisely the same farfield conditions. First, the angle of attack correction is only an approximation. Furthermore, the critical amplification factor, N_{crit}, at which transition is set to occur (a user-defined parameter in XFOIL) is correlated to the level of free-stream disturbances, and it is unclear what the value for a simulation should be. In the present case, setting N_{crit} to 4.6 in XFOIL results in a match in transition location.

The iso-surfaces of q-criterion of Figure 4-8 show that coherent vortical structures

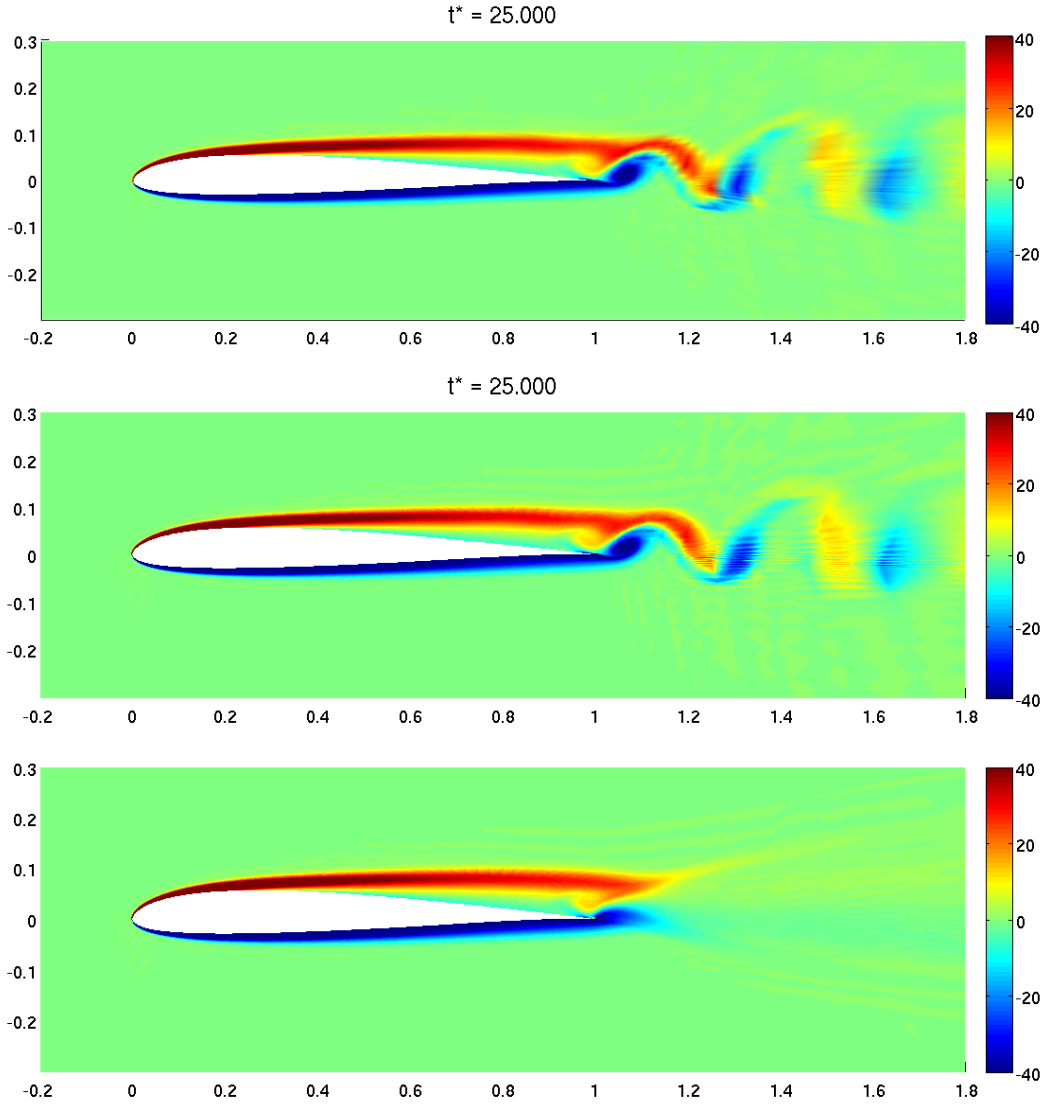

Figure 4-6: Span-wise vorticity at $Re = 10,000$ with grid 2: instantaneous on middle plane (top), instantaneous span-wise average (middle), and average (bottom) contours.

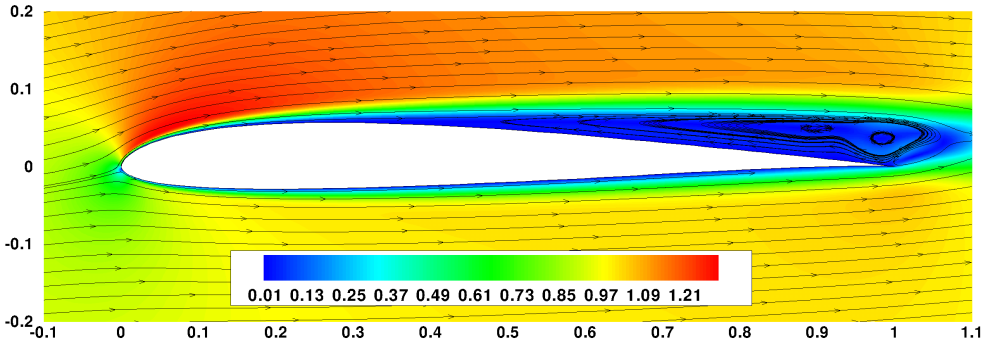

Figure 4-7: Average streamlines and contours of velocity magnitude at $Re = 10,000$ with grid 2.

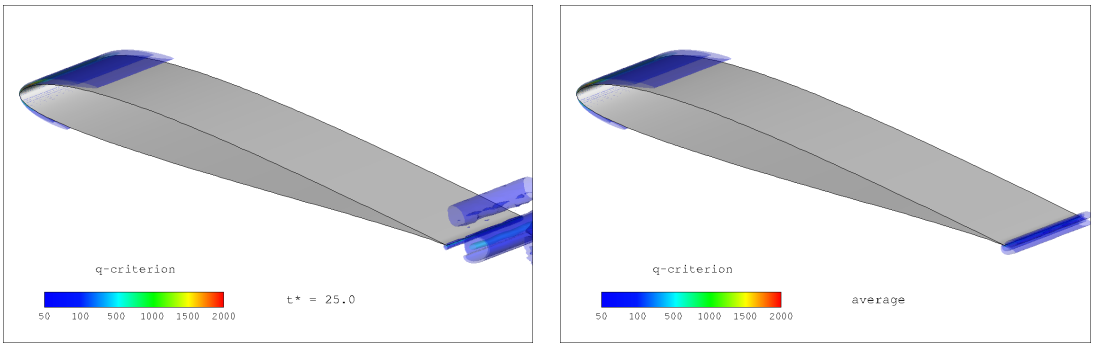

Figure 4-8: Instantaneous (left) and time average (right) iso-surfaces of q-criterion at $Re = 10,000$ with grid 2.

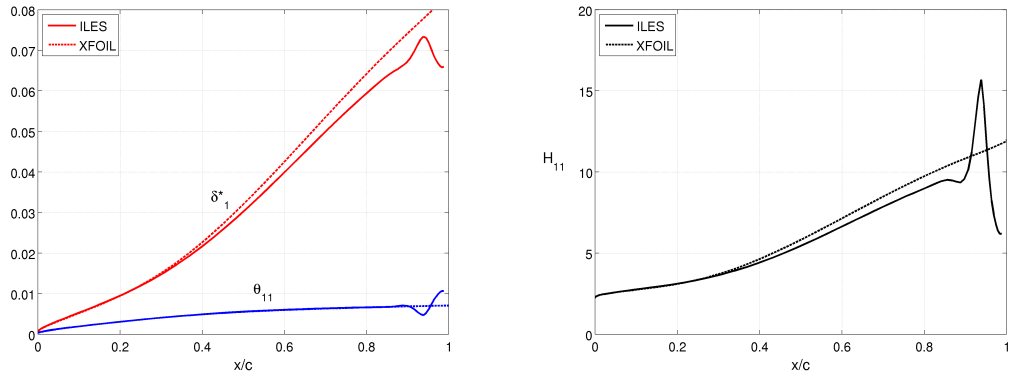

Figure 4-9: Boundary layer average streamwise displacement and momentum thicknesses (left), and shape factor (right) evolution along the chord-wise direction at $Re = 10,000$ with grid 2. The dashed lines give XFOIL predictions at 3.72° angle of attack, $N_{crit} = 7$.

are not present upstream of the trailing edge but only in the wake. Furthermore, the instantaneous iso-surfaces have a straight cylindrical shape with no variation along the span-wise direction thus indicating that the wake structures remain two-dimensional.

At this Reynolds number, the boundary layer separates at around 36% of the chord from the leading edge, and does not reattach. This can be seen on the friction coefficient distribution of Figure 4-5, on the instantaneous and average span-wise vorticity contours as shown in Figure 4-6, and on the average stream-lines shown in Figure 4-7. Furthermore, the flow structures are all relatively large with only pairs of well-defined vortices being shed (see Figure 4-6).

The curves of streamwise displacement thickness, δ_1^*, momentum thickness, θ_{11}, and shape factor, $H_{11} = \delta_1^*/\theta_{11}$, of Figure 4-9 confirm that transition to turbulence occurs only at 94% of the chord. Furthermore, the curves for two-dimensional simulations and for grid 1 are undistinguishable from those of grid 2. The main difference

between the boundary layer evolution as predicted by XFOIL (dashed lines in the figures) and the one resulting from the present ILES is that the latter predicts a transition to turbulence just upstream of the trailing edge as evidenced by the peak in shape factor, while the former does not. However, the shape factor peak in the ILES is very close to the trailing edge and might not represent an actual transition but rather a lack of resolution.

4.2 Low Transitional Regime: $Re = 22,000$

4.2.1 Three-Dimensionality

The flow at $Re = 22,000$ is now considered. As is shown later, the flow at this Reynolds number transitions to turbulence, and since turbulence is a fundamentally three-dimensional phenomena, we expect that a two-dimensional simulation would not be able to capture the important flow features. This is confirmed by comparing the three-dimensional results obtained on grid 2 with a two-dimensional simulation using, as previously, a grid with the same resolution as a span-wise plane.

With respect to the instantaneous force coefficients of Figure 4-10, it can be noted that the lift and drag force coefficients for the two-dimensional case have significantly larger magnitudes (by close to a factor of three) than those of the three-dimensional case. This is of course due to three-dimensional alleviating effects.

The pressure and skin friction profiles of Figure 4-11 also confirm the significance of three-dimensional effects, with the friction being more sensitive than the pressure, while largest discrepancies occur near transition ($x/c \approx 0.7$). However, a two-dimensional flow approximation yields separation, transition, and reattachment locations, as well as lift and drag coefficients, which are relatively close (less than 10%

Table 4.2: Average flow results at Reynolds 22,000.

Source	Separation x_{sep}/c	Transition x_{tr}/c	Reattachment x_r/c	Bubble Length	C_L	C_D
XFOIL at 3.60°, $N_{crit} = 7$	0.2489	0.7784	0.9494	$0.7005c$	0.5193	0.03772
grid 1	0.2744	0.6853	-	-	0.6359	0.04309
difference with grid 2	15%	0.60%			−1.5%	0.87%
grid 2, 2D	0.2144	0.6602	0.9554	$0.7410c$	0.6707	0.04510
difference with grid 2	−10%	−3.1%	1.9%	6.0%	3.9%	5.6%
grid 2	0.2386	0.6812	0.9379	$0.6993c$	0.6456	0.04272
difference with grid 2, $p = 4$	6.6%	0.95%	0.011%	−2.0%	−0.031%	−0.37%
grid 2, $p = 4$	0.2239	0.6748	0.9378	$0.7139c$	0.6458	0.04288
difference with XFOIL	−10%	−13%	−1.2%	1.9%	24%	14%

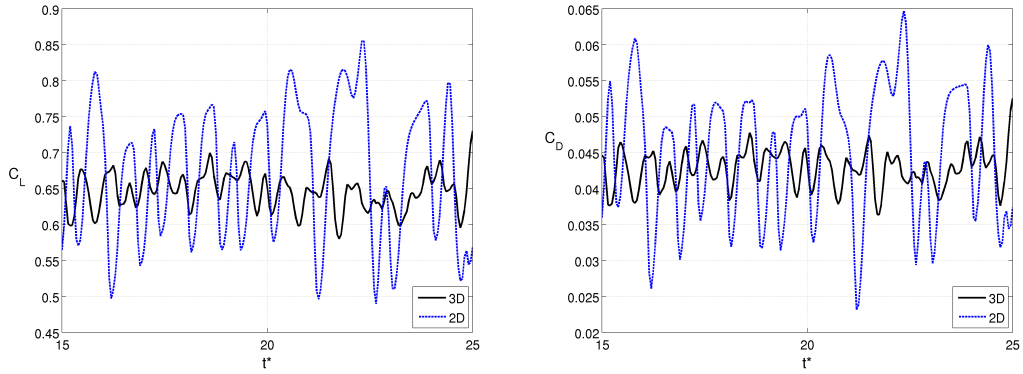

Figure 4-10: Time variation of lift (left) and drag (right) coefficients at $Re = 22,000$ on grid 2: comparison of 2D and 3D simulations.

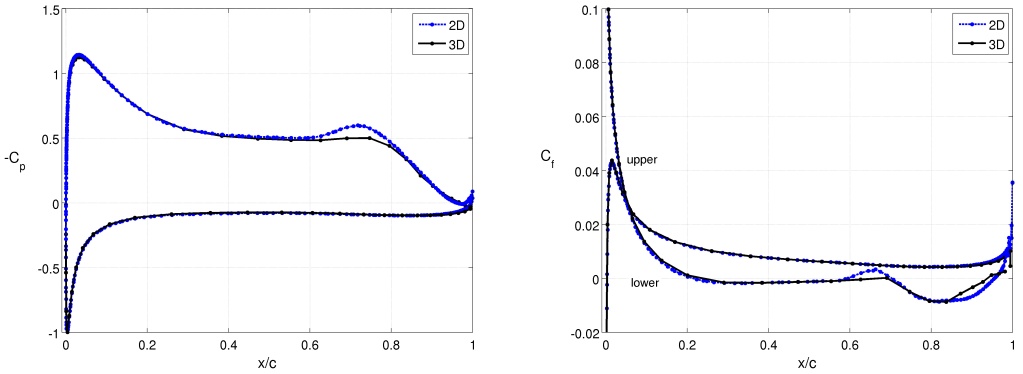

Figure 4-11: Average pressure coefficient (left) and chord-wise skin friction coefficient (right) at $Re = 22,000$ on grid 2: comparison of 2D and 3D simulations.

off) to the three-dimensional solution values as indicated by the numbers in Table 4.2.

4.2.2 Spatial Resolution: Grid Comparisons

In order to assess how much spatial resolution is needed at $Re = 22,000$, the flow is computed with three different resolution levels: grid 1 with $p = 3$, grid 2 with $p = 3$, and grid 2 with $p = 4$. The curves of average pressure coefficient and average skin friction coefficient profiles for the three levels are indistinguishable as can be seen in Figure 4-13. On the other hand, the instantaneous force histories of Figure 4-12 differ but have approximately the same magnitudes. They depict a turbulent signal and indicate an aperiodic vortex shedding with various scale sizes and frequencies. Furthermore, the span-wise force coefficient, while small (of the order of 10^{-4}), reveals the presence of span-wise flow motions. The average separation, transition, and

reattachment locations, as well as the lift and drag coefficients of the mean flow are given in Table 4.2.

The coarsest mesh employed (grid 1) is unable to provide an accurate enough solution for the flow to reattach to the wing. Note that the difference of 6.6% in separation location on grid 2 between results at $p = 3$ and $p = 4$ might partly be explained by the uncertainty in determining the separation location from the friction coefficient curve: the curve is close to horizontal near $C_f = 0$ and the value of x_s/c is linearly interpolated between two chord-wise locations. If one uses the shape factor to determine separation (taking it at a value of 4), the difference in location is significantly reduced; this approach is adopted for the swept-wing analysis.

Furthermore, the boundary layer chord-wise variation of streamwise displacement thickness and momentum thickness are not significantly different on grid 2 between solutions at $p = 3$ and at $p = 4$. However, the shape factor does show a discrepancy but only in the separation region ($H_{11} > 4$) and not in the transition location as can be seen in Figure 4-14. Thus, the results obtained on grid 2 with $p = 3$ can

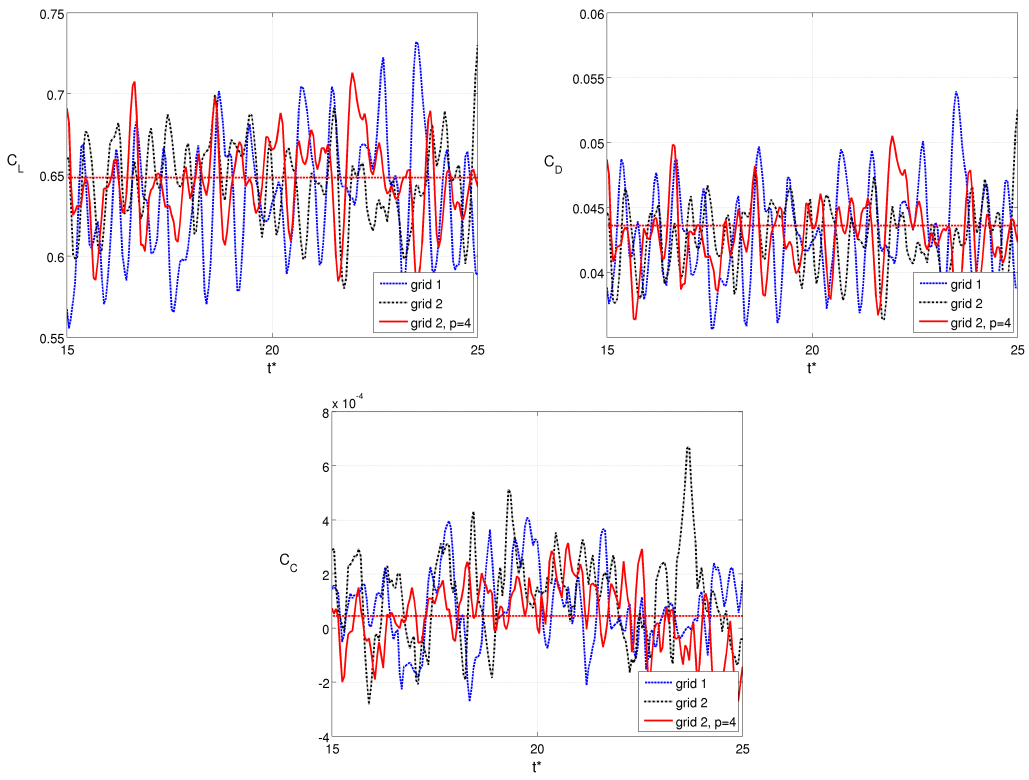

Figure 4-12: Time variation of lift (top left), drag (top right), and span-wise (bottom) force coefficients at $Re = 22,000$: comparison of results with different spatial resolutions. The dotted horizontal line indicates the average values for grid 2, $p = 4$.

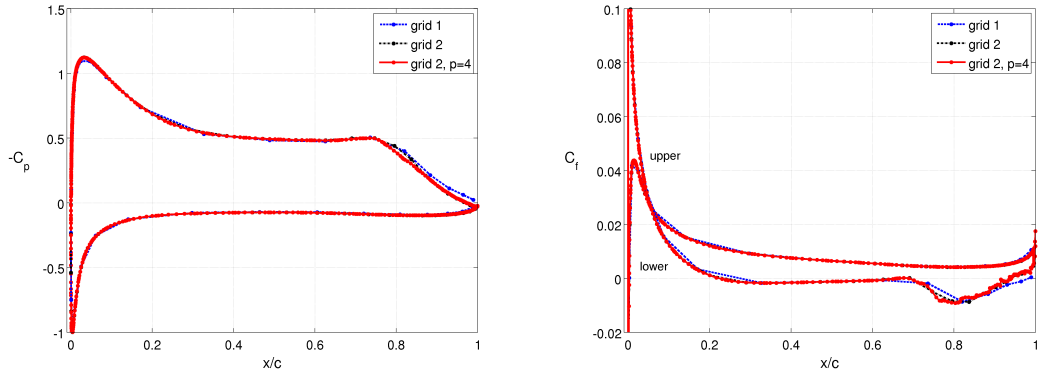

Figure 4-13: Average pressure coefficient (left) and chord-wise skin friction coefficient (right) at $Re = 22,000$: comparison of results with different spatial resolutions.

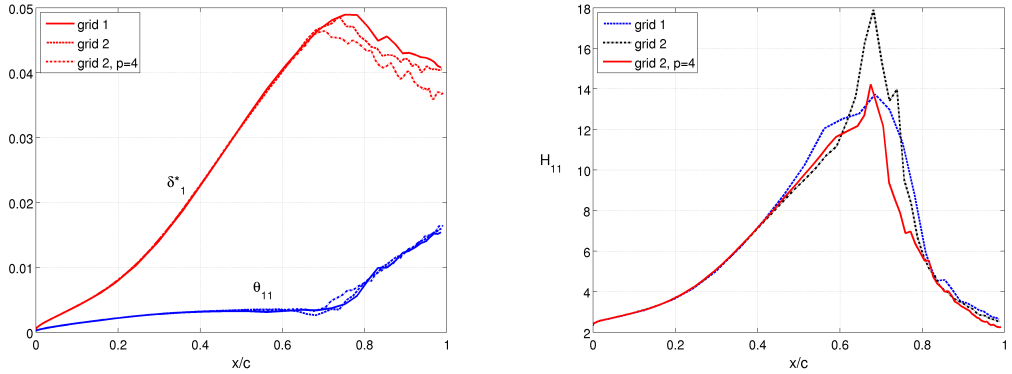

Figure 4-14: Boundary layer average streamwise displacement and momentum thicknesses (left), and shape factor (right) evolution along the chord-wise direction at $Re = 22,000$: comparison of results with different spatial resolutions.

be considered to be grid-converged with respect to global average quantities—with the exception of the peak in shape factor which is particularly hard to resolve—and this mesh is characteristic of the spatial resolution needed to resolve the mean flow features at $Re = 22,000$.

4.2.3 Results with Grid 2, $p = 3$

At this Reynolds number of 22,000, the separation bubble is clearly visible on the C_p profile of Figure 4-15 with the characteristic plateau. From the skin friction coefficient, separation is located at around 23% of the chord. Transition takes place after separation, at around 68% as measured from the peak in the boundary layer shape factor of Figure 4-20; this is also made visible by the velocity correlations of Figure 4-17 which show significant velocity fluctuations on the downstream part of

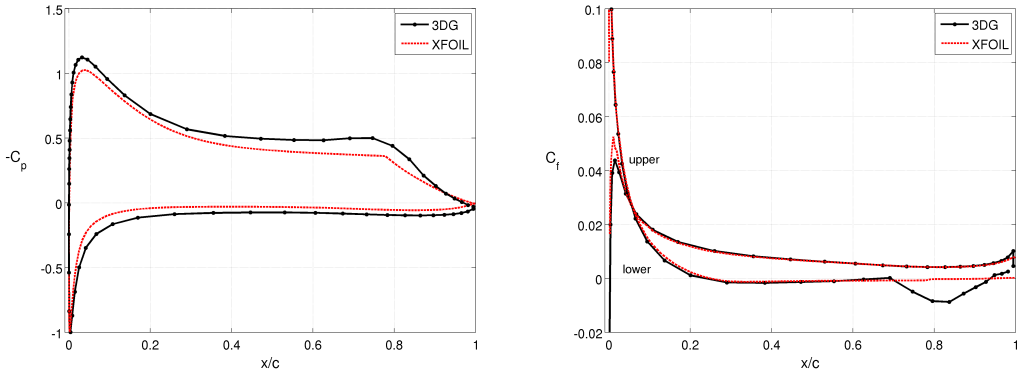

Figure 4-15: Average pressure coefficient (left) and chord-wise skin friction coefficient (right) at $Re = 22,000$ on grid 2. The dashed lines give XFOIL predictions at 3.60° angle of attack, $N_{crit} = 7$.

the foil. Finally, the flow reattaches at around 94% of the chord, thus forming a long laminar separation bubble (LSB) which encompasses more than 70% of the wing's chord. This LSB is made visible by the average streamlines of Figure 4-18.

Contrarily to what was observed at $Re = 10,000$, the instantaneous vorticity contours of Figure 4-16 contain a significant amount of small, high-frequency structures, and the flow is not anymore restricted to pairs of shed vortices. As already pointed out, the flow at this Reynolds number is three-dimensional and contains structures that vary in the span-wise direction. This can be seen in the instantaneous iso-surfaces of q-criterion and of span-wise vorticity of Figure 4-19: the iso-surfaces are not cylindrical and reveal significant span-wise variations. The presence of small variations in average q-criterion past transition might be due to traces of high-frequency structures and a time average which is not fully converged.

The comparison with XFOIL's predictions show some disagreement—see the pressure and friction profiles of Figure 4-15 and the boundary layer integral thickness evolutions of Figure 4-20—but the same remarks made for the $Re = 10,000$ case hold here, and the comparisons provide merely a consistency check. Transition, for instance, can be made to match by setting $N_{crit} = 5.2$ in XFOIL. Furthermore, the flow is three-dimensional and beyond the modeling capabilities of XFOIL.

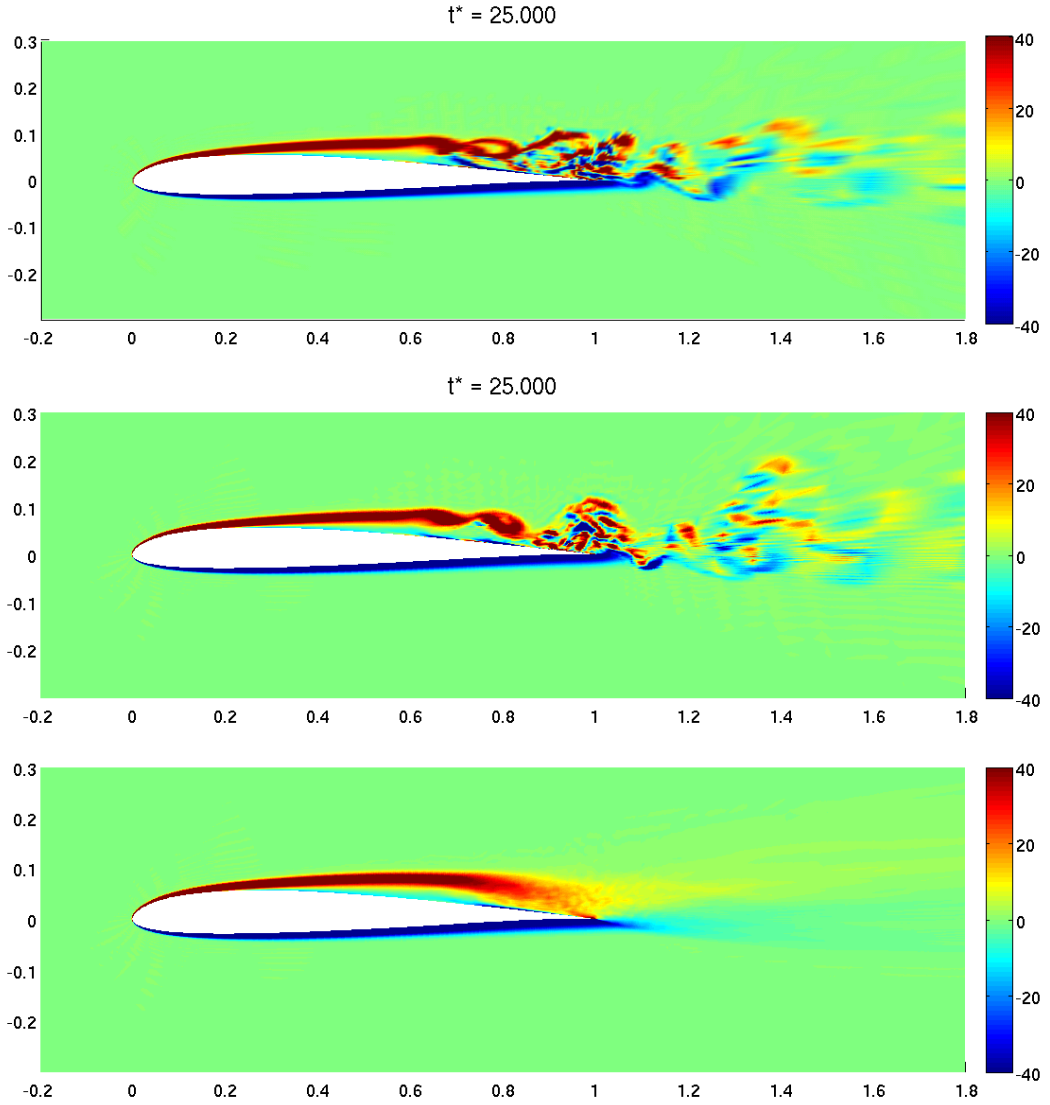

Figure 4-16: Span-wise vorticity at $Re = 22,000$ with grid 3, $p = 4$: instantaneous on middle plane (top), instantaneous span-wise average (middle), and average (bottom) contours.

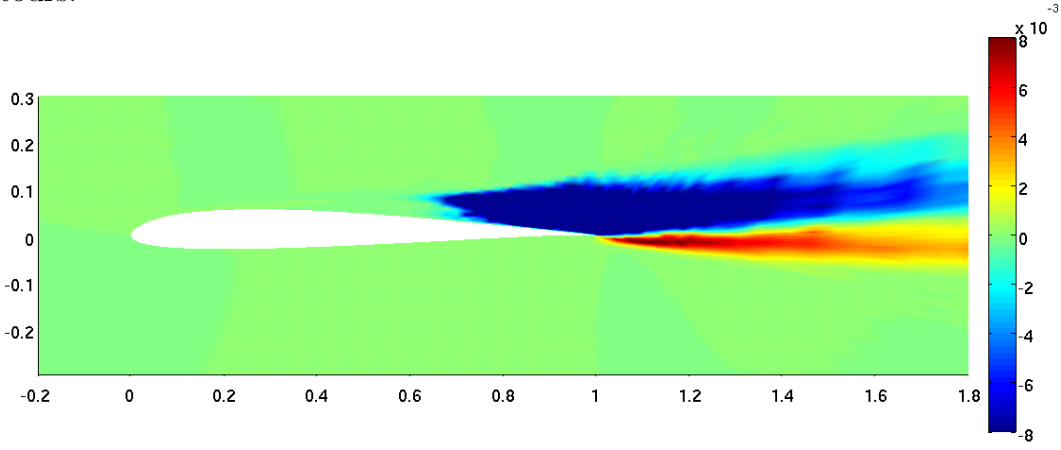

Figure 4-17: Non-dimensional chord-wise transverse velocity correlations $\overline{u'_x u'_z} \,/\, U_\infty^2$ at $Re = 22,000$ with grid 2, $p = 3$.

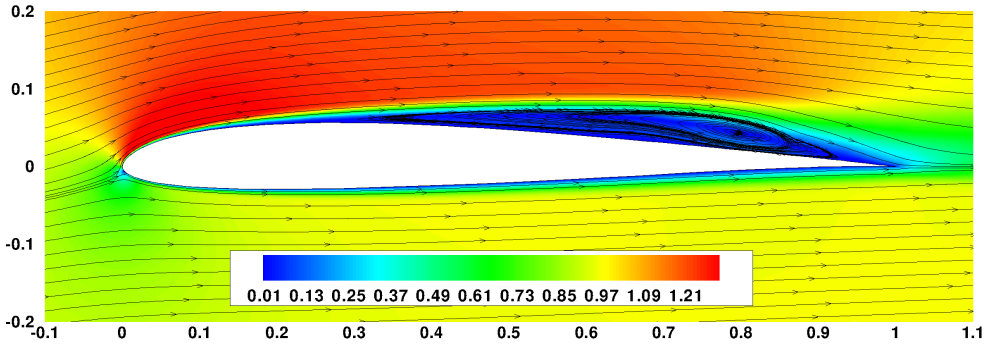

Figure 4-18: Average streamlines and contours of velocity magnitude at $Re = 22,000$ with grid 3, $p = 4$.

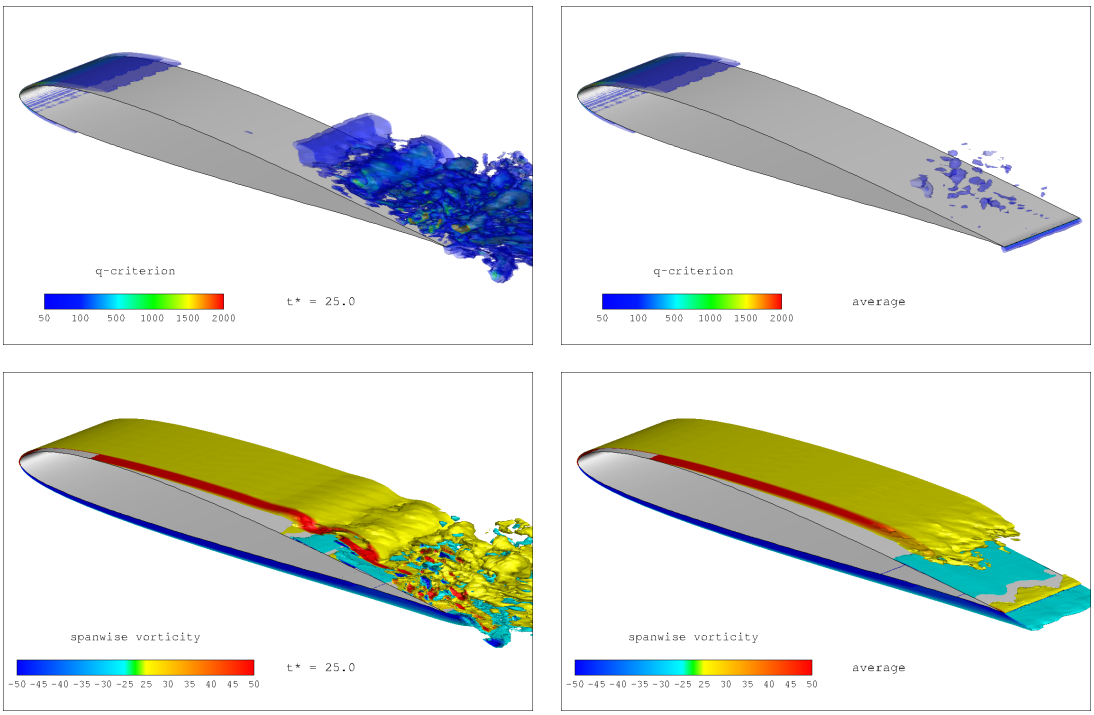

Figure 4-19: Instantaneous (left) and average (right) iso-surfaces of q-criterion (top) and span-wise vorticity (bottom) at $Re = 22,000$ with grid 3, $p = 4$.

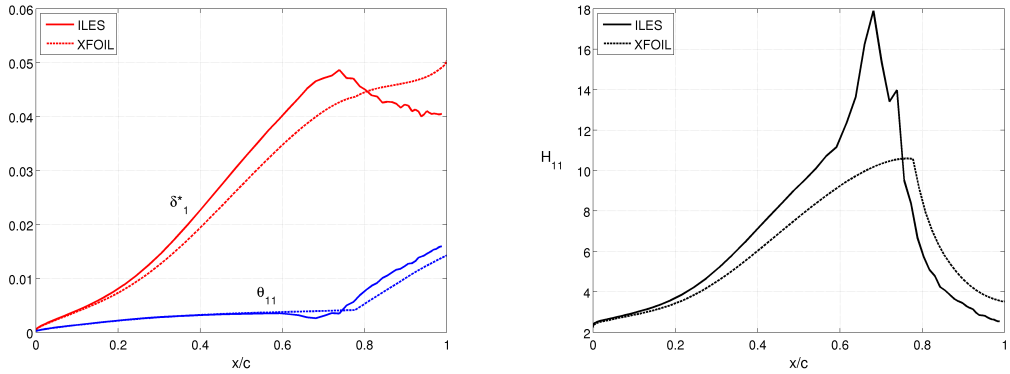

Figure 4-20: Boundary layer average streamwise displacement and momentum thicknesses (left), and shape factor (right) evolution along the chord-wise direction at $Re = 22,000$ with grid 2. The dashed lines give XFOIL predictions at 3.60° angle of attack, $N_{crit} = 7$.

4.2.4 Transition Mechanism

A close look at the boundary layer in the average flow provides insight into the transition process. From the shape factor of Figure 4-20, the transition location is clearly identified by the peak, while the separated flow can be identified as the region where H_{11} is larger than 4. The left plot of Figure 4-21 shows average profiles of streamwise pseudo-velocity at several chord-wise locations $x/c \in [0.1, 0.3]$, which resemble the profiles over a flat plate by construction of the pseudo-velocity through equation (3.11).

As explained in Section 3.8, the transition mechanism can be determined by considering the profiles of fluctuating streamwise pseudo-velocity, $\overline{u_1'^2}/\overline{u}_e^2$, of Figure 4-21. Each profile's shape is consistent with a superposition of Tollmien-Schlichting (TS) waves whose amplitudes increase along the chord-wise direction. Note also that the maximum moves away from the wall as it is convected downstream. The amplitude increase is quantified through the streamwise amplification factor N_1 of Figure 4-22 which increases linearly along the chord upstream of separation. This analysis clearly proves that transition is the result of the growth in TS waves, and hence that we are in the presence of a natural transition—not a bypass transition.

The chord-wise transition location determined previously from the shape factor ($x_{tr}/c = 0.68$) can be used to observe that, according to the $N_1(x/c)$ curve, transition takes place at a critical amplification of $N_1 = 4.6$. This is close to the value of 5.2 required for XFOIL at 3.60° angle of attack to give agreement with respect to the transition location.

Note that the fluctuations observed in N_1 for $x/c > 0.5$ indicate that the temporal

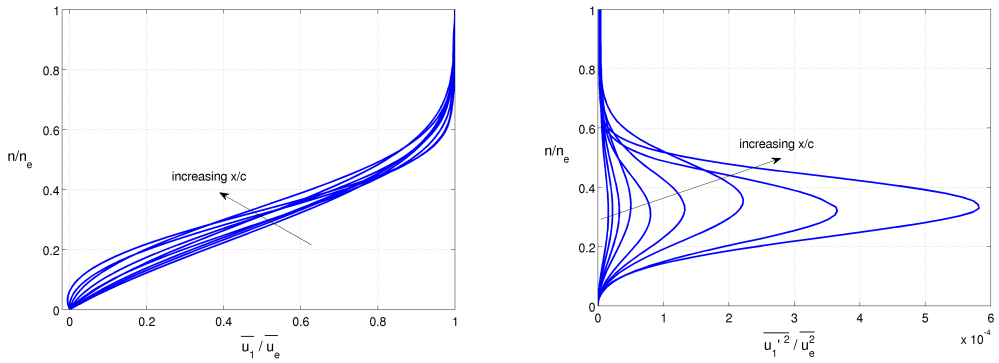

Figure 4-21: Boundary layer average profiles of streamwise pseudo-velocity $\overline{u}_1/\overline{u}_e$ (left), and fluctuating streamwise pseudo-velocity $\overline{u_1'^2}/\overline{u}_e^2$ (right), at different chordwise locations $x/c \in [0.1, 0.3]$ at $Re = 22,000$ with grid 2.

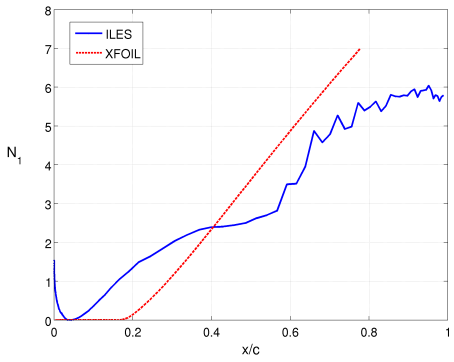

Figure 4-22: Amplification factor N_1 of streamwise pseudo-velocity perturbations for the flow at $Re = 22,000$ with grid 2. The dashed line gives XFOIL predictions at 3.60° angle of attack, $N_{crit} = 7$.

average needs to be carried out over a larger number of time steps to average the high-frequency structures present past transition. This lack of statistical convergence is mostly evident for boundary layer considerations and hence only observed in Figures 4-20 and 4-22, and also in the small variations seen in the average q-criterion iso-surfaces of Figure 4-19. However, the average process of disturbance growth and transition is well captured and described with these statistics.

4.3 High Transitional Regime: $Re = 60,000$

As mentioned in the background section, the flow around the SD7003 at 4° angle of attack and Reynolds number of 60,000 has been studied by several groups. This case is considered in detail here, in particular the three-dimensional effects, the required

resolution for ILES with DG, and the influence of span length and of time step on the average results. The transition mechanism is also established.

4.3.1 Three-Dimensionality

As expected, at $Re = 60,000$ the flow cannot be approximated by a two-dimensional simulation. The magnitude of force fluctuations in Figure 4-23 from a two-dimensional simulation are about a factor of 9 times larger than the three-dimensional results: three-dimensional alleviation is even more significant than at $Re = 22,000$. Furthermore, while at a Reynolds number of 22,000 a two-dimensional simulation was able to capture the separation bubble, at $Re = 60,000$ no bubble is present in two-dimensional runs as made evident in the pressure and skin friction profiles of Figure 4-24: there is no plateau in average C_p but only a close to linear pressure rise along most of the upper surface.

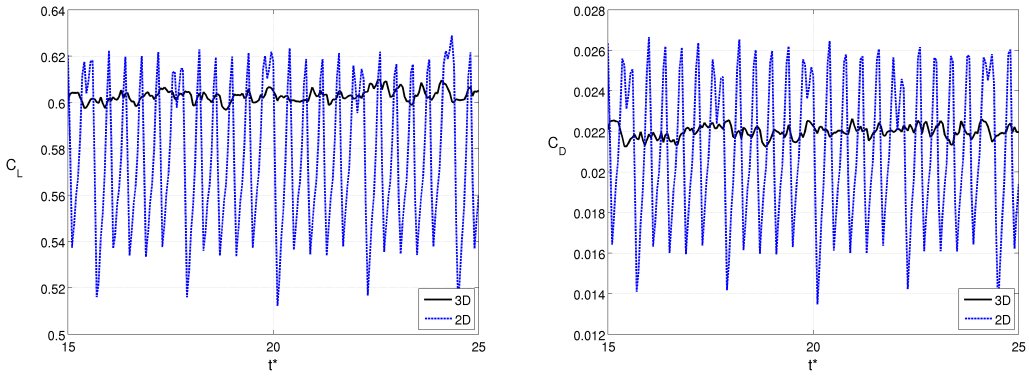

Figure 4-23: Time variation of lift (left) and drag (right) coefficients at $Re = 60,000$ on grid 2: comparison of 2D and 3D simulations.

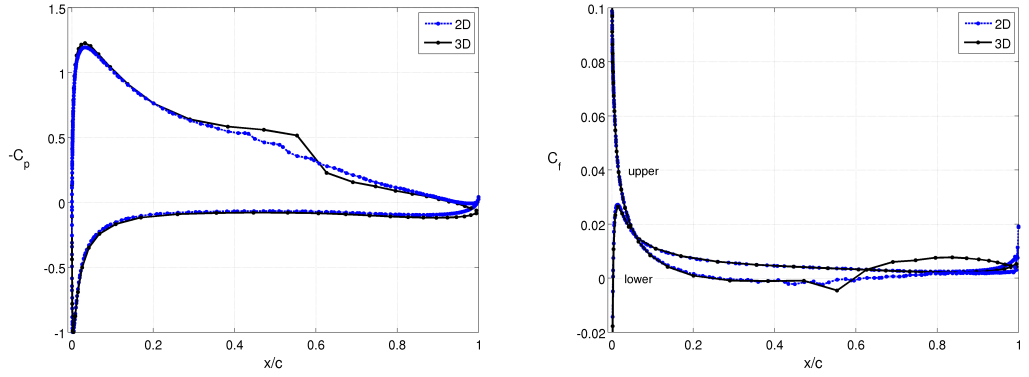

Figure 4-24: Average pressure coefficient (left) and chord-wise skin friction coefficient (right) at $Re = 60,000$ on grid 2: comparison of 2D and 3D simulations.

Table 4.3: Average flow results at Reynolds 60,000.

Source	Separation x_{sep}/c	Transition x_{tr}/c	Reattachment x_r/c	Bubble Length	C_L	C_D
grid 1	0.2907	0.4119	0.5396	0.2489c	0.5997	0.02058
difference with grid 2	19%	−20%	−9.6%	29%	0.51%	−6.4%
grid 2, 2D	0.2589	0.4295	0.6213	0.3624c	0.5730	0.02097
difference with grid 2	6.1%	−16.5%	4.1%	2.7%	−4.9%	−4.6%
grid 2	0.2440	0.5145	0.5967	0.3527c	0.6028	0.02198
difference with grid 2, $p = 4$	18%	−3.6%	−10%	−23%	−1.5%	−8.7%
grid 2, span 0.3c	0.2306	0.5146	0.6233	0.3927c	0.6021	0.02196
difference with grid 2	−5.5%	0.019%	4.5%	11%	−0.12%	−0.091%
grid 2, Δt_1^*	0.2424	0.5146	0.6124	0.3700c	0.6033	0.02200
difference with grid 2	−0.66%	0.019%	2.6%	4.9%	0.083%	0.091%
grid 2, $p = 4$, 2D	0.2544	0.4930	0.5811	0.3267c	0.5458	0.02142
difference with grid 2, $p = 4$	23%	−7.6%	−13%	−29%	−11%	−11%
grid 2, $p = 4$	0.2069	0.5335	0.6658	0.4589c	0.6122	0.02407
difference with grid 3, $p = 4$	−0.34%	−1.1%	−0.48%	−0.54%	0.39%	0.042%
grid 3, $p = 4$	0.2076	0.5397	0.6690	0.4614c	0.6098	0.02406

4.3.2 Spatial Resolution: Grid Comparisons

The spatial resolution required to capture the main flow features is assessed by comparing the results with several grids. We use grids 1 and 2 with polynomials of order 3 ($p = 3$), as well as grids 2 and 3 with $p = 4$. The distance between the wall and the first high-order node along the upper surface of the foil on grid 2, $p = 3$, is approximately $\Delta y \approx 4 \times 10^{-4}\, c$. At $x/c = 0.1$ where $C_f \approx 0.01$, this corresponds to approximately $\Delta y^+ \approx 2$ wall units, with the usual definition $y^+ = u_\tau y/\nu$ for $u_\tau = \sqrt{\tau_w/\rho} = \sqrt{C_f/2}\; U_\infty$.

The comparison of force histories and of average pressure and skin friction coefficients on the airfoil obtained with the different spatial resolution levels can be seen in Figures 4-25 and 4-26. Grid 1 is unable to properly capture the separation bubble and associated transition to turbulence, giving only a short LSB and forces that are too small. With $p = 3$, grid 2 provides a relatively accurate average flow but forces which are still too low, a delayed separation and too rapid transition thus resulting again in an under-predicted bubble length. Finally, the magnitude of the temporal evolution of forces, the average flow and boundary layer integral thicknesses obtained on grid 2 with $p = 4$ and on grid 3 with $p = 4$ agree. Thus, grid 2 is able to provide the required spatial resolution when polynomials of order $p = 4$ are employed.

4.3.3 Effect of Domain Span Length

In order to investigate what domain span length is required to simulate an infinite wing with a span-wise periodic boundary condition while properly capturing the

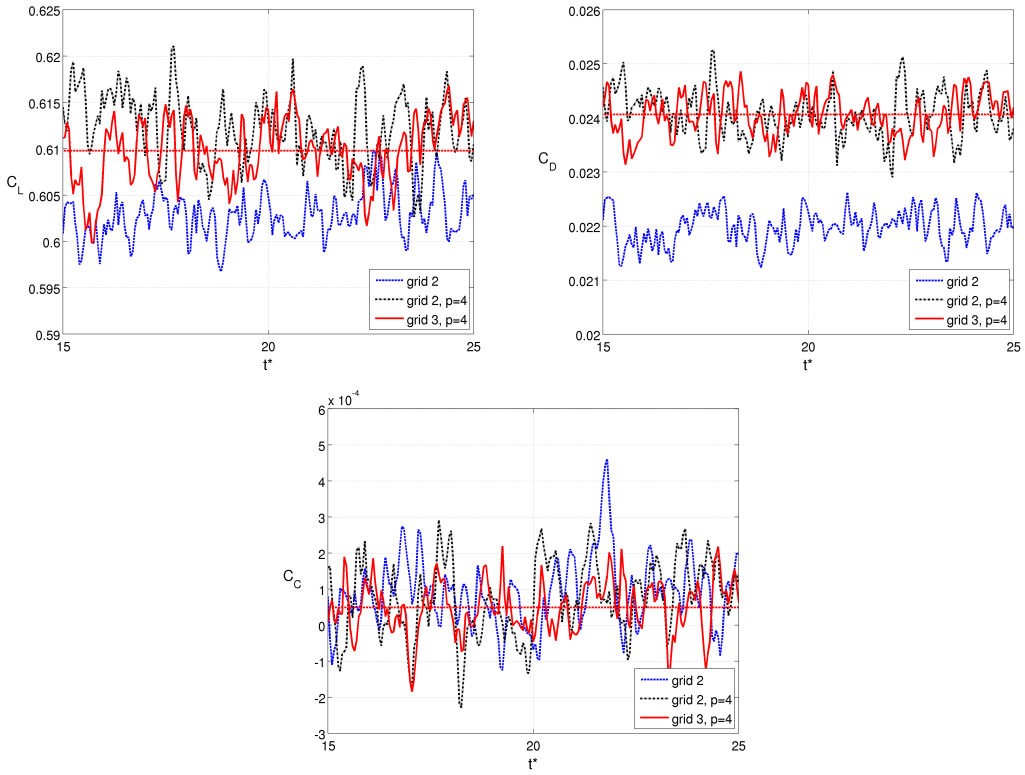

Figure 4-25: Time variation of lift (top left), drag (top right), and span-wise (bottom) force coefficients at $Re = 60,000$: comparison of results with different spatial resolutions. The dotted horizontal line indicates the average values for grid 3, $p = 4$.

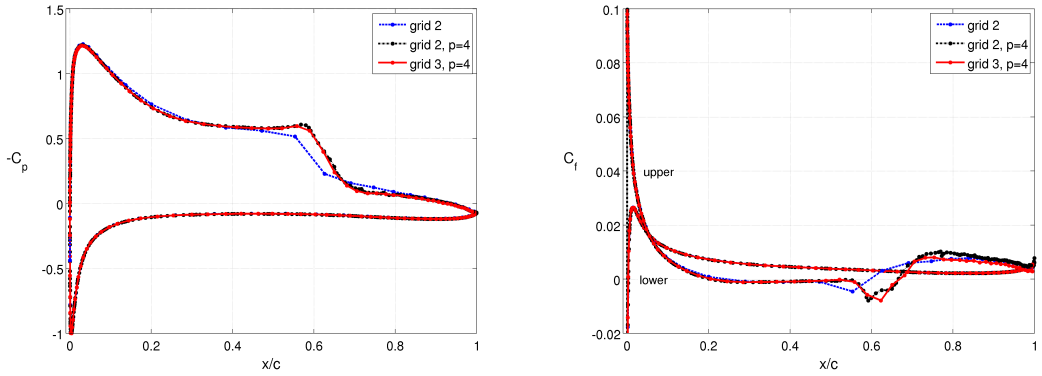

Figure 4-26: Average pressure coefficient (left) and chord-wise skin friction coefficient (right) at $Re = 60,000$: comparison of results with different spatial resolutions.

dominant flow structures, a domain with a span of 0.3 chords is considered in addition to the $0.2c$ span used in all other simulations, with a grid identical to grid 2, $p = 3$, except in the span-wise direction. To preserve the span-wise resolution, 3/2 times more nodes are used along the span: thus, this grid has 6 elements in the span-wise direction for 19 unique high-order nodes along the span, while grid 2 has 4 elements and 13 unique nodes span-wise. In this way, we ensure that comparing results with those on grid 2 reveals the effect of span length only, and ant differences are unrelated to resolution.

The time evolution of forces of Figure 4-27 show similar amplitudes and shapes for the two spans considered, even though the exact curves do not overlap, as expected for a turbulent flow and just as is observed when comparing different grids. Furthermore, the curves of average pressure coefficient and skin friction coefficient profiles of Figure 4-28 are undistinguishable between the two span lengths considered. However, small differences are observed in the boundary layer profiles as can be seen in Figure 4-29, but the separation, transition, and reattachment locations

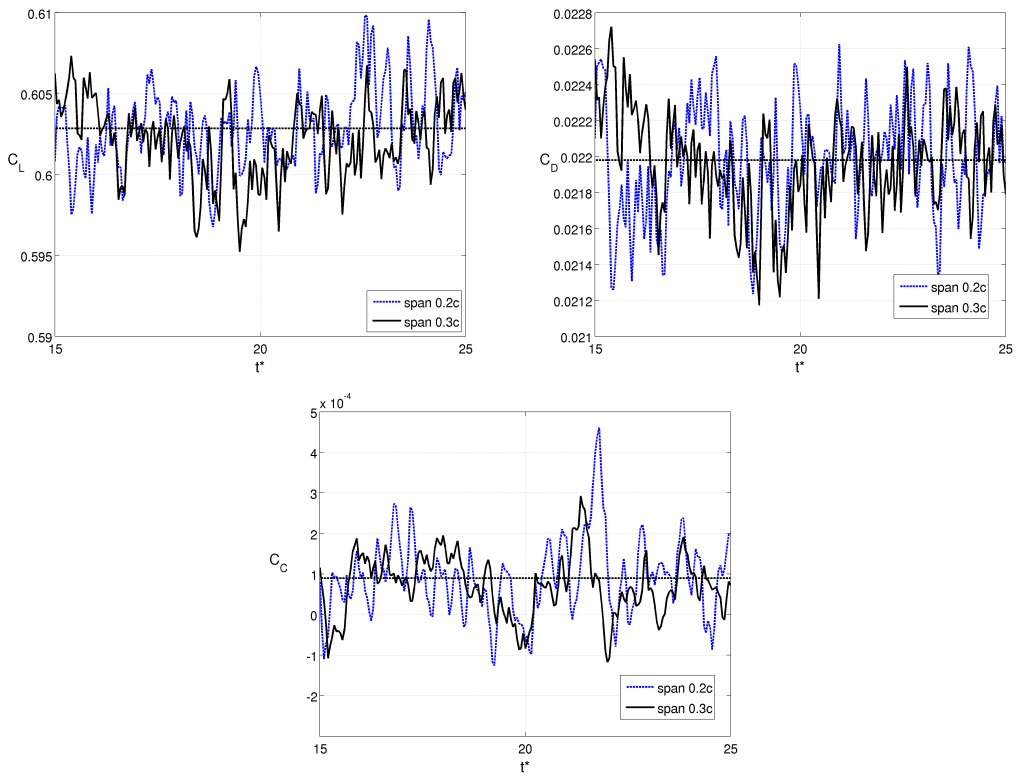

Figure 4-27: Time variation of lift (top left), drag (top right), and span-wise (bottom) force coefficients at $Re = 60,000$ on grid 2: comparison of grids with two different span lengths.The dotted horizontal line indicates the average values for the $0.3c$ span.

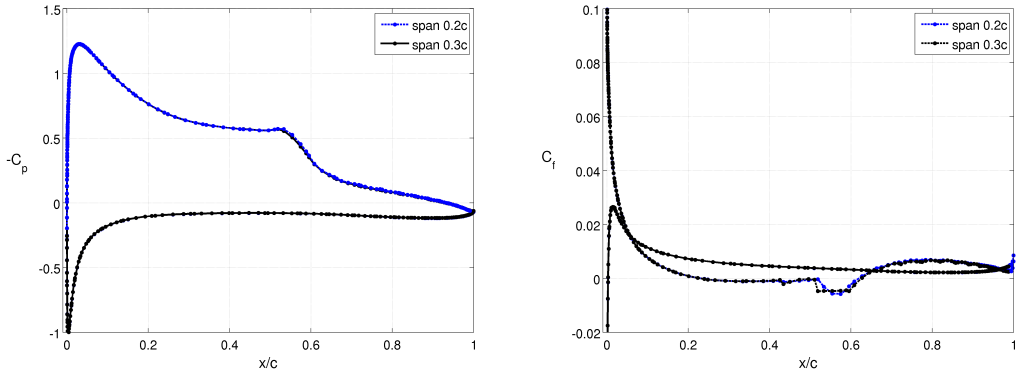

Figure 4-28: Average pressure coefficient (left) and chord-wise skin friction coefficient (right) at $Re = 60,000$ on grid 2: comparison of grids with two different span lengths.

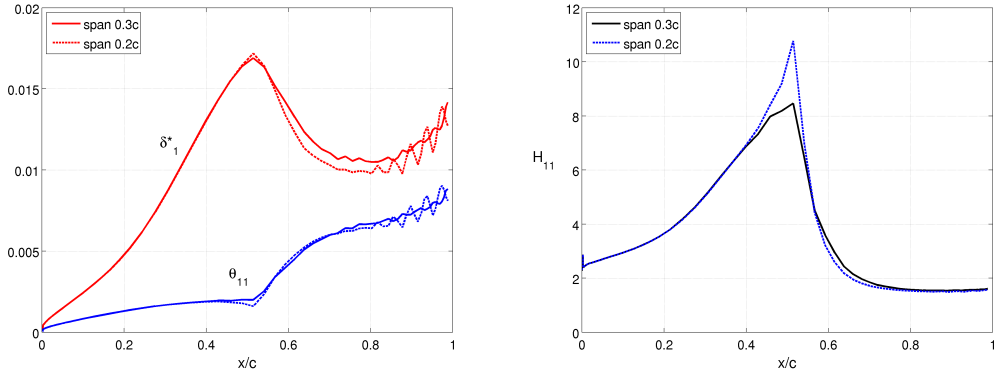

Figure 4-29: Boundary layer average streamwise displacement and momentum thicknesses (left), and shape factor (right) evolution along the chord-wise direction at $Re = 60,000$ with grid 2: comparison of grids with two different span lengths.

are essentially unchanged. A domain span of $0.2c$ is thus appropriate to capture the main flow features in the simulation of an infinite wing as observed by Galbraith and Visbal (2008).

4.3.4 Temporal Resolution

The use of an implicit time stepping procedure allows for the choice of large time steps irrespective of stability considerations. However, one should still ensure that the time resolution is sufficient to obtain accurate average quantities—even though the instantaneous fields depend on which frequencies are captured.

A simulation on grid 2 with solutions saved every $\Delta t_1^* = 0.02$ is performed in order to assess whether the chosen value of $\Delta t_0^* = 0.05$ can appropriately capture the mean flow features. Note that the actual time step in the DIRK time stepping method is

set to $dt^* = 0.01$ for both, but the solutions are saved either every 5 or every 2 steps for Δt_0^* and Δt_1^*, respectively. Note also that we have not chosen a multiple of the original time step Δt_0^* in order to avoid any possible sub-harmonic locking. When using the smaller time step Δt_1^*, statistics are computed over 500 steps (while 200 steps are used for Δt_0^*) in order to span the same time $t^* \in [15, 25]$; this also provides for a sense of the degree of convergence of the time-averaged fields and fluctuating quantities which are now determined based on more steps.

As expected, the average pressure and friction profiles are not sensitive to the temporal resolution change, and the curves of C_p and C_f of Figure 4-31 overlap. Furthermore, while the boundary layer thicknesses and shape factor evolution do not perfectly match between the runs at the two time steps, they are however very close. As can be seen in Figure 4-32, the shape factor curves are almost identical (maximum difference of 6.4% at transition), and the displacement and momentum thicknesses do exactly overlap before transition with a maximum difference in the

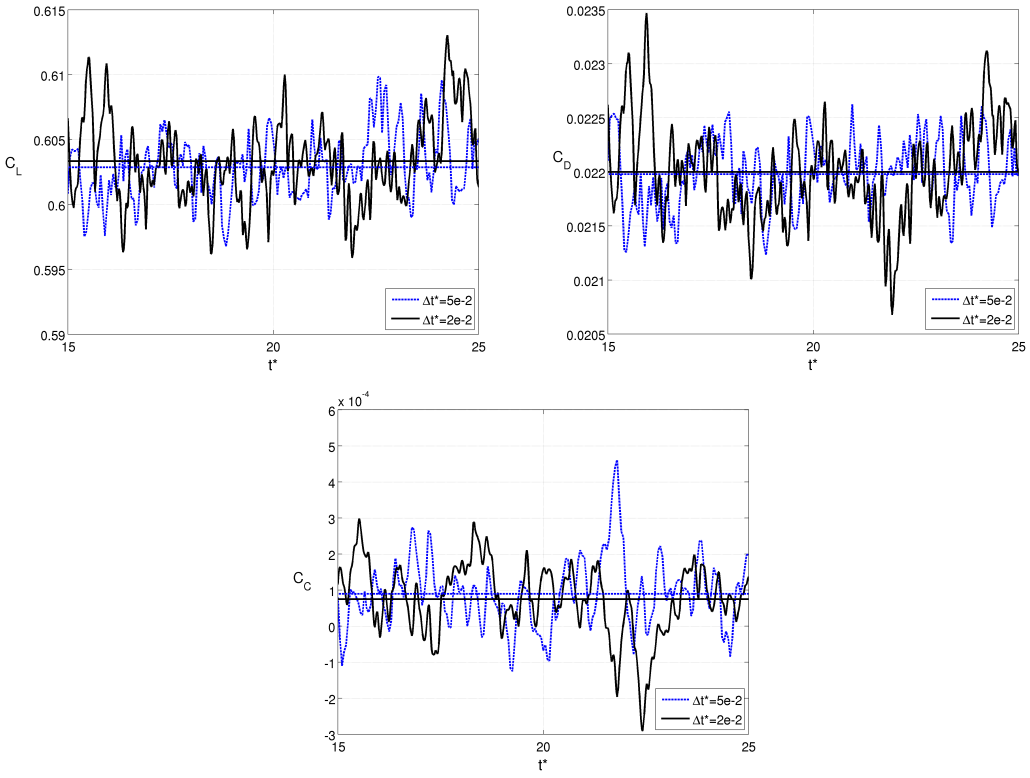

Figure 4-30: Time variation of lift (left), drag (center), and span-wise (right) force coefficients at $Re = 60,000$ on grid 2: comparison of simulations saved every 5 time steps ($\Delta t_0^* = 0.05$) and every 2 time steps ($\Delta t_1^* = 0.02$). The dotted horizontal line indicates the average values for the latter.

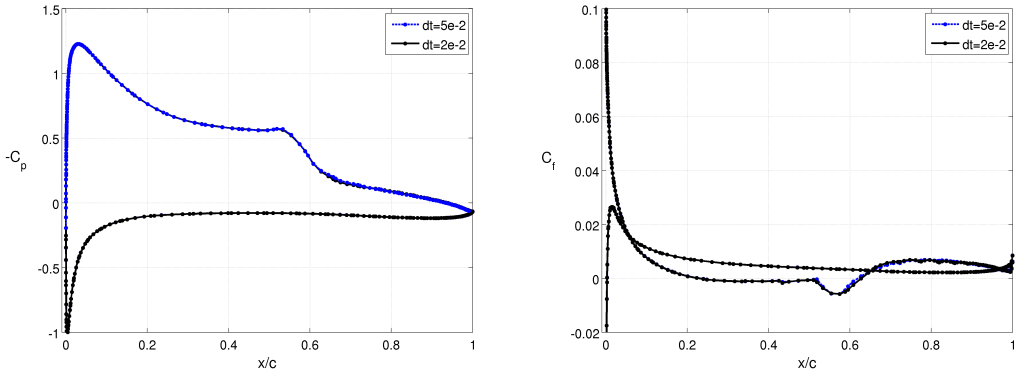

Figure 4-31: Average pressure coefficient (left) and chord-wise skin friction coefficient (right) at $Re = 60,000$ on grid 2: comparison of simulations saved every 5 time steps ($\Delta t_0^* = 0.05$) and every 2 time steps ($\Delta t_1^* = 0.02$).

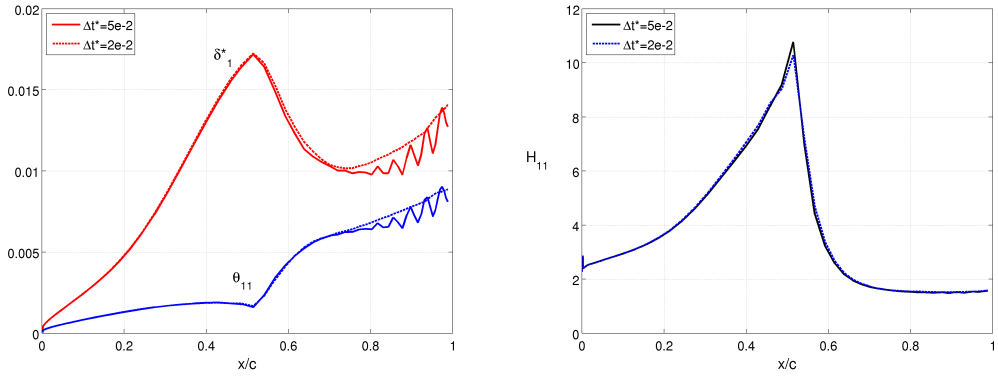

Figure 4-32: Boundary layer average streamwise displacement and momentum thicknesses (left), and shape factor (right) evolution along the chord-wise direction at $Re = 60,000$ with grid 2: comparison of simulations saved every 5 time steps ($\Delta t^* = 0.05$) and every 2 time steps ($\Delta t^* = 0.02$). The time averages are carried out over 200 and over 500 instantaneous solutions, respectively.

first three quarters of the foil of 3.7% and 4.9% for displacement and momentum, respectively. Separation, transition, and reattachment locations are unaffected. The oscillations observed on the aft quarter of the foil for the lower time step indicate a lack of statistical convergence of the averages computed over 200 steps, which is not present in the curve of the lower time step for which averages are computed over 500 steps instead. Thus, we deem the temporal resolution of $\Delta t_0^* = 0.05$ sufficient with respect to average statistics, even though the small (high-frequency) boundary layer structures would require more resolution to be fully accounted for.

4.3.5 Effect of Averaging

In order to verify that turbulence statistics are properly converged, we compare the results obtained by performing averages over 100 time steps (instantaneous solutions) and over 200 steps. The average pressure and skin friction coefficients over the wing shown in Figure 4-33 are undistinguishable, while there is a small difference in the boundary layer thicknesses and shape factor of Figure 4-34 which is comparable to that observed in Figure 4-32 when considering different temporal resolutions.

As mentioned in the methodology section, the average quantities are obtained by computing a time average followed by a spatial span-wise average. For the latter, the solution is first interpolated (to an order compatible with the polynomial order being used so as to avoid interpolation errors) at 20 different planes perpendicular to the span-wise direction, and these 20 interpolated solutions are then averaged. The use of only 10 planes was tested and again provided results that compared with the use of 20 planes in a manner similar to how the use of 100 steps compares with 200, as can be seen in Figures 4-35 and 4-36.

Thus, in order to obtain proper averages, the use of 200 solutions and 20 span-wise planes is deemed sufficient, in spite of the small fluctuations observed in the average boundary layer integral lengths after transition. Only for the amplification factor chord-wise evolution these statistics are inadequate, but still allowed us to observe the development of TS waves as discussed in Section 4.3.7.

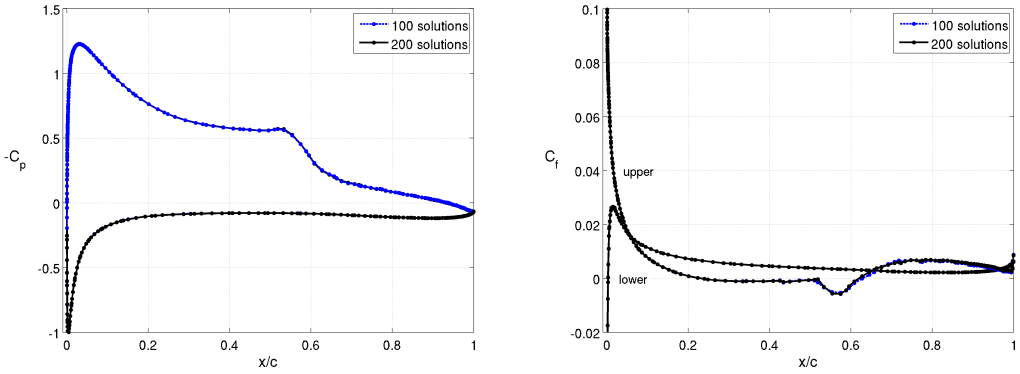

Figure 4-33: Average pressure coefficient (left) and chord-wise skin friction coefficient (right) at $Re = 60,000$ on grid 2: comparison of averages over 100 and over 200 solutions.

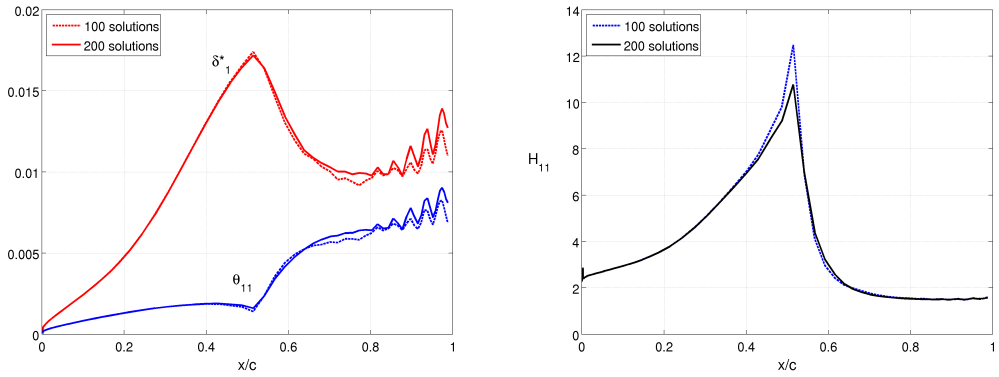

Figure 4-34: Boundary layer average streamwise displacement and momentum thicknesses (left), and shape factor (right) evolution along the chord-wise direction at $Re = 60,000$ with grid 2: comparison of averages over 100 and over 200 solutions.

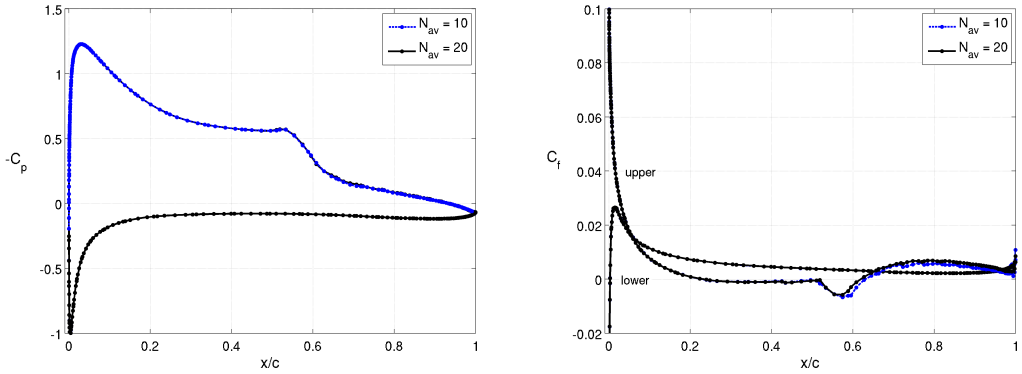

Figure 4-35: Average pressure coefficient (left) and chord-wise skin friction coefficient (right) at $Re = 60,000$ on grid 2: comparison of averages over 10 and over 20 span-wise planes.

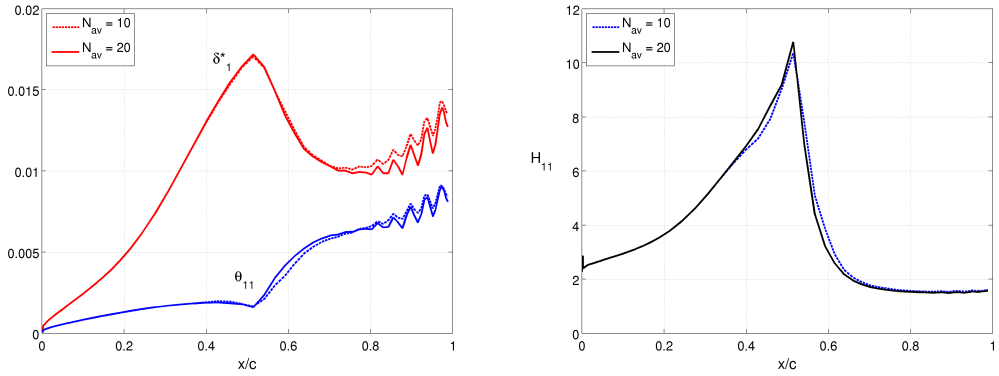

Figure 4-36: Boundary layer average streamwise displacement and momentum thicknesses (left), and shape factor (right) evolution along the chord-wise direction at $Re = 60,000$ with grid 2: comparison of averages over 10 and over 20 span-wise planes.

4.3.6 Results with Grid 2, $p = 4$

Table 4.4 gives a comparison with previously published results at a Reynolds number of 60,000, as well the mean lift and drag coefficients for the present simulations with grid 2, $p = 4$. TU-BS corresponds to the PIV experiments at the Technical University of Braunschweig Low-Noise Wind Tunnel (Radespiel et al., 2006), while HFWT is from the PIV experiments at the Air Force Research Laboratory Horizontal Free-Surface Water Tunnel (Ol et al., 2005); Visbal's data is from an ILES with sixth-order compact differences by Galbraith and Visbal (2008); Visbal et al. (2009). The present results are well within variations between previously published works.

At $Re = 60,000$, with a fifth-order method, a relatively coarse mesh (grid 2, $p = 4$) with 1.8 million high-order nodes is able to accurately capture the average locations of separation, transition, and reattachment, as well as the average pressure and skin friction coefficient profiles along the foil which can be seen in Figure 4-37 together with comparison curves for the data from XFOIL (Drela, 2002) and by Galbraith and Visbal (2008); Visbal et al. (2009) who employ a well resolved grid with about 4.8 million nodes. The separation bubble is clearly visible in these profiles, with separation occurring on average at 21% of the chord and reattachment at 67% in the present simulations. As expected, the length of the LSB is significantly shorter ($0.46c$ compared to $0.72c$) than at $Re = 22,000$ due to a more rapid transition.

Contours of instantaneous and average span-wise vorticity are shown in Figure 4-39, and reveal a large number of small structures created by turbulent motions past the mid-chord. Average non-dimensional velocity correlations can be seen in Figure 4-40 and illustrate the presence of transition to turbulence. This is verified by looking at the displacement thickness, momentum thickness, and shape factor of the pseudo-

Table 4.4: Comparison of average results at $Re = 60,000$ with grid 2, $p = 4$. TU-BS (Radespiel et al., 2006) and HFWT (Ol et al., 2005) correspond to PIV experiments; Visbal (Galbraith and Visbal, 2008; Visbal et al., 2009) is an ILES; the XFOIL predictions are obtained at 3.37° and $N_{crit} = 7$.

Source	Separation x_{sep}/c	Transition x_{tr}/c	Reattachment x_r/c	Bubble Length	C_L	C_D
TU-BS	0.30	0.53	0.62	$0.32c$	-	-
HFWT	0.18	0.47	0.58	$0.40c$	-	-
Visbal	0.23	0.55	0.65	$0.42c$	-	-
XFOIL	0.28	0.58	0.61	$0.34c$	0.5624	0.0176
present ILES	0.21	0.53	0.67	$0.46c$	0.6122	0.0241

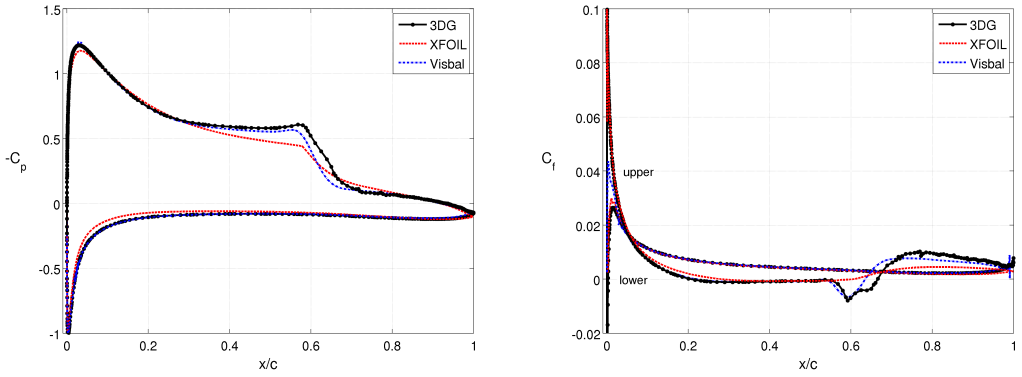

Figure 4-37: Average pressure coefficient (left) and streamwise skin friction coefficient (right) at $Re = 60,000$ on grid 2, $p = 4$. The dashed lines give XFOIL predictions at 3.37°, $N_{crit} = 7$, and the dot-dashed lines show ILES data of Galbraith and Visbal (2008); Visbal et al. (2009).

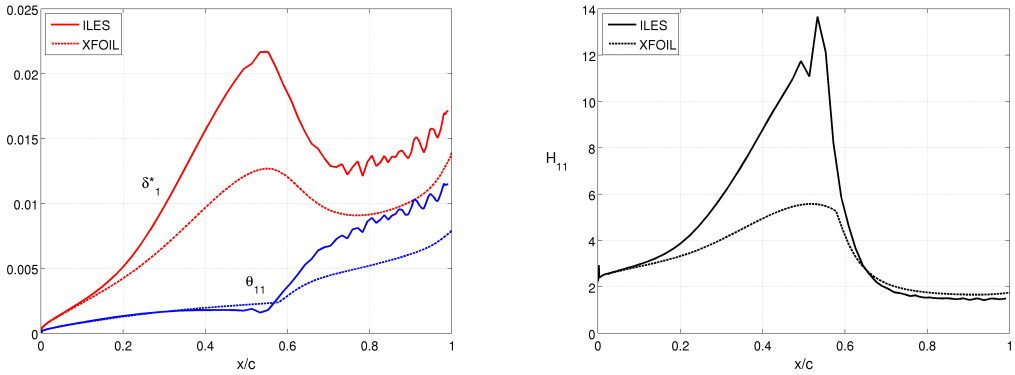

Figure 4-38: Boundary layer average streamwise displacement and momentum thicknesses (left), and shape factor (right) evolution along the chord-wise direction at $Re = 60,000$ with grid 2, $p = 4$. The dashed lines give XFOIL predictions at 3.37° angle of attack, $N_{crit} = 7$.

Table 4.5: Summary of average results at the three Reynolds numbers considered with: grid 1, $p = 3$ for $Re = 10,000$; grid 2, $p = 3$ for $Re = 22,000$; grid 2, $p = 4$ for $Re = 60,000$.

Reynolds Number	Separation x_{sep}/c	Transition x_{tr}/c	Reattachment x_r/c	Bubble Length	C_L	C_D
10,000	0.3557	0.9384	-	-	0.3743	0.04967
22,000	0.2386	0.6812	0.9379	$0.6993c$	0.6456	0.04272
60,000	0.2069	0.5335	0.6658	$0.4589c$	0.6122	0.02407

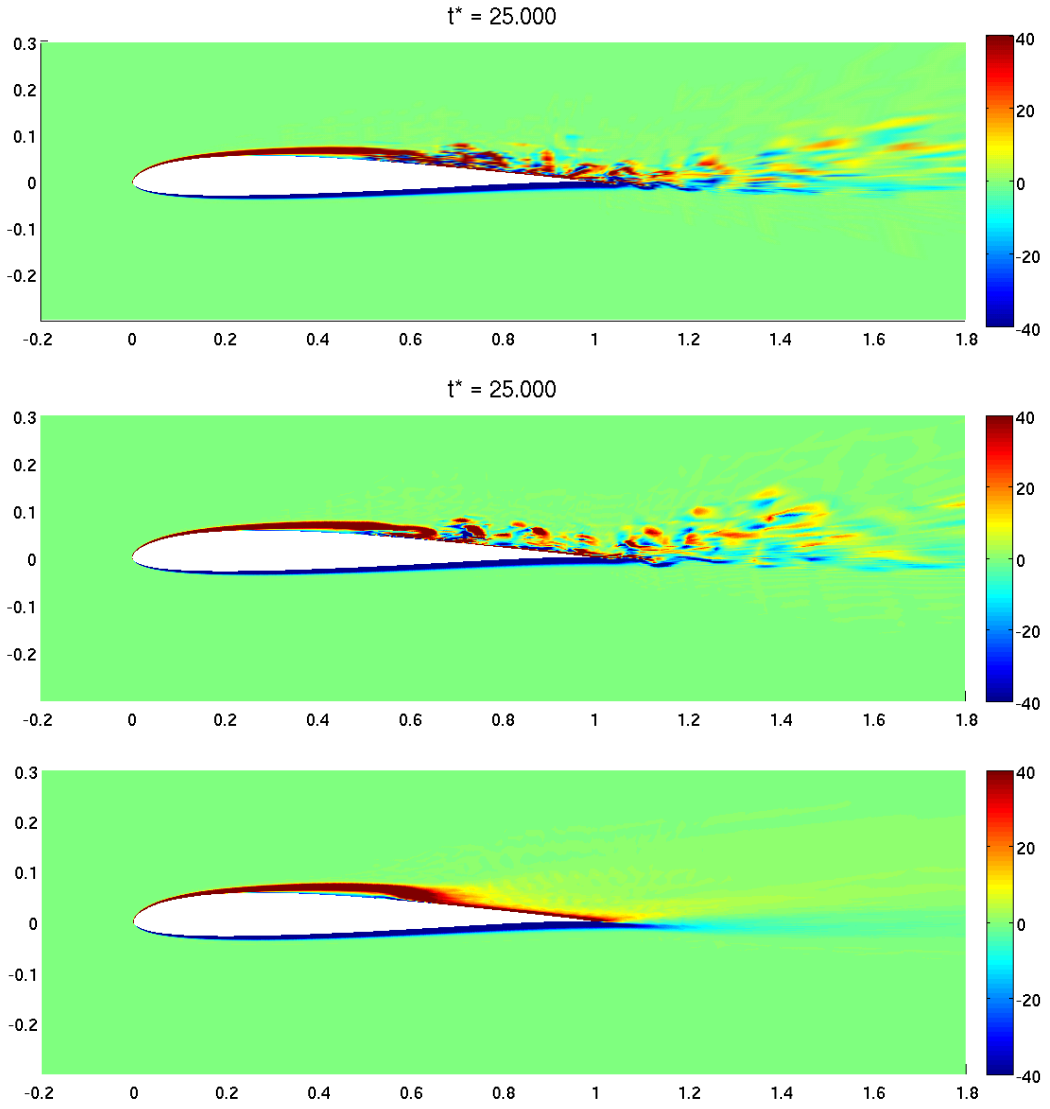

Figure 4-39: Span-wise vorticity at $Re = 60,000$ with grid 2, $p = 4$: instantaneous on middle plane (top), instantaneous span-wise average (middle), and average (bottom) contours.

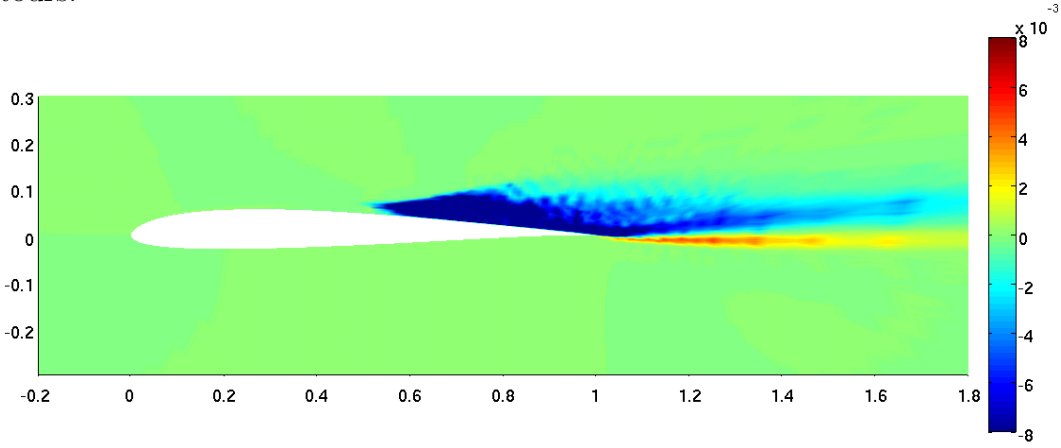

Figure 4-40: Non-dimensional chord-wise transverse velocity correlations $\overline{u'_x u'_z} \,/\, U_\infty^2$ at $Re = 60,000$ with grid 2, $p = 4$.

velocity profile (Figure 4-38). A sharp peak in shape factor reveals that transition to turbulence occurs on average at 53% of the chord.

As shown earlier, three-dimensional structures are present at this Reynolds number due to turbulent motions; this is clearly visible in the instantaneous iso-surfaces of q-criterion and span-wise vorticity of Figure 4-42. On the other hand, the average surfaces are almost cylindrical showing that the average flow is close to converged.

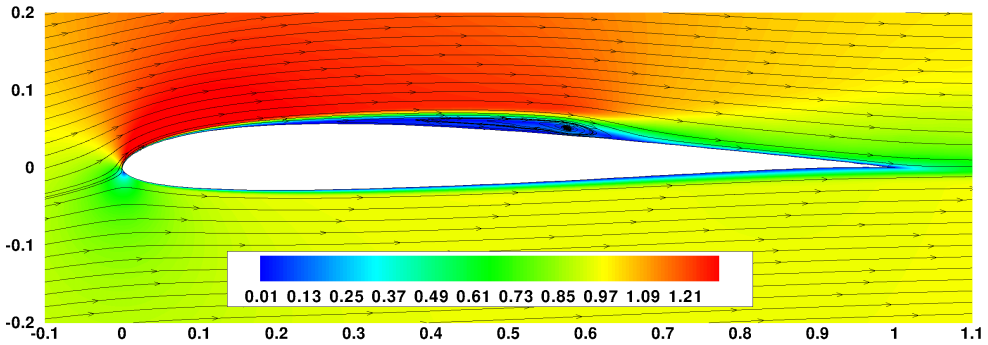

Figure 4-41: Average streamlines and contours of velocity magnitude at $Re = 60,000$ with grid 2, $p = 4$.

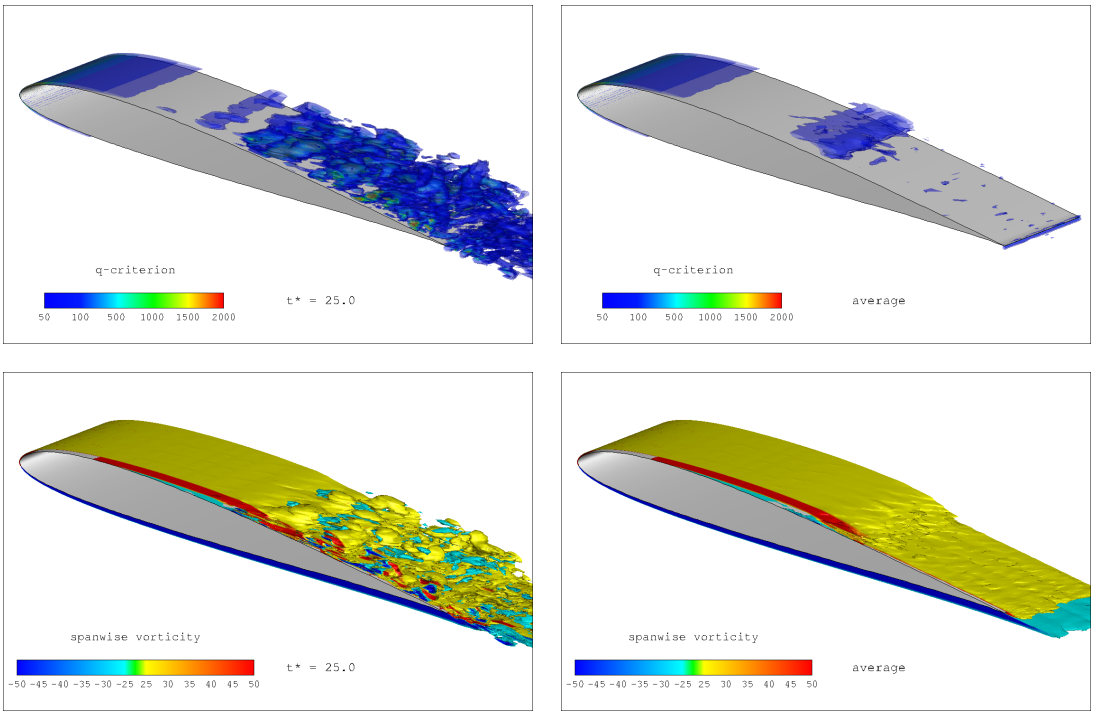

Figure 4-42: Instantaneous (left) and average (right) iso-surfaces of q-criterion (top) and span-wise vorticity (bottom) at $Re = 60,000$ with grid 2, $p = 4$.

4.3.7 Transition Mechanism

Profiles of fluctuating streamwise pseudo-velocity, $\overline{u_1'^2}/\overline{u}_e^2$, can be seen on the left plot of Figure 4-43, for chord-wise stations $x/c \in [0.1, 0.3]$. As for the $Re = 22,000$ flow, the profiles are consistent with a superposition of Tollmien-Schlichting (TS) modes, and we observe an increase in perturbation amplitude along the chord-wise direction. The average streamwise pseudo-velocity profiles resemble those at $Re = 22,000$ of Figure 4-21.

The growth of the streamwise amplification factor along the chord-wise direction can be seen in Figure 4-44. As mentioned previously, the fluctuations observed from the separation location on ($x/c \geq 0.24$) indicate that the temporal averages need to be carried out over a longer period of time. The dotted red line shows the amplification factor of the single most energetic wave as predicted by XFOIL, while the blue line for the present simulation is the result of the integration (3.18) and hence corresponds to the compounded energy of all the waves; this explains why the XFOIL line gives a smaller amplification factor at any given location. However, the slopes of the lines for both cases are very similar, which confirms that the unstable modes are properly captured even with the relatively coarse grid used.

Again, both the shape of the fluctuating streamwise pseudo-velocity profiles and the spatial linear growth of the amplification factor indicate that the mechanism of transition along the LSB for these low Reynolds number flows is a TS natural transition.

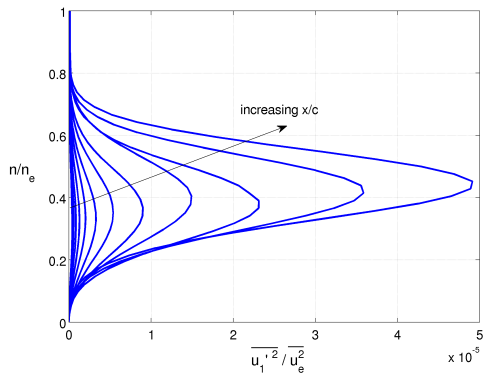

Figure 4-43: Boundary layer average fluctuating streamwise pseudo-velocity profiles $\overline{u_1'^2}/\overline{u}_e^2$ at different chord-wise locations $x/c \in [0.1, 0.3]$ at $Re = 60,000$ with grid 2, $p = 4$.

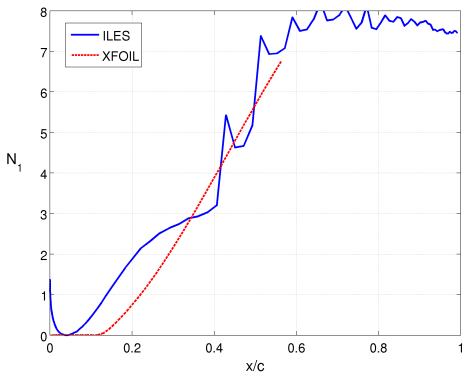

Figure 4-44: Amplification factor N_1 of streamwise pseudo-velocity perturbations for the flow at $Re = 60,000$ with grid 2, $p = 4$.

Table 4.6: Disturbance amplification based on transition model for the three Reynolds numbers considered. The columns 'positive source' and 'positive N' give the location where the value (source or N) becomes larger than 0.5% of its maximum; 'slope of N' gives the slope of the linear growth region.

Reynolds Number	Transition x_{tr}/c	Positive Source	Positive N	N at Transition	Slope of N
10,000	0.9384	0.2773	0.3059	4.4	7.2
22,000	0.6812	0.1631	0.1798	6.8	13.8
60,000	0.5335	0.1126	0.1339	9.4	25.9

4.4 Use of the Transition Model Equation

Having determined that transition to turbulence along the LSB is due to the growth of TS waves, we compute the evolution of the amplification factor N using the transition model equation (3.22) to verify that it predicts the development of instability correctly.

The details of how the transition model is to be used with any computational approach is described in Section 3.9. In the present work, the model equation is discretized using the same DG procedure as the governing equations (see Section 3.2) which provides a stable discretization of convection, and hence no diffusion term is required. Furthermore, for the cases of a stationary wing, we are interested in the average flow. Therefore, we solve the steady state equation

$$\nabla_s \cdot (\vec{u}_c\, N) = \frac{|\vec{u}_c|}{\theta_{11}} f\left(H_{11}, Re_\theta\right) , \tag{4.1}$$

in which the required inputs are computed as part of the boundary layer post-processing from the average flow, and (3.24) defines the surface gradient operator $\nabla_s \equiv \hat{s}_1\, \partial/\partial s_1 + \hat{s}_2\, \partial/\partial s_2$. Note that the convective velocity is taken to be $\vec{u}_c = k_c\, \vec{u}_e$ and that the choice of k_c has no influence on the final (steady) evolution of N predicted by (4.1). For each Reynolds number, the flow at the level of spatial refinement that was shown to be required is used in this section: grid 1, $p = 3$ for $Re = 10,000$; grid 2, $p = 3$ for $Re = 22,000$; and grid 2, $p = 4$ for $Re = 60,000$.

The edge location for the boundary layer on the upper surface can be seen in Figure 4-45 for the three Reynolds numbers considered; the strong variations on the back of the foil show that averages still contain some fluctuations due to the presence of small, high-frequency structures which require many time steps to compute their

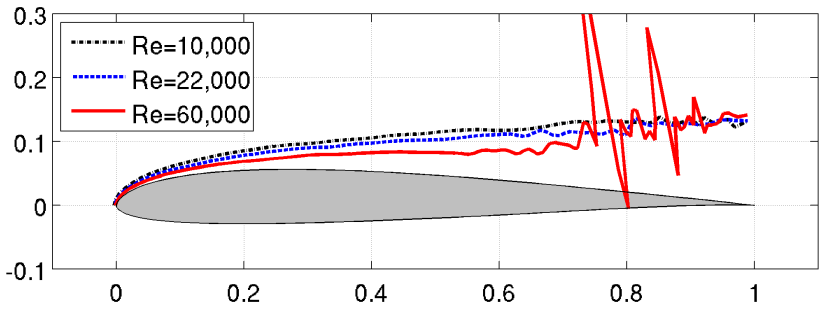

Figure 4-45: Location of the boundary layer edge for the three Reynolds numbers considered.

mean behavior—this being specially true at higher Reynolds numbers. Figure 4-46 shows the chord-wise evolution of edge velocity and source term (right-hand-side of (4.1)), where again some fluctuations are still present on the back of the foil.

The growth of the N-factor obtained from the transition model equation (4.1) is shown in Figure 4-47. For comparison, Figure 4-48 shows the amplification factors obtained by integrating the streamwise pseudo-velocity perturbations through equation (3.18) for the three Reynolds numbers studied, together with XFOIL predictions (straight dotted lines), as had been plotted in Figures 4-22 and 4-44.

As required, when the Reynolds number increases the disturbances are amplified earlier (N starts increasing farther upstream) and faster (larger slope). Based on the boundary layer post-processing, transition takes place at $x_{tr}/c = 0.6812$ for $Re = 22,000$, and this location corresponds to $N = 6.8$ in the curve of Figure 4-47, while at $Re = 60,000$ transition is observed at $x_{tr}/c = 0.5335$ where $N = 9.4$, as indicated in Table 4.6.

Based on the location where the source term stops being zero, disturbances are amplified (positive source) starting at $x/c = 0.1631$ and at $x/c = 0.1126$ for $Re = 22,000$ and $Re = 60,000$ respectively, while the N factor starts increasing at $x/c = 0.1798$ and at $x/c = 0.1339$, respectively for these two flows. The location where either the source, or N, becomes positive has been taken to be where its value is larger than 0.5% of its maximum.

The evolution of the N-factor predicted by the transition model equation has the proper shape: as the Reynolds number is increased, the linear growth factor increases; moreover, it reflects how the disturbances start growing exponentially at a chord-wise location that gets closer and closer to the leading edge as Re is increased. However, there is no common value of N for the different Reynolds numbers at which transition

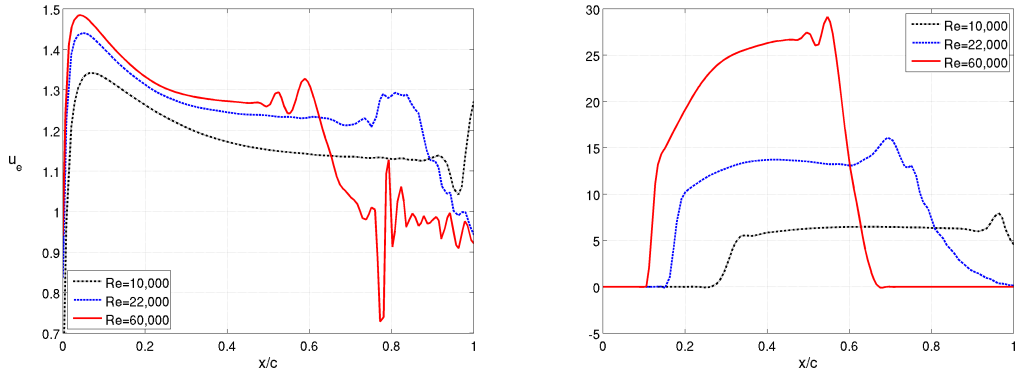

Figure 4-46: Chord-wise evolution of boundary layer edge velocity (left) and source term $|\vec{u}_c| f\left(H_{11}, Re_\theta\right)/\theta_{11}$ with $k_c = 0.8$ (right) for the three Reynolds numbers considered.

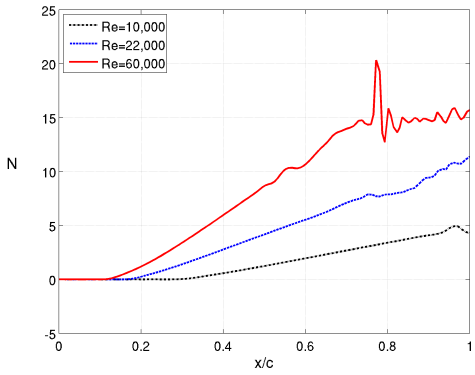

Figure 4-47: Evolution of N-factor based on steady transition model equation for the three Reynolds numbers considered.

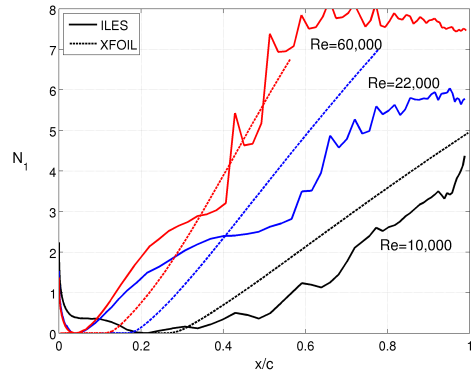

Figure 4-48: Evolution of streamwise amplification factor N_1 based on integration of pseudo-velocity perturbations for the three Reynolds numbers considered; the dashed straight lines give XFOIL's predictions.

can be set to take place, *i.e.* no critical amplification N_{crit} prevails. Furthermore, there does not seem to be any simple correlation linking the flow Reynolds number to the value of N at transition, nor to the linear slope of N, nor to the location of growth onset in the source term. The quantitive aspects of the transition prediction will be determined by the specific coupling of the transition model equation with a given RANS turbulence model. In particular, the N evolution is to be incorporated into either a trip term (with the SA model for instance) or a turbulence suppression term, the calibration of which needs to be investigated.

Note that the fluctuations in the N evolution (which result from fluctuations in u_e and the source term) are not expected to influence the transition location triggered by coupling the N transport equation with turbulence models, since what happens downstream of the location where N reaches the critical value for transition has an insignificant impact. It is trivial to implement a low pass filter to obtain smoother evolutions of the source term and hence of N even from an only partially-averaged flow.

The plots in Figure 4-49 show the results obtained when applying a low-pass-filter smoothing to the edge velocity and source term for the $Re = 60,000$ case. The smoothed evolution, $< a(x/c) >$, is computed by combining the original (unfiltered) variable, $a(x/c)$, with the filtered variable, $\tilde{a}(x/c)$, through

$$< a >= (1 - \kappa)\, a + \kappa\, \tilde{a}$$

using the ramping factor

$$\kappa = \frac{1 + \tanh\left(\frac{x - x_0}{d_w c}\right)}{2}\,.$$

The parameter d_w controls the width over which the damping occurs, while x_0/c defines the center of the ramp along the chord. Here, we set $d_w = 20$ and $x_0/c = 0.4$, and used a first-order Butterworth low-pass filter with normalized cut frequency of 0.1 to obtain $\tilde{a}$ and the plots of Figure 4-49.

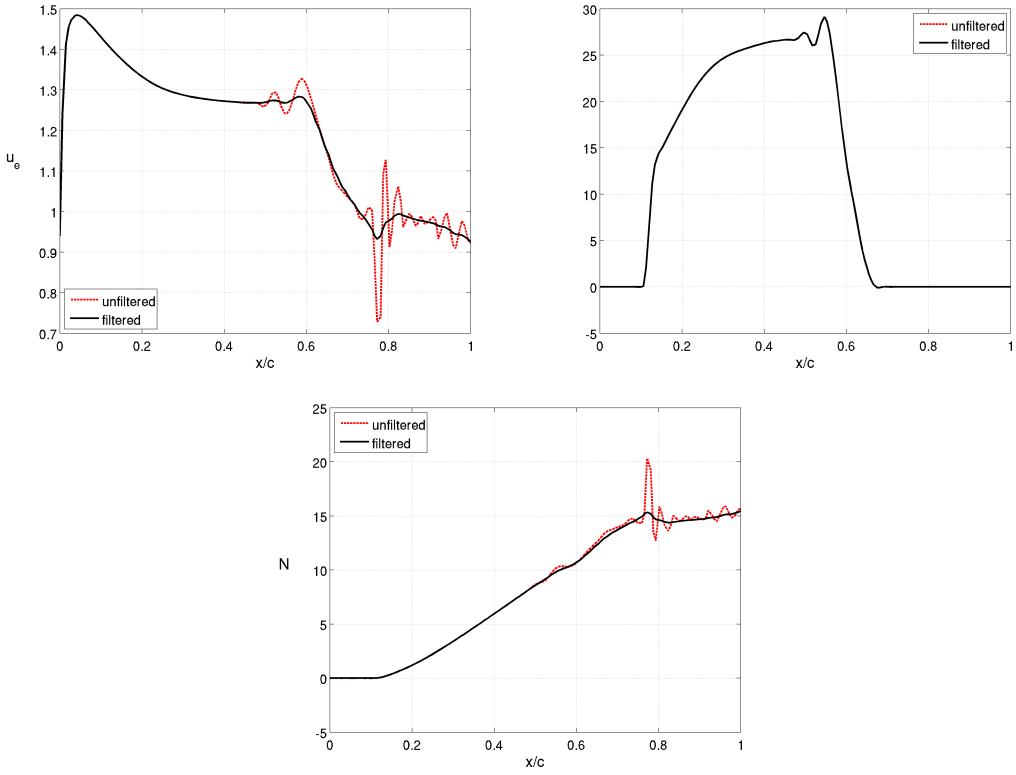

Figure 4-49: Chord-wise evolution of boundary layer edge velocity (top left), source term $|\vec{u}_c| f\left(H_{11}, Re_\theta\right)/\theta_{11}$ with $k_c = 0.8$ (top right), and N-factor (bottom) for $Re = 60,000$: comparison of results with and without filtering (smoothing) of edge velocity and source term.

Chapter 5

Effects of Cross-Flow on Transition

As described in the background Section 2.4, when a wing is swept with respect to the free-stream flow direction, a cross-flow velocity component appears within the boundary layer which can interact and destabilize the streamwise flow. In order for a transition model to be applicable to flows over swept wings, it would need to integrate this influence. To further contribute to the understanding of low Reynolds number aerodynamics, the present chapter investigates the effects of the boundary layer cross-flow on transition which have so far remained largely unexplored for the low Reynolds number regime.

5.1 Swept Infinite Wings

5.1.1 Approach

A rectangular, infinite, SD7003 wing is again used but this time the free-stream velocity has a non-zero component in the direction of the leading edge line. With x and y the chord-wise and span-wise directions respectively, the velocity imposed at the farfield of the domain is given by

$$\vec{U}_\infty = \begin{bmatrix} \cos\alpha \\ \tan\Lambda \\ \sin\alpha \end{bmatrix} \tag{5.1}$$

in which α is the angle of attack as previously, and Λ is the sweep angle which is defined here as the angle between the free-stream velocity and the x-z plane on which the SD7003 foil lies. Note that the angle of attack is the angle between the free-stream

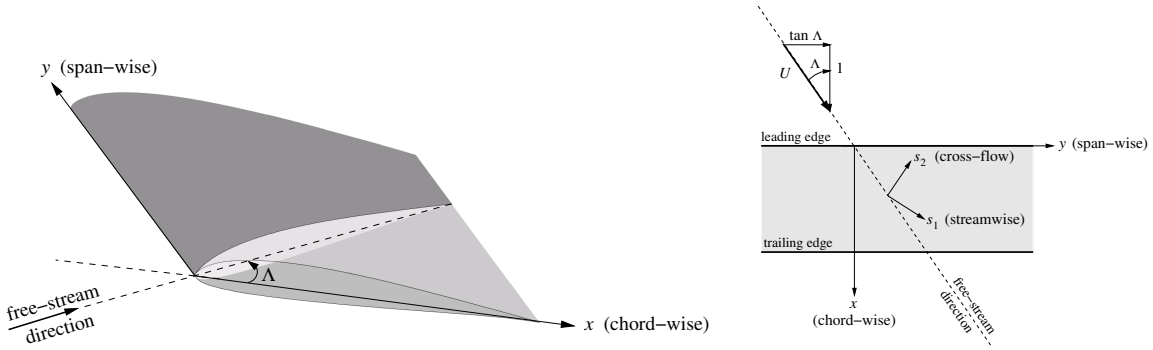

Figure 5-1: Illustration of the free-stream velocity $\vec{U}_\infty$, chord-wise direction x, and span-wise direction y for the swept-wing flow; Λ is the sweep angle.

velocity and the SD7003 chord (x-direction), that is $\alpha = \tan^{-1}(U_{\infty_z}/U_{\infty_x})$ as for the wing with no cross-flow. The free-stream velocity now has a magnitude of

$$U_\infty = \sqrt{1+\tan^2\Lambda} = \frac{1}{\cos\Lambda} \ .$$

In order to keep the descriptions consistent with those in the absence of cross-flow of Section 4, the term *chord-wise* is used to refer to the x-direction which preserves the SD7003 geometry, while the foil that the free-stream flow sees is the SD7003 scaled by a factor of $\sqrt{1+\tan^2\Lambda}$ along its chord as illustrated in Figure 5-1. Similarly, *span-wise* refers to the direction of the leading edge line, that is the y-direction.

The chord-wise Reynolds number, Re_x, thus denotes the Reynolds number in the direction normal to the leading edge line, and is kept at $Re_x = 60,000$. In this way, the flow in the chord-wise direction should be similar to the one for the high transitional regime of Section 4.3 except for the effects of coupling between the cross-flow and streamwise components as explained in Section 5.1.2. The effects of cross-flow on the boundary layer development and transition to turbulence can thus be assessed by comparing the results with $\Lambda \neq 0$ and those of Section 4.3. Note that the free-stream Reynolds number, $Re_\infty = Re_x\sqrt{1+\tan^2\Lambda} = Re_x/\cos\Lambda$, and the span-wise Reynolds number, $Re_y = Re_x \tan\Lambda$, vary with sweep angle.

The pressure and skin friction forces are non-dimensionalized with respect to the dynamic pressure projected along the chord-wise direction in order to obtain pressure and friction coefficients consistent with those of the un-swept wing and allow for a meaningful comparison. The forces are thus divided by $q_{\infty_x} = {}^1\!/_2\,\rho\,U^2_{\infty_x}$ instead of the usual $q_\infty = {}^1\!/_2\,\rho\,U^2_\infty$; this corresponds to a factor of $(1+\tan^2\Lambda)$. The coefficients of lift (force component normal to the free-stream direction) and drag

(force in the free-stream direction) are referred to as C_L and C_D, respectively, while $C_{L_x} = C_L\,(1+\tan^2\Lambda)$ and $C_{D_x} = C_D\,(1+\tan^2\Lambda)$ denote the chord-wise lift and drag coefficients, respectively, with respect to q_{∞_x}.

The arbitrary sign choice implied by the definition (3.13) of the cross-flow unit vector, $\hat{s}_2 = \hat{s}_1 \times \hat{n}$, results in a dominantly negative cross-flow. In order to avoid confusion, we refer to the average profile $-\overline{u}_2/\overline{u}_e$ as the *cross-flow pseudo-velocity profile* or simply as the *cross-flow velocity*.

In order to keep the computational cost manageable, all the cases presented in this chapter (includind those at $\Lambda = 0°$) are run on a grid which has the same resolution as grid 2 on the x-z planes, but whose span-wise resolution has been increased to 12 elements. Polynomials of order $p = 3$ are used, and hence the total number of unique span-wise nodes is 37. We shall call this computational mesh grid 2c. Less attention is paid to verifying the grid convergence of average quantities than previously and only this grid is used in swept-wing simulations, since the focus here is on how the cross-flow influences transition and on the trends with varying sweep angle. These are not expected to be qualitatively modified as long as the spatial resolution is close to adequate, and grid 2 proved so for the unswept wing cases.

5.1.2 Swept-Wing Theory

Let us consider the Navier-Stokes equations for a three-dimensional, steady, incompressible, laminar flow whose velocity vector has components u in the chord-wise x direction, v in the span-wise y direction, and w in the transverse z direction. It is reasonable to assume that the changes along the span-wise direction over a constant-chord swept-wing are much smaller than changes that occur along both the chord-wise and the transverse directions. This is a good approximation not only for small sweep angles, but for any sweep provided that one is far away from the wing ends (which is always the case for an infinite wing). The y-derivative terms ($\partial/\partial y$) can thus be neglected in front of x and z derivatives, and the governing equations simplified to

$$
\begin{aligned}
&\frac{\partial u}{\partial x} + \frac{\partial w}{\partial z} = 0 \\
&u\frac{\partial u}{\partial x} + w\frac{\partial u}{\partial z} = -\frac{1}{\rho}\frac{\partial p}{\partial x} + \nu\left(\frac{\partial^2 u}{\partial x^2} + \frac{\partial^2 u}{\partial z^2}\right) \\
&u\frac{\partial v}{\partial x} + w\frac{\partial v}{\partial z} = \nu\left(\frac{\partial^2 v}{\partial x^2} + \frac{\partial^2 v}{\partial z^2}\right) \\
&u\frac{\partial w}{\partial x} + w\frac{\partial w}{\partial z} = -\frac{1}{\rho}\frac{\partial p}{\partial z} + \nu\left(\frac{\partial^2 w}{\partial x^2} + \frac{\partial^2 w}{\partial z^2}\right) \quad .
\end{aligned}
$$

An interesting property of a flow governed by the above equations is that the components u and w are decoupled from v, but v depends on u and w. To make this clear consider the first, second, and last equations above, namely

$$\begin{cases} \dfrac{\partial u}{\partial x} + \dfrac{\partial w}{\partial y} = 0 \\ u\dfrac{\partial u}{\partial x} + w\dfrac{\partial u}{\partial z} = -\dfrac{1}{\rho}\dfrac{\partial p}{\partial x} + \nu\left(\dfrac{\partial^2 u}{\partial x^2} + \dfrac{\partial^2 u}{\partial z^2}\right) \\ u\dfrac{\partial w}{\partial x} + w\dfrac{\partial w}{\partial z} = -\dfrac{1}{\rho}\dfrac{\partial p}{\partial z} + \nu\left(\dfrac{\partial^2 w}{\partial x^2} + \dfrac{\partial^2 w}{\partial z^2}\right) \end{cases} . \tag{5.2}$$

This system can be solved for u, w, p (three equations, three unknown functions of x and z), irrespective of the span-wise velocity: it predicts the two-dimensional laminar boundary layer flow on the airfoil's plane. The additional equation

$$u\frac{\partial v}{\partial x} + w\frac{\partial v}{\partial z} = \nu\left(\frac{\partial^2 v}{\partial x^2} + \frac{\partial^2 v}{\partial z^2}\right) \tag{5.3}$$

defines v for given u and w. Hence, there is a one-way coupling between the laminar flow component in the span-wise direction and the components on the chord-wise plane: v depends on u and w, but the converse is not true.

Comparing the chord-wise boundary layer flow at different sweep angles thus allows to study the influence (if any) of the cross-flow present over swept wings on the boundary layer development and transition. The above analysis predicts no influence in the laminar boundary layer region; on the other hand, turbulence is a highly non-linear process which could be responsible for a two-way coupling in which the span-wise flow influences the chord-wise boundary layer evolution.

5.1.3 Boundary Layer Quantities

The cross-flow displacement thickness corresponds to the defect of cross-flow velocity ratio in the boundary layer relative to its edge value which is zero—since the cross-flow vanishes at the boundary layer edge by construction (see Section 3.7). Hence it is defined as

$$\delta_2^* = \int_0^{n_e} \left(0 - \frac{u_2}{u_e}\right) dn \,.$$

The momentum thickness is a tensor with four components

$$\theta_{11} = \int_0^{n_e} \left(1 - \frac{u_1}{u_e}\right) \frac{u_1}{u_e}\, dn \quad , \quad \theta_{12} = \int_0^{n_e} \left(1 - \frac{u_1}{u_e}\right) \frac{u_2}{u_e}\, dn \quad ,$$

$$\theta_{21} = \int_0^{n_e} \left(0 - \frac{u_2}{u_e}\right) \frac{u_1}{u_e}\, dn \quad , \quad \theta_{22} = \int_0^{n_e} \left(0 - \frac{u_2}{u_e}\right) \frac{u_2}{u_e}\, dn \ .$$

Note that, on average, the cross-flow pseudo-velocity u_2 is negative over most of the boundary layer, and hence all the thicknesses δ_i^*, θ_{ij} are positive values except for θ_{12}. These integral quantities defined in the local streamwise, cross-flow reference frame are different for different sweep angles.

In order to decouple any linear effects, it is useful to consider the chord-wise quantities

$$\delta_x^* = \int_0^{n_e} \left(\frac{u_{e_x}}{u_e} - \frac{u_x^*}{u_e}\right) dn \ , \tag{5.4}$$

$$\theta_{xx} = \int_0^{n_e} \left(\frac{u_{e_x}}{u_e} - \frac{u_x^*}{u_e}\right) \frac{u_x^*}{u_e}\, dn \ , \tag{5.5}$$

in which $u_e = |\vec{u}_e^*| = |\vec{u}^*(n_e)|$ is the boundary layer edge pseudo-velocity magnitude, and u_x^* the component of the pseudo-velocity $\vec{u}^*$ in the chord-wise x direction. In a two-dimensional boundary layer, the displacement and momentum thicknesses are

$$\delta^* = \int_0^{n_e} \left(1 - \frac{u_x^*}{u_{e_x}}\right) dn \ ,$$

$$\theta = \int_0^{n_e} \left(1 - \frac{u_x^*}{u_{e_x}}\right) \frac{u_x^*}{u_{e_x}}\, dn \ .$$

A meaningful comparison of the average boundary layer integral quantities can thus be obtained by considering the *two-dimensional equivalent* values for any given sweep angle and at any chord-wise location through the relations

$$\delta^* = \frac{u_e}{u_{e_x}}\, \delta_x^* \ , \tag{5.6}$$

$$\theta = \left(\frac{u_e}{u_{e_x}}\right)^2 \theta_{xx} \ , \tag{5.7}$$

in which the ratio u_e/u_{e_x} (equal to the x component of the streamwise unit vector $\hat{s}_1$) accounts for the effect of sweep on the boundary layer development: it is unity for $\Lambda = 0°$, and increases as the sweep angle increases. The effect of the cross-flow on the chord-wise boundary layer can thus be assessed by comparing the two-dimensional equivalents δ^*, θ, and $H = \delta^*/\theta$ for various sweep angles, and is done in Section 5.3.

5.2 Results at 30° Sweep Angle

The flow around a wing with sweep angle $\Lambda = 30°$ is first considered in detail. After determining that a span domain length of $0.2c$ is sufficient to capture the mean flow features, the average results are compared with those of the un-swept wing.

5.2.1 Effect of Domain Span Length

The presence of a span-wise velocity component may change the characteristic span-wise length of the flow structures, and hence the flow in a domain with $0.2c$ span is compared to that for a $0.3c$ domain span. Figure 5-2 shows the time evolution of lift, drag, and span-wise force coefficients for both cases. Figure 5-3 shows the pressure and skin friction coefficients and Figure 5-4 the boundary layer integral parameters of the average flow on the wing. As for the un-swept wing (Section 4.3.3), the forces are similar, the average pressure and skin forces are undistinguishable, and the small difference in boundary layer quantities after transition can be attributed to a lack

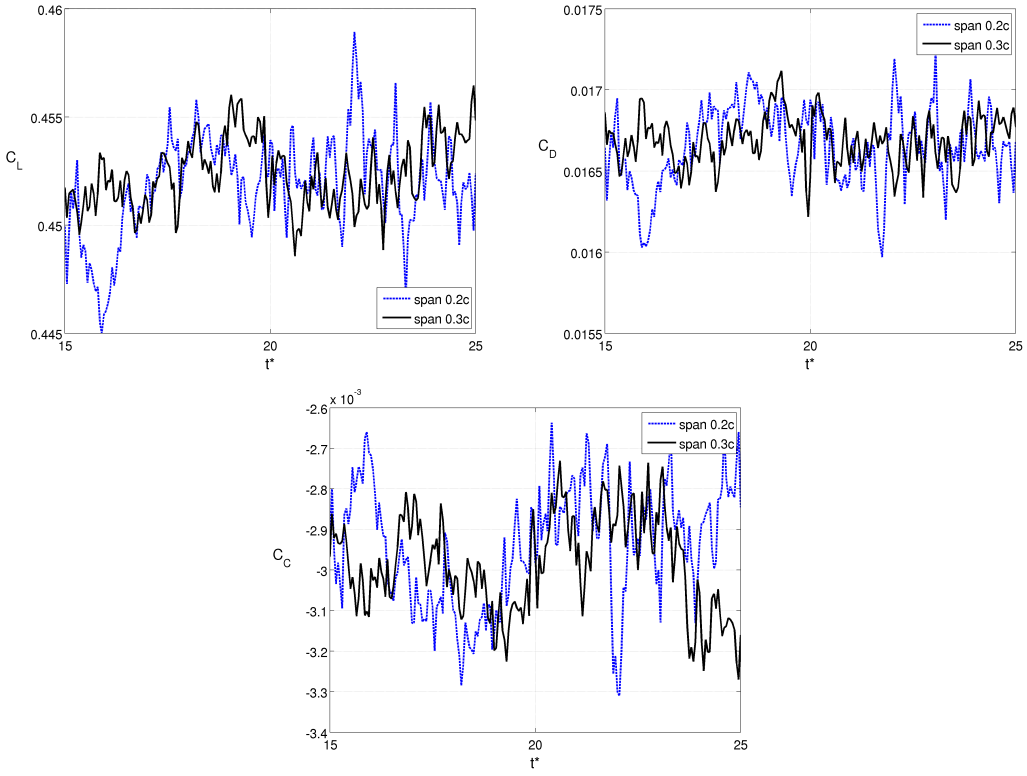

Figure 5-2: Time variation of lift (top left), drag (top right), and span-wise (bottom) force coefficients for 30° sweep wing at $Re_x = 60,000$ on grid 2c: comparison of grids with two different span lengths.

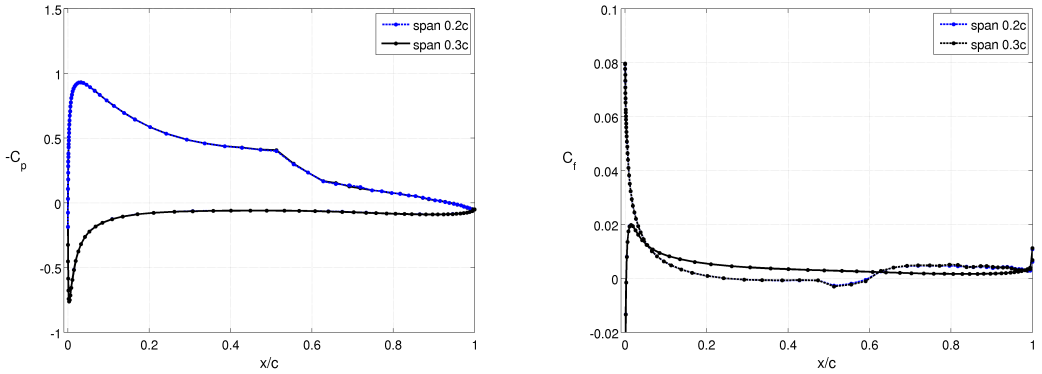

Figure 5-3: Average pressure coefficient (left) and chord-wise skin friction coefficient (right) for 30° sweep wing at $Re_x = 60,000$: comparison of grids with two different span lengths.

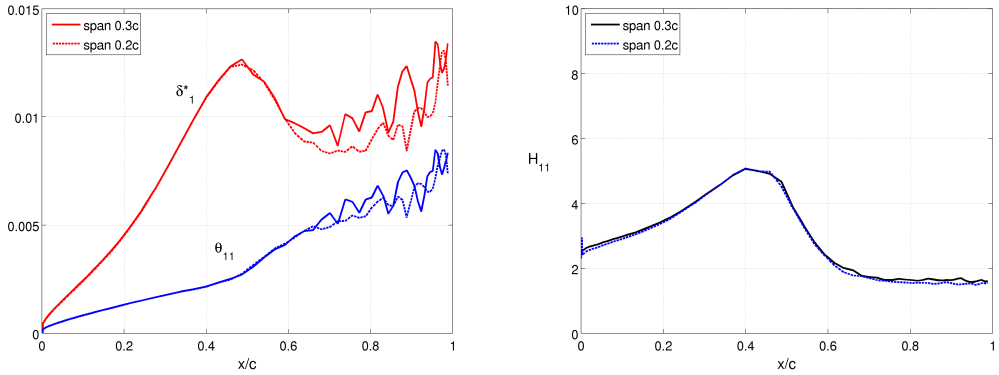

Figure 5-4: Boundary layer average streamwise displacement and momentum thicknesses (left), and shape factor (right) evolution along the chord-wise direction for 30° sweep wing at $Re_x = 60,000$: comparison of grids with two different span lengths.

of statistical convergence of the time-average flow and not to the difference in the domain's span. Hence, a domain with a span length of $0.2c$ and span-wise periodic boundary conditions is deemed adequate to capture the mean flow features of an infinite wing even with a span-wise free-stream component corresponding to $\Lambda = 30°$.

This span should also be adequate for any other sweep angle: for larger sweeps, the span-wise extent of any flow structures is more likely to decrease than increase; and for smaller Λ, this domain span should be enough since it was sufficient at $\Lambda = 0$.

5.2.2 Comparison with Un-Swept Wing

Now the results for a 30° sweep wing are compared with those of an un-swept one. To provide a meaningful comparison, the results referred to here as un-swept wing are obtained on grid 2c, and are slightly different than those of the previous chapter.

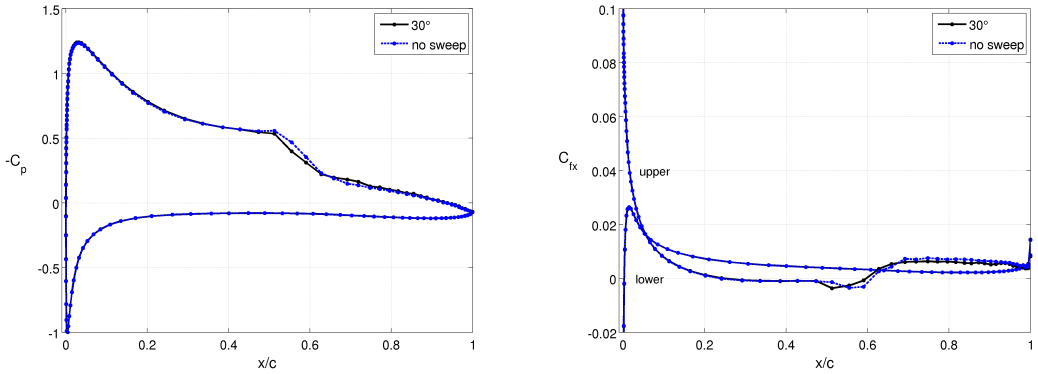

Figure 5-5: Average pressure coefficient (left) and chord-wise skin friction coefficient (right): comparison of un-swept and 30° sweep wing at $Re_x = 60,000$ on grid 2c.

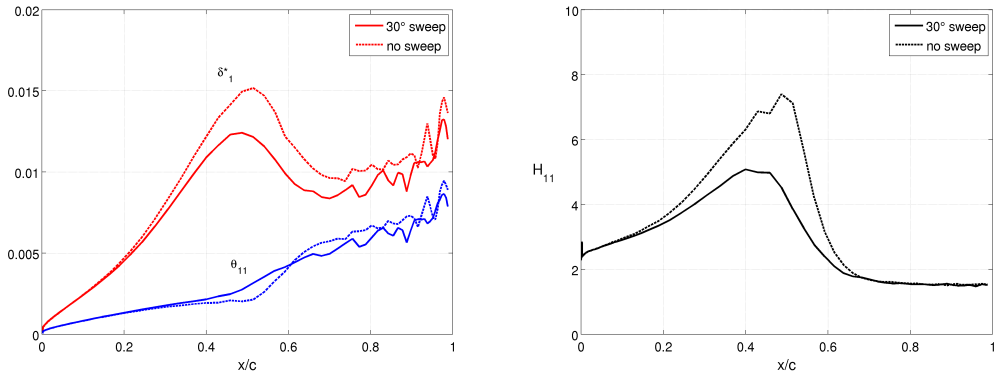

Figure 5-6: Boundary layer average streamwise displacement and momentum thicknesses (left), and shape factor (right) evolution along the chord-wise direction: comparison of un-swept and 30° sweep wing at $Re_x = 60,000$ on grid 2c.

Figure 5-5 shows the pressure and chord-wise skin friction coefficients for both $\Lambda = 0$ and $\Lambda = 30°$, while Figure 5-6 provides a comparison of the boundary layer streamwise displacement thickness, momentum thickness, and shape factor. As mentioned previously, non-dimensionalization of pressure and skin friction forces is done with respect to the free-stream dynamic pressure projected along the chord-wise direction, q_{∞_x}, which is the same for swept and un-swept wings since $Re_x = 60,000$ for both. The separation location does not change much (5% farther downstream for the swept wing), but transition does occur significantly earlier (18%) in the presence of cross-flow. This, and the considerations that follow, shows that the presence of a cross-flow component destabilizes the streamwise velocity profile.

The inviscid streamline can be seen in Figure 5-7: as expected, it is inclined at an angle smaller than the sweep angle (or free-stream direction), and is subject to leading-edge and trailing-edge effects. The average iso-surfaces of q-criterion of Fig-

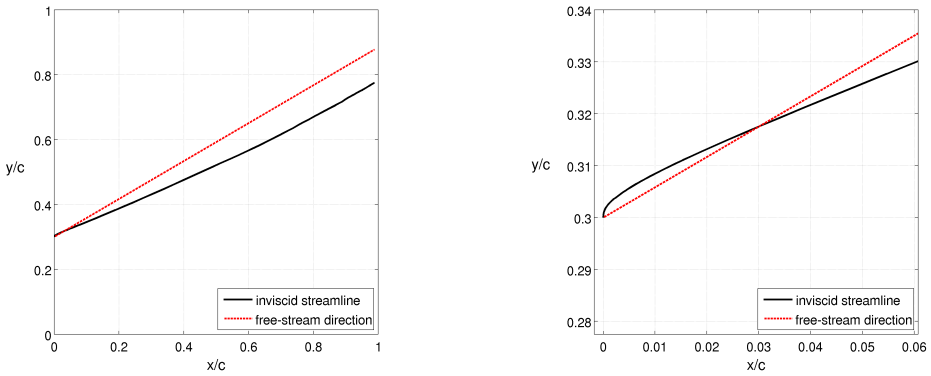

Figure 5-7: Inviscid streamline over the upper surface of the 30° sweep wing at $Re_x = 60,000$ on grid 2c: (left) entire domain and (right) close look at the leading edge region; the dotted line shows the free-stream direction.

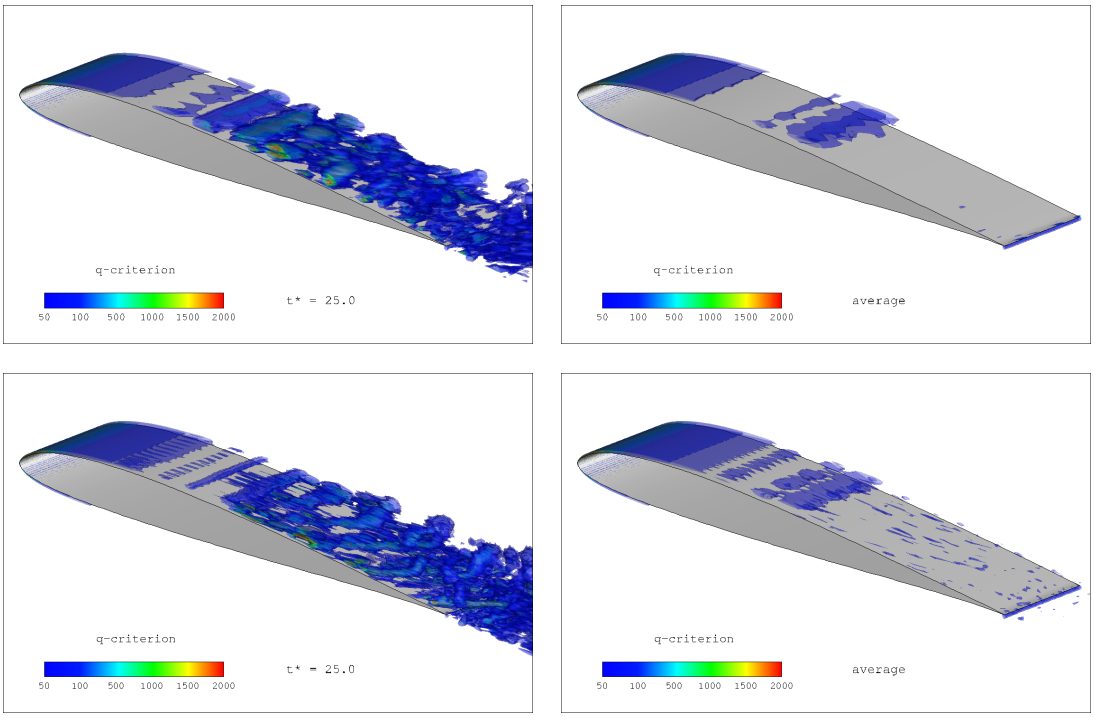

Figure 5-8: Instantaneous (left) and average (right) iso-surfaces of q-criterion for unswept wing (top) and wing with 30° sweep (bottom) at $Re_x = 60,000$ with grids 2 and 2c, respectively.

ure 5-8 show that the swept wing generates more vortical structures, in particular closer to the leading edge (around the quarter-chord point), than the un-swept wing; this is consistent with the fact that the flow becomes unstable earlier. Furthermore, the noise in the average iso-surfaces on the downstream half of the swept wing indicates that averages over more time steps is needed due to the presence of smaller, higher-frequency structures over the swept wing.

The average and fluctuating profiles of streamwise pseudo-velocity at different chord-wise locations for $\Lambda = 30°$ of Figure 5-9 are qualitatively similar to those without cross-flow. The streamwise profile at $x/c = 0.1$ with and without sweep can be seen in Figure 5-10: the difference, though very small, is largest on the half of the boundary layer thickness close to the wall where shear stress is important.

The cross-flow pseudo-velocity profiles, $-\overline{u}_2/\overline{u}_e$, of Figure 5-11 confirm that the cross-flow is zero both at the wall and at the boundary layer edge. Moreover, close to the wing's leading edge the cross-flow has an S-shaped profile with two inflection points: the cross-flow velocity $-\overline{u}_2/\overline{u}_e$ goes from being positive near the wall (*i.e.* cross-flow dircted towards the root of a wing with backward sweep), to negative near the boundary layer edge before asymptoting to zero at the edge. Downstream of $x/c \approx 0.13$, the cross-flow velocity remains of the same sign (positive) all the way from the wall up to the boundary layer edge and the profile has a single inflection point. The cross-flow velocity direction is consistent with the description given in Section 2.4 where the cross-flow is described to be directed towards the root on the upstream part of a wing with positive sweep.

A quantitative measure of how much cross-flow is present is given by the value of the maximum average cross-flow, $\max\left(-\overline{u}_2/\overline{u}_e\right)$, along the chord-wise direction shown on the left plot of Figure 5-12: the black line indicates that the maximum cross-flow increases linearly as we move downstream up to the transition location of $x_{tr}/c = 0.3996$, while the dotted blue line shows that the location of maximum cross-flow moves away from the wall as we move downstream down towards transition. The large variations past transition can probably be explained, again, by the need for computing time averages over more steps.

The right-hand-side of Figure 5-12 shows how the value of the minimum cross-flow velocity (the local extrema near the boundary layer edge which gives the cross-flow profile an S-shape) increases as we move downstream, and eventually becomes zero thus leaving a cross-flow profile with a single inflection point. Furthermore, as this happens, the locus of minimum negative cross-flow moves closer and closer to the boundary layer edge as indicated by the dotted blue line in the figure.

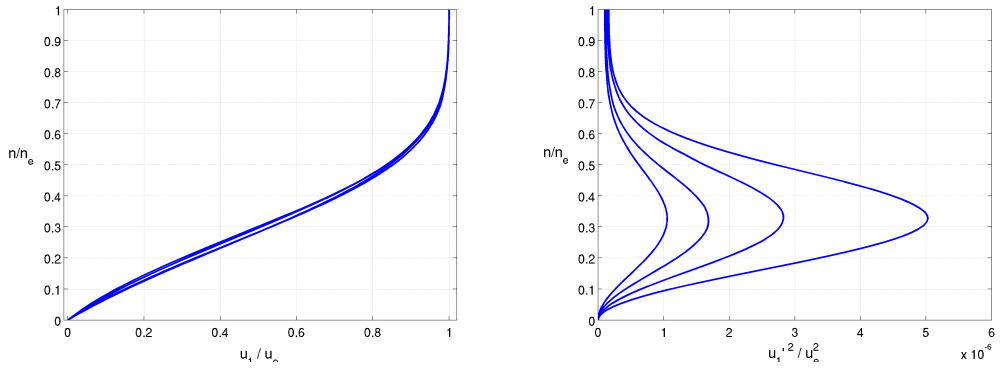

Figure 5-9: Boundary layer average profiles of streamwise pseudo-velocity $\overline{u}_1/\overline{u_e}$ (left), and fluctuating streamwise pseudo-velocity $\overline{u_1'^2}/\overline{u_e^2}$ (right), at different chord-wise locations $x/c \in [0.1, 0.15]$ for 30° sweep wing at $Re_x = 60,000$ with grid 2c.

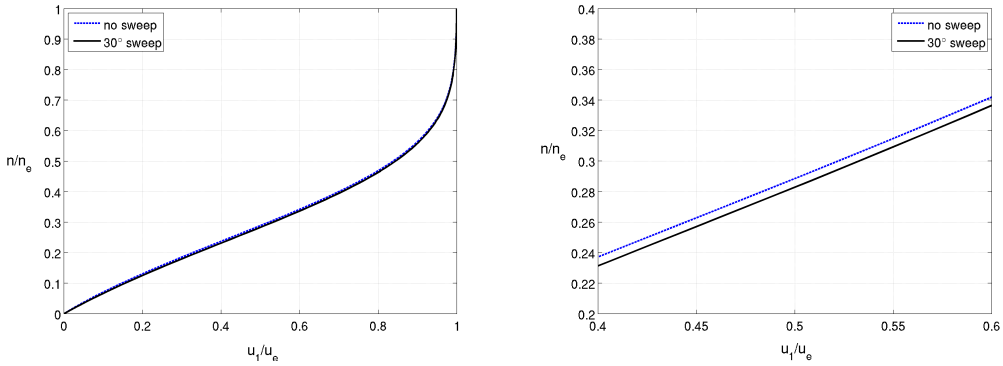

Figure 5-10: Boundary layer average streamwise profile $\overline{u}_1/\overline{u_e}$ at $x/c = 0.1$: comparison of un-swept and 30° sweep wing at $Re_x = 60,000$ on grid 2c.

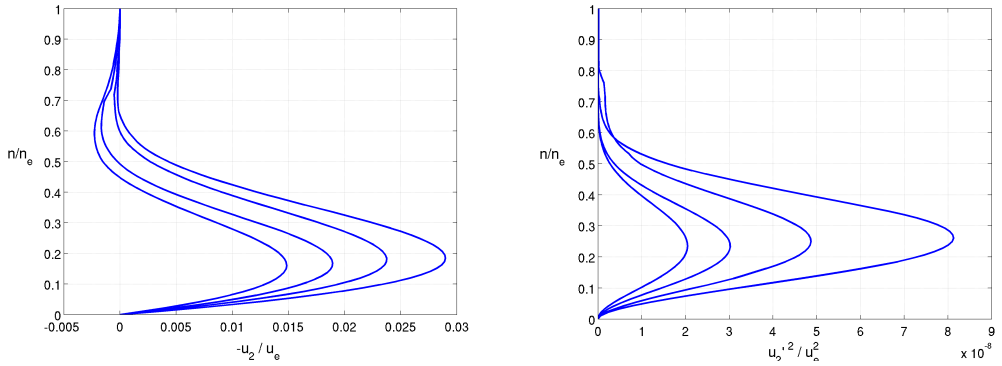

Figure 5-11: Boundary layer average profiles of cross-flow pseudo-velocity $-\overline{u}_2/\overline{u_e}$ (left), and fluctuating cross-flow pseudo-velocity $\overline{u_2'^2}/\overline{u_e^2}$ (right), at different chord-wise locations $x/c \in [0.1, 0.15]$ for 30° sweep wing at $Re_x = 60,000$ with grid 2c.

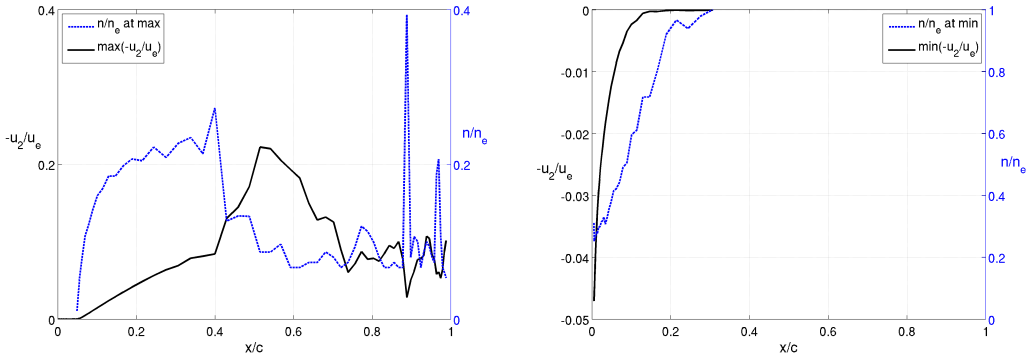

Figure 5-12: Values and locations of maximum (left) and minimum (right) average cross-flow velocity $-\overline{u}_2/\overline{u}_e$ for 30° sweep wing and $Re_x = 60,000$ with grid 2c.

A comparison of streamwise amplification factor, N_1, evolution between the wing without cross-flow and the wing at $\Lambda = 30°$ can be seen in Figure 5-13. As expected and as confirmed by the earlier occurring transition, the amplification factor grows faster in the presence of cross-flow (slope of 16 in the region of linear increase where disturbances grow exponentially) than for the un-swept wing (linear slope of 13).

However, the streamwise profiles with and without sweep only differ slightly as shown in Figure 5-10. If one solves the Orr-Sommerfeld equations for both of these profiles, the resulting growth factors differ only by about 3%, thus proving that the change in streamwise profiles is insignificant from a stability point of view. As explained in the background section, the cross-flow/TS interaction is particularly important since the cross-flow velocity magnitude is significant near the wall (highest at around 20% of the boundary layer thickness here) which is a region of high shear

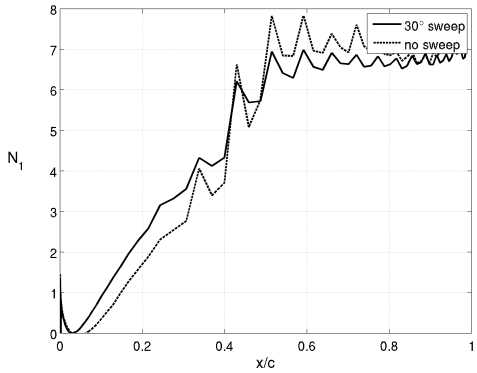

Figure 5-13: Amplification factor N_1 of streamwise perturbations: comparison of un-swept and 30° sweep wing at $Re_x = 60,000$ on grid 2c.

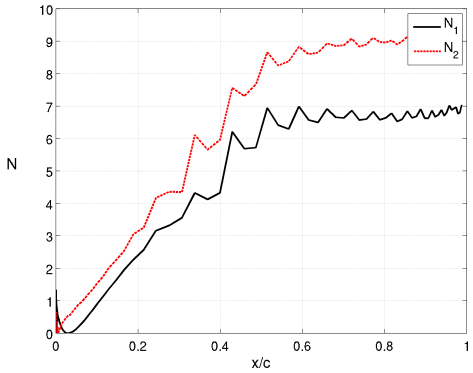

Figure 5-14: Streamwise and cross-flow amplification factors, N_1 and N_2 respectively, for 30° sweep wing at $Re_x = 60,000$ with grid 2c.

where the streamwise profile has a large gradient. Thus, even more than modifying the streamwise profile, the presence of a cross-flow velocity modifies the stability of the overall flow: the transition over the 30° swept wing is not solely caused by the growth of TS waves, but is a mixed result of streamwise and cross-flow disturbances. We shall come back to this important fact later.

With $\Lambda = 30°$, the cross-flow amplification factor N_2 plotted in Figure 5-14 has a similar slope (close to 15) in the linear-growth region as the streamwise amplification factor N_1, but a larger normalized magnitude at any given chord-wise location. However, this does not allow us to determine whether transition is caused by the growth of TS waves or by cross-flow disturbances: the threshold where transition occurs might not be the same for both amplification factors, and there is no currently known value of critical cross-flow amplification factor—the determination of an appropriate value being outside the scope of the present research, especially since the mechanism of cross-flow instability might not be as accurately reduced to the amplification of cross-flow disturbances as purely TS transition is.

5.3 Effects of Sweep Angle

Having seen how the presence of cross-flow induced by a 30° sweep can accelerate transition, we now quantify how different sweep angles affect the boundary layer development by considering values of $\Lambda \in \{0°, 1°, 5°, 10°, 20°, 30°, 40°, 50°, 60°\}$. The results are summarized in Table 5.1.

5.3.1 Forces

When normalizing the forces with respect to the chord-wise dynamic pressure, q_{∞_x}, there is little change in lift coefficient, C_{Lx}, which remains at 0.6 within about 5% for all sweep angles considered as illustrated in Figure 5-15 (blue line with triangles). Indeed, lift is primarily the result of pressure forces which, when normalized properly, change little with sweep angle and only in the region close to transition as can be seen in Figure 5-16. On the other hand, the drag coefficient, C_{Dx}, increases for sweep angles of 30° and more, probably due to the rise in friction coefficient associated with an earlier transition, as well as to some non-linear effects in the interaction between streamwise and cross-flow components. As expected, the third coefficient of force, C_{Cx}, (in the direction normal to both lift and drag) increases almost linearly with Λ.

Table 5.1: Summary of average flow results for swept wings at $Re_x = 60,000$ and 4° angle of attack on grid 2c.

Sweep Angle	0°	1°	5°	10°	20°	30°	40°	50°	60°
C_L	0.6030	0.6036	0.5987	0.5849	0.5316	0.4519	0.3530	0.2496	0.1499
C_{Lx}		0.6038	0.6033	0.6031	0. 6021	0.6025	0.6015	0.6042	0.5994
C_D	0.02184	0.02190	0.02182	0.02114	0.01928	0.01665	0.01379	0.01065	0.00760
C_{Dx}		0.02191	0.02198	0.02179	0.02183	0.02220	0.02350	0.02579	0.03042
$-C_C$	-	0.00009	0.00066	0.00132	0.00246	0.00294	0.00287	0.00251	0.00176
$-C_{Cx}$		0.00009	0.00067	0.00137	0.00278	0.00392	0.00489	0.00608	0.00703
x_{sep}/c from C_{fx}	0.2365	0.2374	0.2360	0.2387	0.2431	0.2485	0.2515	0.2498	0.2460
x_{sep}/c from $H = 4$	0.2380	0.2390	0.2372	0.2404	0.2450	0.2483	0.2502	0.2492	0.2468
x_{tr}/c from H_{11}	0.4870	0.4870	0.4870	0.4586	0.4586	0.3996	0.3996	0.3996	0.3996
x_{tr}/c from H		0.4850	0.4980	0.4870	0.4710	0.4560	0.4560	0.4450	0.4470
x_r/c from C_{fx}	0.6121	0.6104	0.6107	0.6076	0.6008	0.5968	0.6009	0.6009	0.5939
x_r/c from $H = 4$	0.5637	0.5716	0.5703	0.5628	0.5566	0.5439	0.5372	0.5384	0.5470
$\max(H_{11})$	7.4000	7.7418	7.2925	6.5602	5.8552	5.0812	4.6081	4.1548	3.7707
$\max(H)$		7.7472	7.3756	6.7746	6.5794	6.2124	5.9570	5.8463	5.9160
$\max(-\overline{u}_2/\overline{u}_e)$ at $x/c = 0.1$	-	0.000538	0.002622	0.005189	0.010127	0.014651	0.018426	0.020914	0.020816
maximum x/c with $-\overline{u}_2 < 0$	0	0.0020	0.0787	0.1006	0.1139	0.1291	0.1291	0.1464	0.1291
$dN_1/d(x/c)$	13.16	14.81	12.42	12.62	15.74	16.06	14.67	16.58	12.59
$dN_2/d(x/c)$	-	13.07	7.20	8.12	14.27	15.11	9.73	12.97	9.15
N_1 at x_{tr}/c	6.3	5.9	5.5	5.7	5.9	4.4	4.4	4.6	4.3
N_2 at x_{tr}/c	-	10.4	8.8	8.5	8.1	6.8	6.2	6.5	5.7

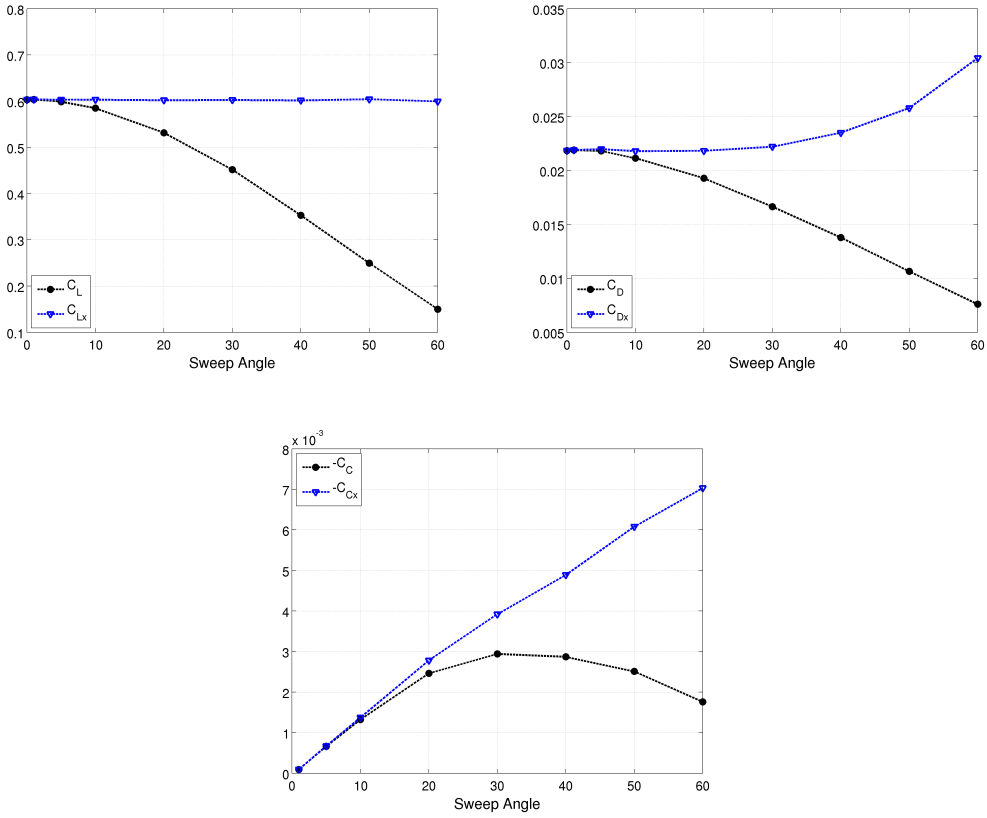

Figure 5-15: Variation of force coefficients with sweep angle at $Re_x = 60,000$ with grid 2c: lift coefficient (top left), drag coefficient (top right), and span-wise force coefficient (bottom). The subscript x and dotted lines with triangles refer to the force coefficients non-dimensionalized with respect to the chord-wise dynamic pressure q_{∞_x}.

If we now look at the lift and drag as commonly defined with respect to the free-stream (C_L and C_D black lines and circles of Figure 5-15), both lift and drag decrease close to linearly for moderate and large sweep angles ($\Lambda \geq 20°$) as occurs when a wing is swept and its profile is effectively elongated. It is interesting that the third force component increases and then decreases, having a maximum at around $\Lambda = 30°$; however, in a typical vehicle configuration with two symmetric wings, this lateral force would be counteracted by an equal and opposite one from the other wing, and hence would have no impact on the overall aerodynamics of the vehicle.

5.3.2 Separation, Transition, Reattachment

Separation occurs almost at the same chord-wise location across all sweep angles, as measured from the two-dimensional equivalent shape factor and the common location where $H = 4$ (Figure 5-20). The earliest and latest separations are observed at 24%

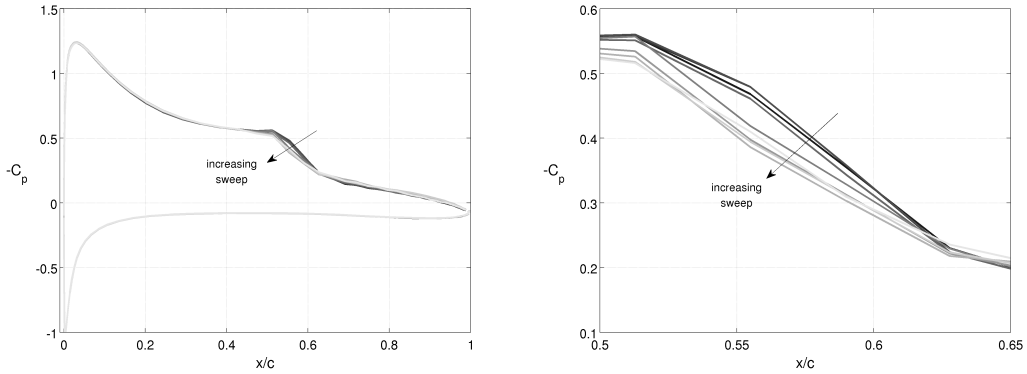

Figure 5-16: Average pressure coefficient profiles (left) and closer view on transition region (right): comparison between sweep angles of $\{0°, 1°, 5°, 10°, 20°, 30°, 40°, 50°, 60°\}$ at $Re_x = 60,000$ with grid 2c.

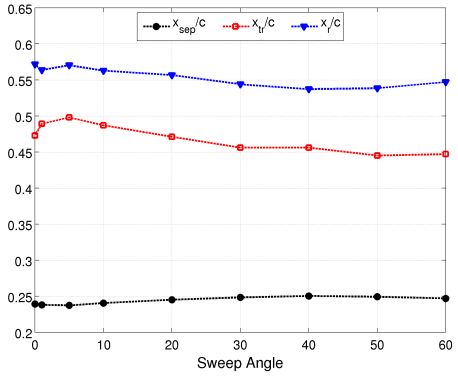

Figure 5-17: Variation of separation x_{sep}/c, transition x_{tr}/c, and reattachment x_r/c locations with sweep angle at $Re_x = 60,000$ with grid 2c.

and 25% of the chord, respectively, showing that separation location varies only by about than 6% (moving upstream by less than 1.5% of the chord) even for sweep angles up to 60° as illustrated in Figure 5-17.

The separation location is basically left unchanged since, for all sweep angles at these low Reynolds numbers, the boundary layer separates while being laminar and hence separation is determined by the chord-wise pressure gradient. The presence of more or less cross-flow at the different sweep angles influences the growth of disturbances, but has no effect on the laminar boundary layer development and separation.

On the contrary, transition does vary significantly with sweep angle as can be readily observed in the pressure coefficient on the wing's upper surface shown in Figure 5-16. Transition location is determined by computing the boundary layer two-dimensional equivalent shape factor H (Figure 5-20) and measuring its peak. Transition takes place between $0.445c$ and 0.498, a close to 12% difference, and for

$\Lambda \geq 5°$ moves farther and farther upstream (by as much as 5% of the chord) as the sweep angle is increased.

The reattachment location is more accurately measured as the place where the shape factor H goes back down to a value of 4 after transition—since the friction coefficient is not a good measure of the flow nature, especially aft of separation. Transition occurring earlier for larger sweep angles, the flow reattaches faster as expected. Reattachment takes place as late as $x_r/c = 0.5716$ for the un-swept wing, but moves up to $0.5372c$ for $\Lambda = 40°$: reattachment is pushed upstream by as much as 3.5% of the chord. This represents a difference of only 6% while transition between these two cases moves upstream by 12%; this is to be explained by the fact that turbulent flow fluctuations do create more momentum but not all of the momentum gain is readily organized into a shear layer shape that induces reattachment.

To summarize, the change in transition location (by up to $0.05c$) is more significant than the change in both separation (up to $0.015c$) and reattachment (up to $0.035c$) locations: transition is dominated by the growth of unstable perturbations and hence strongly influenced by the presence of a destabilizing cross-flow, while laminar separation is set by the pressure gradient which is left unchanged in the chord-wise direction. Reattachment (influenced both by the unchanged pressure gradient and the moving transition) does globally move upstream due to the faster transition, thus making the laminar separation bubble slightly shorter for larger sweeps.

It is important to note that the uncertainly in determining the relevant locations is not insignificant, in particular at small sweep angles. In particular, transition is taken at the location of the peak in the two-dimensional equivalent shape factor, and the peak region is not smooth given the relative coarseness of the grid employed.

5.3.3 Boundary Layer

The plots of streamwise boundary layer displacement thickness, momentum thickness, and shape factor of Figure 5-18 show a continuous change in boundary layer shape (except for the case at $\Lambda = 1°$) as the sweep angle is increased: the peak in H_{11} moves upstream and its maximum value decreases as quantified in Figure 5-21. Even a small sweep angle of $\Lambda = 10°$—which induces only little cross-flow and small cross-flow perturbations—is enough to change the stability characteristics of the streamwise boundary layer profile, as evidenced by the change (about 13%) in $\max(H_{11})$ between $\Lambda = 0°$ and $10°$. As the sweep angle is increased further, the maximum shape factor continues to decrease but at a lower and lower rate.

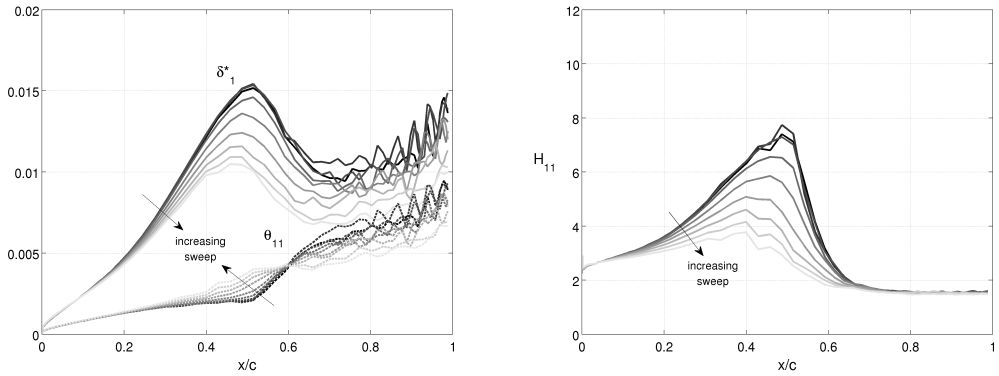

Figure 5-18: Boundary layer average streamwise displacement and momentum thicknesses (left), and shape factor (right) evolution for sweep angles of $\{0°, 1°, 5°, 10°, 20°, 30°, 40°, 50°, 60°\}$ at $Re_x = 60,000$ with grid 2c.

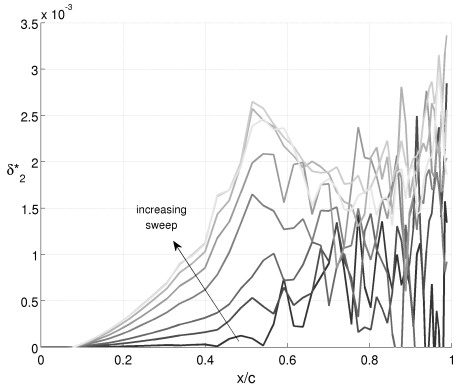

Figure 5-19: Boundary layer average cross-flow displacement thickness evolution for sweep angles of $\{0°, 1°, 5°, 10°, 20°, 30°, 40°, 50°, 60°\}$ at $Re_x = 60,000$ with grid 2c.

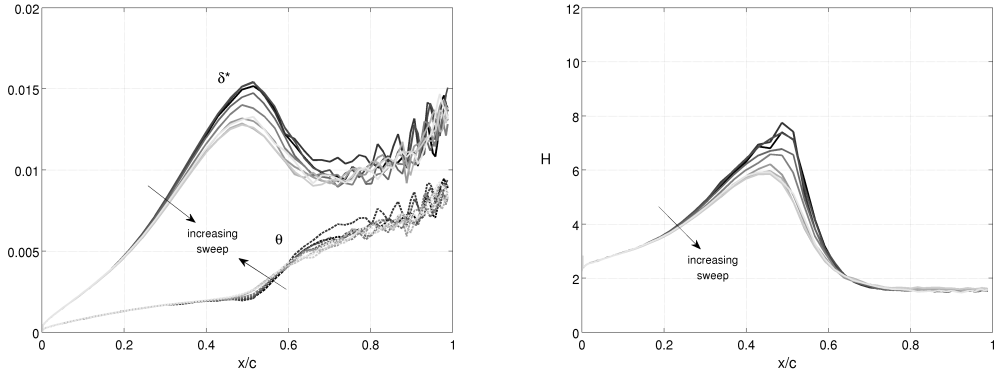

Figure 5-20: Boundary layer average two-dimensional equivalent chord-wise displacement and momentum thicknesses (left), and shape factor (right) evolution for sweep angles of $\{0°, 1°, 5°, 10°, 20°, 30°, 40°, 50°, 60°\}$ at $Re_x = 60,000$ with grid 2c.

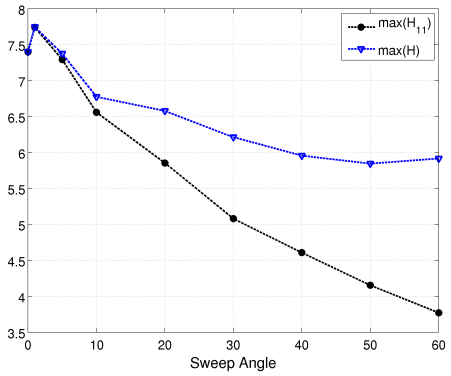

Figure 5-21: Variation of boundary layer streamwise shape factor maximum, $\max(H_{11})$, and two-dimensional equivalent shape factor maximum, $\max(H)$, with sweep angle at $Re_x = 60,000$ with grid 2c.

The cross-flow displacement thickness becomes larger and larger at any chord-wise location when the sweep angles increases as can be seen in Figure 5-19: larger sweep angles generate more cross-flow and hence a larger δ_2^* by its definition (5.1.3).

As explained in Section 5.1.3, since the chord-wise characteristics are held constant for all sweeps (same airfoil profile, angle of attack, chord-wise Reynolds number) the two-dimensional-equivalent quantities δ^*, θ, H can provide a meaningful comparison by decoupling the cross-flow components from the purely chord-wise boundary layer evolution. In other words, if the cross-flow and streamwise effects are only linearly coupled, the two-dimensional-equivalent curves for different sweep angles should collapse into a single line.

Comparing the plots of δ^*, θ, H in Figure 5-20 clearly demonstrates that the span-wise (and cross-flow) effects cannot be considered independently of the chord-wise (and streamwise) evolution for sweep angles between 10° and 30°: the influence of the latter on the former is non-linear. On the other hand, for $\Lambda \in \{0°, 1°, 5°\}$ the two-dimensional equivalent boundary layer curves collapse, indicating that only linear interactions occur; the same happens for sweep angles of 40° and larger.

This is evident in most of the curves presented next, as well as on Figure 5-21 which shows the maximum in H: if we ignore the $\Lambda = 1°$ point, the curve is flat between 0° and 5° sweep, and then again for $\Lambda \geq 40°$. In between, the interaction between cross-flow and streamwise components is non-linear and there is a continuous decrease in the H peak as the sweep angle is increased.

In the laminar region, all the curves of two-dimensional equivalent boundary layer integral quantities overlap: if the cross-flow affects streamwise disturbances, these

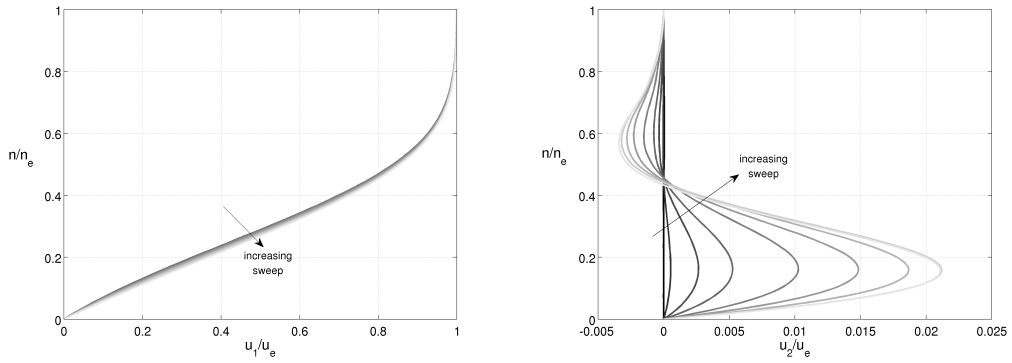

Figure 5-22: Boundary layer average profiles of streamwise $\overline{u}_1/\overline{u_e}$ (right) and cross-flow $-\overline{u}_2/\overline{u_e}$ (left) pseudo-velocity at $x/c \in [0.1, 0.15]$ for sweep angles of $\{0°, 5°, 10°, 20°, 30°, 40°, 50°, 60°\}$ at $Re_x = 60,000$ with grid 2c.

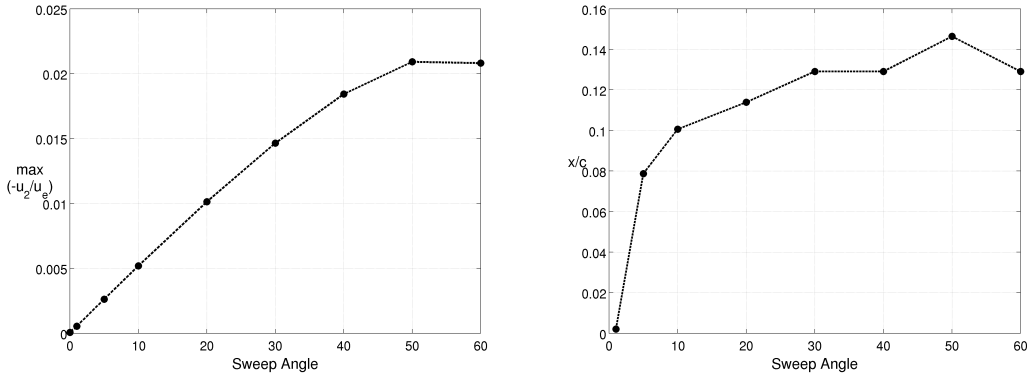

Figure 5-23: Variation of the average boundary layer cross-flow pseudo-velocity profile $-\overline{u}_2/\overline{u}_e$ characteristics with sweep angle at $Re_x = 60,000$ with grid 2c: maximum at $x/c = 0.1$ (left) and chord-wise location where the profile stops being S-shaped, that is where $\min(\overline{u}_2/\overline{u}_e) \geq 0$ (right).

play no role in the laminar boundary layer development. Once separation occurs, the disturbances are rapidly amplified and the interactions become highly non-linear: the largest difference between the curves occurs around the transition region where disturbance growth and their interactions dominate the shear layer evolution.

Note that the curves of boundary layer quantities at 0° and 1° sweep in Figures 5-18 and 5-20 are not smooth near transition. This can be attributed to the coarseness of the grids being used and to the very high sensitivity of boundary layer quantities near transition to spatial resolution. Furthermore, the uncertainty in determining the separation, transition, and reattachment locations shows in Figure 5-17 is relatively large. Therefore, while we believe the major trends discussed in this section can

be trusted, the exact values could benefit from a more accurate solution; this is particularly true at certain sweep angles (0° and 1° certainly, and probably also 10°) and it is thus not possible to draw all of the conclusions with confidence.

As the average streamwise and cross-flow pseudo-velocity profiles of Figure 5-22 show, the streamwise flow is only slightly modified but the cross-flow component sees significant changes with varying sweep angle. In particular, the value of the maximum cross-flow velocity at any given chord-wise location, *e.g.* at $x/c = 0.1$ as in the plots on the left of Figure 5-23, increases while its minimum (second extrema near the boundary layer edge of S-shaped profiles) decreases when Λ increases. This is similar to what happens when moving downstream in the chord-wise direction: the cross-flow profiles becomes more and more unstable as we either move downstream or increase the sweep angle. Again, this indicates that the cross-flow has a destabilizing effect.

From the precise variation of maximum cross-flow velocity with sweep angle at $x/c = 0.1$ of Figure 5-23, it can be noted that the maximum cross-flow value increases linearly up to about $\Lambda = 40°$ before starting to level off. This saturation suggests that increasing the sweep cannot result in an arbitrarily large cross-flow.

Similarly, there seems to be a limit of how far downstream cross-flow S-shaped profiles (*i.e.* profiles with two-inflection points) can exist, all the profiles having a single inflection point far enough downstream—even long before separation. As the right plot of Figure 5-23 shows, S-shaped profiles are present in longer and longer regions near the leading edge as the sweep angle is increased, but their spatial extent does not seem to increase above about $0.14c$ where the curve levels off for $\Lambda \geq 30°$.

5.3.4 Amplification Factors

The streamwise and cross-flow amplification factors, N_1 and N_2, for different sweep angles can be seen in Figure 5-24. Contrarily to the average boundary layer integral quantities, the change in amplification factors is not uniform with sweep angle: the growth (even linear) of disturbances is more complex than the average boundary layer development, and a simple correlation seems unlikely. However, this hypothesis needs to be verified with better resolved simulations, as the average results at some of the sweep angles are particularly noisy.

Correspondingly, the slopes of streamwise and cross-flow amplification factors in their linear regions vary non-uniformly with sweep angle as quantified in Figure 5-25. The linear slope of N_1 varies by as much as 30% with sweep angle, and an even larger change is observed in the growth of the cross-flow disturbances which almost doubles

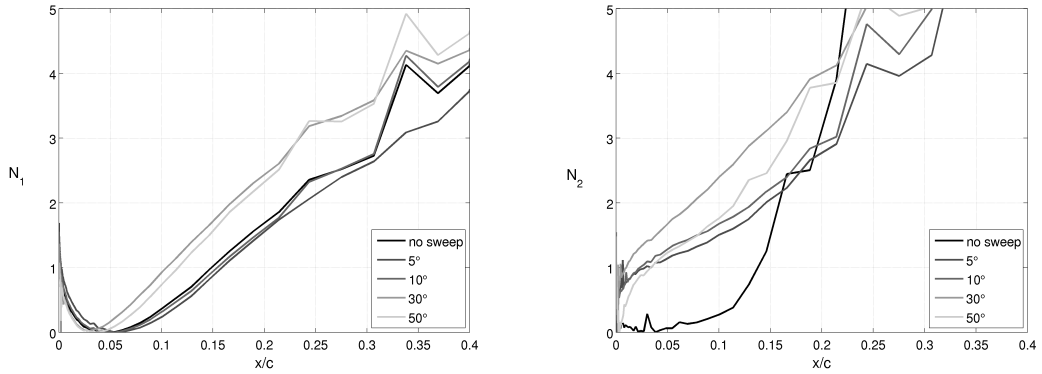

Figure 5-24: Streamwise amplification factor N_1 (left), and cross-flow amplification factor N_2 (right): comparison of different sweep angles at $Re_x = 60,000$ with grid 2c.

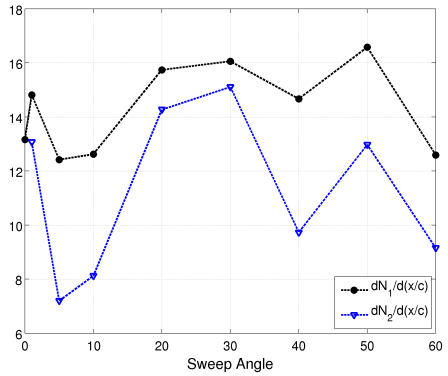

Figure 5-25: Variation of streamwise and cross-flow amplification factor slopes in the linear-growth region, $dN_1/d(x/c)$ and $dN_2/d(x/c)$, with sweep angle at $Re_x = 60,000$ with grid 2c.

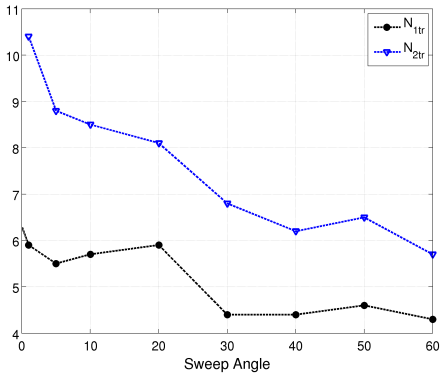

Figure 5-26: Variation of streamwise and cross-flow amplification factors at transition with sweep angle at $Re_x = 60,000$ with grid 2c.

from $\Lambda = 5°$ to $\Lambda = 20°$. What happens for sweep angles larger than 30° (slope amplitudes decrease, then increase, and then increase again) can be interpreted as the effect of a complex interaction between streamwise and cross-flow unstable waves.

Figure 5-26 shows the values of N_1 and N_2 at transition for the different sweeps. Assuming that there is a critical cross-flow amplification analog to the critical amplification factor in two-dimensional flows, if transition were due to cross-flow instabilities at $\Lambda = 60°$ (which is the most likely candidate for cross-flow transition) then transition would also have to be caused by cross-flow instabilities at all the other sweep angles since they all have a value of N_2 at transition lower than that for $\Lambda = 60°$. However, it seems unlikely that transition at such a small sweep angle as 5° would be the result of unstable cross-flow disturbances. Therefore, the following hypothesis

seems again the most plausible: transition over the swept wing at this low Reynolds number is caused by the growth of unstable TS waves (just as it was for the un-swept wing), but the presence of even small cross-flow velocities destabilizes the laminar streamwise profile and accelerates transition. In other words, for intermediate sweep angles we are in the presence of a mixed transition.

Again, at this point it is not possible to determine at which critical cross-flow amplification factor transition can be assumed to occur, and hence it is even harder to determine which type of disturbance (TS or cross-flow waves) is eventually responsible for transition. However, for sweep angles of 30° and more, the value of N_1 at transition remains more or less constant close to 5.5, while transition location keeps moving upstream: this suggest that transition at large sweeps is primarily dominated by cross-flow disturbances. In spite of this, N_2 at transition keeps decreasing; one should remember at this point that cross-flow transition may not be characterized by solely the linear growth of disturbances—a simplification which has often be successful for TS-dominated transition.

5.3.5 Summary

Three interesting facts observed throughout the study of the effects of cross flow on transition are worth emphasizing once more. One is the saturation phenomena observed at large sweep angles: after "enough" cross-flow is present (a fuzzy threshold), the flow becomes somewhat insensitive to further increases, and the cross-flow stops being strongly influential even before the sweep angle becomes inefficient at generating cross-flow. This is seen in many of the curves which flatten-out for large values of Λ, *e.g.* maximum in H and transition location. A plausible explanation is that for moderate to large sweep angles transition is very strongly influenced (and even dominated) by the cross-flow instabilities.

Furthermore, the streamwise and cross-flow components cannot be decoupled from a stability point of view for intermediate sweep angles (roughly between $\Lambda = 10°$ and 30°) and the resulting mixed transition is due to the presence of strong non-linear interactions. Considering the two components independently is however possible for either very small or very large sweep angles. This is consistent with the high Reynolds number observations of Strokowsky and Orszag (1977)[1] and with the results of authors (e.g. Reshotko, 1994) who have successfully decoupled them for other flows.

[1] when the cross-flow is unstable, the boundary layer stability characteristics are very close to those of the cross-flow alone (*i.e.* irrespective of the streamwise flow); when the cross-flow is stable, the stability characteristics are essentially those of the streamwise profile; see details in Section 2.4

Finally, even a very small amount of cross-flow significantly affects transition, as evidenced by the significant differences between results at 0° and 10° sweep. This is not unexpected since transition and turbulence are highly non-linear processes, and the stability characteristics of boundary and shear layers are very sensitive to even small perturbation. An important practical conclusion is that, at these low Reynolds numbers in which transition takes place along a laminar separation bubble, a purely TS-wave based transition is very unlikely to be successful in real flow conditions since the free-stream will not be (nor stay) closely aligned with the chord-wise direction—and this misalignment will be more pronounced on instantaneous fields and with flapping vehicles for which the wing is not stationary.

Chapter 6

Conclusions

6.1 Summary and Contributions

The present work shows how the formation, and related transition to turbulence, of a laminar separation bubble (LSB) on an un-swept, rectangular, SD7003 infinite wing at 4° angle of attack and low Reynolds numbers can be predicted by means of an Implicit Large Eddy Simulation (ILES) using a Discontinuous Galerkin (DG) method with relatively coarse grids. In addition to being one of the first LES studies using DG and hence an important contribution to the advancement of numerical methods, attention is given to the boundary layer characteristics which had not yet been previously studied for this problem on the base of numerical simulations, thus contributing to the understanding of low Reynolds number flows and transition.

At a Reynolds number of 10,000, the flow is found to be essentially two-dimensional with no closed laminar separation bubble (LSB) formation since it lacks reattachment, and a periodic shedding of pairs of large counter-rotating vortices. For this flow, computations with 430,080 high-order nodes and polynomials of order $p = 3$ are sufficient, while two-dimensional simulations with as little as 44,000 high-order nodes provide a good estimate.

At the higher Reynolds numbers of 22,000 and 60,000, significant three-dimensional effects are present and an LSB is observed on the upper surface. In order to capture the main flow features, close to 1 million high-order nodes are required with $p = 3$ at $Re = 22,000$, while at $Re = 60,000$ about 1.8 million nodes and $p = 4$ are necessary. The study of transition that takes place along the LSB, through the boundary layer streamwise fluctuating pseudo-velocity profiles and the spatial growth of the amplification factor of disturbances, shows that transition is caused to unstable TS waves

and hence a natural transition. This observation of TS waves through numerical simulations has not been evidenced in other works.

Very little being known about the influence of cross-flow on transition at low Reynolds numbers, a study of the same wing configuration at various sweep angles is presented. By maintaining the chord-wise Reynolds number, angle of attack, and SD7003 geometry constant, the effects of cross-flow are clearly determined since the boundary and shear layer developments have a common two-dimensional equivalent boundary layer. In this way, if the cross-flow and streamwise effects were only linearly coupled, two-dimensional-equivalent curves for different sweep angles would collapse into a single line. This is not what is observed for intermediate sweep angles between 10° and 40°, and it is clearly demonstrated that—except at either very small and or large sweeps—the cross-flow effects *cannot* be considered independently of the streamwise evolution due to strong non-linear interactions that take place after the laminar boundary layer separates.

Two consequences of this finding are of great importance. First, a method which would predict low Reynolds number transition based on two separate models for streamwise and cross-flow amplifications would not be appropriate even for moderately swept wings. Both components need to be treated together, and a single transition equation applicable to swept wings would have to be devised by, for instance, including appropriate correlations to model the cross-flow effects on the streamwise boundary layer development and disturbance amplification. A step-based blending might be worth investigating since for very little cross-flow transition seems dominated by TS instabilities, and dominated by cross-flow disturbances when the cross-flow is sufficiently large.

Furthermore, even a relatively small amount of cross-flow present over a wing with 10° sweep significantly affects transition. In practical terms, this means that many real, low Reynolds number flows with an LSB see a mixed-type transition since the free-stream is unlikely to be closely aligned with the chord-wise direction. This misalignment is expected to be more pronounced on instantaneous fields and with flapping vehicles for which the wing is not stationary, and more so at lower than higher Reynolds numbers due to the low inertia of the flow. An important presumption to be adopted in the study of the flows relevant to MAVs and animal locomotion is thus that the type of transition (TS dominated, cross-flow dominated, or mixed) is *a priori* unknown.

6.2 Further Work

From a purely numerical standpoint, the question of how well the numerical dissipation in a DG method functions as a general implicit subgrid-scale model for ILES is still unclear, and the present work being the first to use DG for fully three-dimensional, unsteady ILES provides only a limited insight. How the intrinsic dissipation in DG behaves for other classes of flows, starting from the fundamental turbulence decay, needs to be investigated. Moreover, as with finite volume methods, other dissipative schemes for the inviscid fluxes are worth trying and could prove more or less effective depending on the particular flow being simulated.

In terms of deriving a model for separation-induced transition over un-swept wings, the next step is to couple the transition equation presented and tested here with the RANS Spalart-Allmaras model via its trip term. This could be done in a DG setting or with more established CFD techniques, even though the calibration of the model might vary depending on which numerical method is being used—in particular whether it is high or low order and whether it relies on numerical dissipation which is explicit (as with the filters used in finite differences) or implicit (as with finite-volume type techniques which tend to rely on some form of upwinding). The ultimate goal is of course to provide a transition model with general applicability (*i.e.* usable with a variety of numerical methods for a relatively large class of flows) which is affordable enough for use in design and everyday engineering computations.

With regards to the understanding of the cross-flow effects on transition, the sweep wing need to be be studied with higher spatial resolution in order to reveal more flow features and reduce the uncertainty of the trends observed in the average results, as well as validate or disprove some of the hypothesis presented. Furthermore, a more detailed variation of not only the sweep angle but also the Reynolds number and angle of attack is a preliminary step to deriving correlations necessary to model mixed transition. It might be then possible to modify the transition equation for the amplification of disturbances in order to take into account the effect of cross-flow.

Finally, MAVs benefit from flapping-type propulsion and lift generation because of the low Reynolds number flows involved. Understanding and predicting how the boundary layer develops and transitions over wings with heaving and/or peaching motions can be approached in the same manner as the wings studied here.

Appendix A

On the Dynamics of Turbulence

A.1 Length Scales

A turbulent flow is characterized by a continuous and broad range of length and time scales. The size of the largest eddies in a flow is represented by the *integral length scale*, ℓ, which is of the order of the width of the flow *e.g.* the diameter of the pipe or the width of the channel in Poiseuille flow.

At the other end of the spectrum, the fluid viscosity sets a lower limit on the size of the structures: below a certain size energy dissipation is the dominant process and velocity fluctuations are negligible. In other words, there is a size threshold below which velocity fluctuations are negligible compared to viscous damping – and by significant we mean that the characteristic time of the viscous dissipation is much smaller than the time scale of the motion.

The size of smallest turbulent eddies is characterized by the Kolmogorov scale, η_K, also known as the Kolmogorov microscale of length. An expression for η_K can be derived using dimensional analysis by assuming that the motion at very small scales is only governed by the dissipation rate per unit mass, ε, and the fluid viscosity, ν, namely

$$\eta_K = \left(\frac{\nu^3}{\varepsilon}\right)^{1/4} . \tag{A.1}$$

For these small eddies, dimensional analysis also provides a time scale, $\tau_K = (\nu/\varepsilon)^{1/2}$, and a velocity scale, $v_K = (\nu\varepsilon)^{1/4}$. These three scales for length, time, and velocity are known as Kolmogorov's microscales. To the Kolmogorov scale corresponds the

Kolmogorov dissipative wave number

$$k_K = \frac{1}{\eta_K} = \left(\frac{\varepsilon}{\nu^3}\right)^{1/4} .$$

The Reynolds number based on the Kolmogorov scales, $Re_K = \eta_K v_K/\nu$, is of order unity: the small-scale motions are very viscous.

A.2 Energy Transfer

On the one end, turbulence production is an increasing function of eddy size, and hence is dominated by the large scales (Tennekes and Lumley, 1972). Turbulent motions extract energy from the mean flow, which thus enters the turbulent energy spectrum at scales of sizes comparable to the integral length ℓ. On the other end, viscous dissipation of turbulent energy takes place at length scales comparable to the Kolmogorov scale η_K. Thus, turbulence dynamics involves the transfer of energy from the larger scales to the smaller scales of motion, down to the Kolmogorov scale where dissipation takes place. This is elegantly illustrated by Richardson (1922) in the riddle

> Big whorls have little whorls,
> Which feed on their velocity;
> And little whorls have lesser whorls,
> And so on to viscosity
> (in the molecular sense)

The downward transfer of energy from the larger to the smaller scales is called *energy cascade*, or *turbulent cascade*. Though energy generally is transferred towards smaller and smaller eddies (as in isotropic turbulence), the opposite transfer does take place in certain circumstances and is referred to as *backscatter*.

A first consequence of the energy cascade from large to small eddies is that the energy dissipation rate ε is related to the transfer of energy from the large eddies and hence governed by the large-scale motions, and this in spite the fact that dissipation takes place at small scales. Mathematically, since the large eddies have a characteristic velocity which is of the order of the turbulent fluctuations u', the dissipation rate is solely determined by the integral scale ℓ and by u', and hence dimensional analysis provides

$$\varepsilon \sim \frac{u'^3}{\ell} \tag{A.2}$$

or $\varepsilon = Au'^3/\ell$ where A is a constant which has been experimentally determined to be close to unity (Tennekes and Lumley, 1972).

A.3 The Energy Spectrum

Important insight into the dynamics of turbulence can be gained by working in wave-number space and considering isotropic turbulence, which is by definition invariant under rotation and translation transformations and hence has an average velocity of zero. The wave-number k characterizes scales of size $\eta = 2\pi/k$ (though sometimes the relation $\eta = 1/k$ is used). The variation of energy density, $E(k)$, as a function of k is known as the *energy spectrum*. The turbulent kinetic energy per unit mass, and total dissipation rate in the flow are thus given by, respectively,

$$KE = \int_0^\infty E(k)\, dk \quad , \quad \varepsilon = 2\nu \int_0^\infty k^2 E(k)\, dk \ .$$

The seminal work of Kolmogorov (1941a,b) provides a quantitative measure of how the energy density $E(k)$ varies. Kolmogorov first assumed that, at large Reynolds numbers, there exists a range of scales over which the motion statistics are only a function of the wave number k, of the dissipation rate ε, and of the viscosity ν. That is, the small scale motions are independent (*universal*) of the particularities of the large scales that characterize a given flow. This range of scales (or wave numbers) is referred as the *universal equilibrium range* and characterized by $k \gg 1/\ell$. In this range, the time scale of the motions is much smaller than the time scale of the large eddies, and hence equilibrium with the large scales can be maintained: energy is dissipated at the smallest scales as rapidly as it is produced by the large scales. This result if of great importance: the statistics of the small eddies is universal, *i.e.* the same in every turbulent flow (for whatever geometry, free-stream conditions, etc).

This universal equilibrium range can be divided into two sub-ranges. At the high end of the spectrum is the *dissipation range*, close to the Kolmogorov dissipative wave number, over which the energy decays exponentially as a result of motions being damped by viscosity. In this range, viscous effects dominate, and the time scale of dissipation is much smaller than the time that characterizes flow motions.

There exists an intermediate range of scales known as the *inertial range*. The assumption that defines this range of wave numbers, as made by Kolmogorov, is that inertial effects are dominant. Over this range, the energy transfer is insensitive to both the dynamics of the large, turbulence-producing scales on the one hand, and to

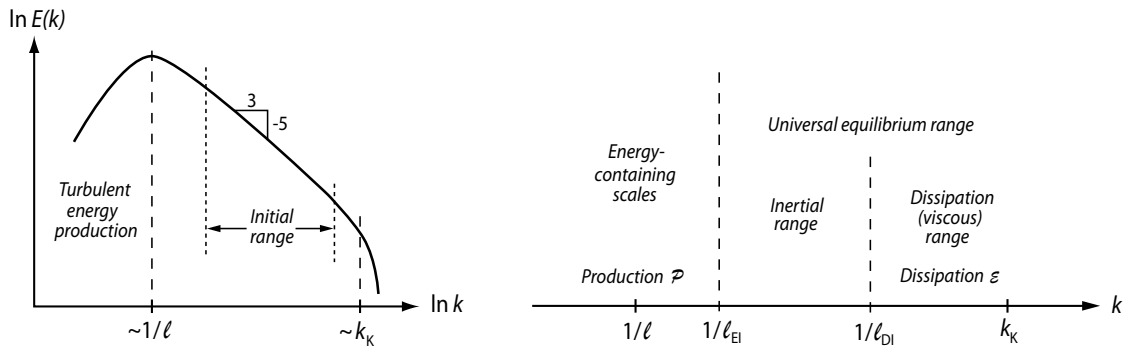

Figure A-1: Illustration of the energy spectrum of homogeneous turbulence (left), and of the different sub-ranges (right).

viscous effects on the other hand. Thus, for $1/\ell \ll k \ll k_K$, the energy spectrum is only a function of the wave number k and the dissipation rate ε. Dimensional analysis (E having units of m^3/s^2, ε units of m^2/s^3, and k units of $1/m$) then yields the power law for the energy spectrum in the inertial range

$$E(k) = C_K \varepsilon^{2/3} k^{-5/3} \ , \tag{A.3}$$

in which C_K is the Kolmogorov constant whose value in a three-dimensional spectra is close to 1.62 (Monon and Yaglom, 1975; Yeung and Zhou, 1997). The energy spectrum of turbulence can be seen (qualitatively) in Figure A-1, together with an illustration of the different ranges.

A very important consequence for turbulence modeling of the existence of an inertial sub-range is that the flow can be regarded as *self-similar* over the inertial range since the quantity $\gamma^{5/3} E(k)$ is invariant by the transformation $k \mapsto \gamma k$, *i.e.* $\gamma^{5/3} E(\gamma k) = E(k)$. This provides the justification behind the so-called scale-similarity subgrid scale models for LES (Meneveau and Katz, 2000).

It is important to note that the assumption of high Reynolds number ensures that $1/\ell \ll k_K$, and hence the existence of the universal equilibrium range over which statistics are independent of the large scale motions. Furthermore, this also guarantees the existence of wave numbers k such that $1/\ell \ll k \ll k_K$, and hence the existence of the inertial range (Batchelor, 1953).

Appendix B

Linear Stability Theory: Derivations

B.1 Disturbance Equations

The governing equations for a Newtonian fluid are the Navier-Stokes equations, which for an incompressible flow read

$$\frac{\partial u_i}{\partial x_i} = 0 \tag{B.1}$$

$$\frac{\partial u_i}{\partial t} + u_j \frac{\partial u_i}{\partial x_j} = -\frac{1}{\rho}\frac{\partial p}{\partial x_i} + \nu \nabla^2 u_i + f_i \quad \text{for} \quad i \in \{1,2,3\} \ , \tag{B.2}$$

in which u_i is the velocity component in the i^{th} direction x_i, p the pressure, ρ the fluid density assumed constant, f_i the body forces, and ∇^2 denotes the Laplacian operator $\partial^2/\partial x_i \partial x_i$.

The basic laminar flow of velocity components U_i and pressure P is assumed to be physical and hence to satisfy the equations of motion, such that

$$\frac{\partial U_i}{\partial x_i} = 0 \tag{B.3}$$

$$\frac{\partial U_i}{\partial t} + U_j \frac{\partial U_i}{\partial x_j} = -\frac{1}{\rho}\frac{\partial P}{\partial x_i} + \nu \nabla^2 U_i + f_i \quad \text{for} \quad i \in \{1,2,3\} \ . \tag{B.4}$$

A perturbation with velocity components u_i' and pressure p' is superimposed on this basic flow, that is

$$u_i = U_i + u_i' \quad , \quad p = P + p' \ . \tag{B.5}$$

Introducing this decomposition into the governing equations (B.1) and (B.2), and

subtracting the basic flow equations (B.3) and (B.4) to each of these respectively yields the disturbance equations

$$\frac{\partial u_i'}{\partial x_i} = 0 \tag{B.6}$$

$$\frac{\partial u_i'}{\partial t} + U_j \frac{\partial u_i'}{\partial x_j} + u_j' \frac{\partial U_i}{\partial x_j} + u_j' \frac{\partial u_i'}{\partial x_j} = -\frac{1}{\rho}\frac{\partial p}{\partial x_i} + \nu \nabla^2 u_i' \quad \text{for} \quad i \in \{1,2,3\} \,. \tag{B.7}$$

B.2 Small Perturbations for Parallel Flow

Since one can assume that the initial perturbations of a laminar flow are small and two-dimensional, the disturbance equations can be simplified by letting

$$u' = u_1'(x,n,t) \;\;,\;\; v' = u_2'(x,n,t) \;\;,\;\; w' = u_3' = 0 \;\;,\;\; p' = p'(x,n,t) \;, \tag{B.8}$$

where the subscript 1 denotes the streamwise (or chord-wise in the present work) x direction, the subscript 2 the transverse, or normal, n direction, and the subscript 3 the third direction (span-wise). Furthermore, a steady *parallel* basic flow is assumed, that is

$$U = U_1(n) \;\;,\;\; V = U_2 = 0 \;\;,\;\; W = U_3 = 0 \;\;,\;\; P = P(x,n) \;. \tag{B.9}$$

The basic pressure P remains a function of the streamwise direction x since the flow is driven by the pressure gradient $\partial P/\partial x$.

The parallel flow assumption is exact for fully developed flows inside ducts of constant cross-section (channel flow). It is a good approximation for boundary layers in which x-derivatives are negligible in front of n-derivatives.

Introducing the forms (B.8) and (B.9) into the disturbance equations (B.6) and (B.7) for $i = 1, 2$, and neglecting quadratic terms in the perturbations, gives the small perturbation equations for parallel flows

$$\frac{\partial u'}{\partial x} + \frac{\partial v'}{\partial n} = 0 \tag{B.10}$$

$$\frac{\partial u'}{\partial t} + U\frac{\partial u'}{\partial x} + v'\frac{\partial U}{\partial n} = -\frac{1}{\rho}\frac{\partial p'}{\partial x} + \nu \nabla^2 u' \tag{B.11}$$

$$\frac{\partial v'}{\partial t} + U\frac{\partial v'}{\partial x} = -\frac{1}{\rho}\frac{\partial p'}{\partial n} + \nu \nabla^2 v' \;. \tag{B.12}$$

These constitute three equations in three unknowns u', v', p', for a known basic flow $U(n)$. The pressure disturbance term can be eliminated by taking the x-derivative of the n-momentum (B.11) and the n-derivative of the x-momentum (B.12), subtracting

the resulting relations to eliminate the terms $\partial^2 p'/\partial x \partial n$, and making use of continuity (B.10), to obtain

$$\frac{\partial}{\partial t}\left(\frac{\partial u'}{\partial n} - \frac{\partial v'}{\partial x}\right) + U\frac{\partial}{\partial x}\left(\frac{\partial u'}{\partial n} - \frac{\partial v'}{\partial x}\right) + v'\frac{\partial^2 U}{\partial n^2} = \nu\nabla^2\left(\frac{\partial u'}{\partial n} - \frac{\partial v'}{\partial x}\right) \tag{B.13}$$

which together with the continuity equation (B.10) forms a system of two equations that needs to be solved for the two perturbation velocities u', v'.

Note that this is nothing but the convection-diffusion equation governing the perturbation in vorticity $\omega' = \partial v'/x - \partial u'/n$,

$$\frac{\partial \omega'}{\partial t} + U\frac{\partial \omega'}{\partial x} = v'\frac{\partial^2 U}{\partial n^2} + \nu\nabla^2\omega' \,,$$

where the source term (first term on the right-hand-side) accounts for the vorticity generated by the gradient in U.

B.3 The Orr-Sommerfeld Equation

In order to automatically satisfy the continuity equation (B.10), it is useful to introduce a perturbation stream function $\psi(x, n, t)$ such that

$$u' = \frac{\partial \psi}{\partial n} \quad , \quad v' = -\frac{\partial \psi}{\partial x} \,. \tag{B.14}$$

The linear, homogeneous, system of equations can be solved using the method of separation of variables and hence we assume that the perturbation on the basic flow is a linear combination of independent modes, with each mode propagating with time in the streamwise x direction. Thus, we introduce a trial solution for the stream function that is made up of a single of these modes, that is

$$\psi(x, n, t) = \phi(n)\, e^{i(\alpha x - \omega t)} \,, \tag{B.15}$$

and then any arbitrary perturbation can be decomposed into such Fourier modes. Here $\phi(n)$ is the eignefunction consistent with the parallel flow assumption and hence only a function of n.

Using the perturbation stream function definition (B.14) and form (B.15) gives

$$\frac{\partial u'}{\partial n} - \frac{\partial v'}{\partial x} = \frac{\partial}{\partial n}\left[\phi' e^{i(\alpha x - \omega t)}\right] - \frac{\partial}{\partial x}\left[-\phi\, i\, \alpha e^{i(\alpha x - \omega t)}\right] = \left(\phi'' - \alpha^2\phi\right) e^{i(\alpha x - \omega t)} \,,$$

where the prime on ϕ denotes the derivative with respect to n. This can finally be introduced into (B.13), and simplified using the fact that $e^{i(\alpha x-\omega t)} \neq 0$, $\alpha \neq 0$, to obtain the dimensional form of the Orr-Sommerfeld equation

$$(U-c)\left(\phi''-\alpha^2\phi\right)-U''\phi=-\frac{i}{\alpha}\nu\left(\phi''''-2\alpha^2\phi''+\alpha^4\phi\right) \ . \tag{B.16}$$

Non-dimensionalization is carried out by taking the boundary layer edge velocity U_e as the characteristic velocity, and some measure of the boundary layer thickness d as the characteristic length (usually the displacement thickness δ^*), such that the characteristic Reynolds number is

$$Re=\frac{U_e d}{\nu} \tag{B.17}$$

and the Orr-Sommerfeld equation in dimensionless form reads

$$(U-c)\left(\phi''-\alpha^2\phi\right)-U''\phi=-\frac{i}{\alpha Re}\left(\phi''''-2\alpha^2\phi''+\alpha^4\phi\right) \ . \tag{B.18}$$

This equation was derived by Orr (1907) and Sommerfeld (1908) and is the starting point of the stability theory of laminar parallel flows. Together with its homogeneous boundary conditions it forms an eigenvalue problem, with parameters α, c, Re, and eigenfunctions $\phi(n)$. Solving the stability problem corresponds to finding the solutions of this equation and thus determining whether the amplification factor ω_i is positive or negative, that is whether the perturbations are amplified (unstable basic flow) or damped (stable basic flow).

The corresponding boundary conditions for a boundary layer are given by the no-slip condition at the wall located at $n = 0$, and the vanishing of disturbances infinitely far from the wall. Both of these conditions translate on vanishing perturbation velocities, and give $\phi = 0$, $\phi' = 0$ both at the wall ($n = 0$) and far from it ($n \to \infty$).

Appendix C

LES: Further Considerations

C.1 Filtered Equations

Mathematically, the distinction between resolved and un-resolved (subgrid) scales can be made through the application of a spatial filter, an approach first proposed by Leonard (1974). Let us consider a conservative law of the form

$$\frac{\partial u}{\partial t} + \nabla \cdot F(u) = 0 \tag{C.1}$$

for some non-linear flux function $F(u)$. Let $\overline{u}$ be the filtered solution, that is

$$\overline{u}\,(\vec{x}, t) = \int u(\vec{x'}, t)\, G(\Delta, \vec{x}, \vec{x'})\, d\vec{x'} \tag{C.2}$$

where $G(\Delta, \vec{x}, \vec{x'})$ is the filter kernel which defines the numerical method. It has a characteristic length Δ (also known as filter width) which provides the cut-off between large eddies of size larger than Δ, and subgrid eddies of size smaller than Δ. Filtering the conservation equation (C.1) gives

$$\overline{\frac{\partial u}{\partial t}} + \overline{\nabla \cdot F(u)} = 0\ .$$

For filter kernels that commute with respect to time and space derivatives, and that are normalized such that

$$\int G(\Delta, \vec{x}, \vec{x'})\, d\vec{x'} = 1$$

we then have

$$\frac{\partial \overline{u}}{\partial t} + \nabla \cdot \overline{F(u)} = 0$$

and the closure problem arrises due to the fact that the filtered non-linear flux $\overline{F(u)}$ cannot be expressed in terms of the filtered solution $\overline{u}$ that is sought through the numerical procedure. It is then common to re-write the above as

$$\frac{\partial \overline{u}}{\partial t} + \nabla \cdot F(\overline{u}) = \nabla \cdot F^{(LES)} \tag{C.3}$$

where

$$F^{(LES)} = F(\overline{u}) - \overline{F(u)} \tag{C.4}$$

is the subgrid scale tensor that needs to be modeled. When F is linear as in the continuity equation, $F^{(LES)} = 0$ and no modeling is required: filtered and unfiltered equations are equivalent.

Thus, the closure problem arises from the non-linearity of the governing equations, and hence when solving the Navier-Stokes equations $F^{(LES)}$ in (C.3) contains the terms related to the inviscid fluxes (the viscous fluxes being linear). In incompressible flow, the subgrid scale tensor for the momentum equations is

$$F_{ij}^{(LES)} = -\rho \left(\overline{u_i u_j} - \overline{u_i}\ \overline{u_j} \right) \ .$$

At this point it is important to mention that the constraint that the filter kernel G must commute with respect to time and space derivatives is unrealistic for bounded domains for which the cut-off length Δ must decrease as the boundary of the domain is approached. When a non-uniform grid is used (as is often the case), non-homogeneous filters have to be used to mathematically represent the LES approach. Several authors have risen the question of whether a theoretical framework of LES on uniform grids can at all be extended to non-uniform grids. The reader is referred to Ghosal (1999) and Sagaut (2007) for more details concerning this problem and possible solutions.

C.2 Sources of Error

Insight into the limitations of explicit LES models can be gained by following the procedure described by Sagaut (2007). We look at the error in the numerical solution in any arbitrary norm, $e(h_r, \eta) = ||u - u_h||$, as resulting from three sources of errors

$$e(h_r, \eta) = e_{\Pi}(h_r, \eta) + e_h(h_r, \eta) + e_r(h_r, \eta) \, . \tag{C.5}$$

Any error is a function of both the resolution (represented by the measure h_r of the resolution of the numerical method) and of the scales that are not resolved (represented by the Kolmogorov scale η).

A first source of error is due to the use of a finite number of degrees of freedom to approximate the exact continuous solution; it is denoted e_Π and is called projection error. No discrete approximation can reduce this error to zero. A second source is the numerical error e_h which results from the approximation of time and space derivatives using numerical schemes; by consistency, this error tends to vanish as h_r tends to zero. The third source of error is the resolution error e_r which accounts for the fact that not all relevant scales are resolved in an LES; in a DNS, $h_r \approx \eta$ and e_r vanishes. The explicit LES approach aims at reducing the resolution error e_r by employing a subgrid-scale (SGS) model to account for the unresolved scales.

C.3 Explicit Subgrid-Scale Models

The LES approach was first introduced in the 1960s by the meteorologist Smagorinsky (1963) who proposed an eddy viscosity subgrid-scale model which is still widely used today due to its simplicity and success for industrial applications. As in all eddy-viscosity models whether for LES or RANS, Smagorinsky's model is based on the idea that the main effect of turbulence is to drain energy from the large scales, that is to drive the kinetic energy cascade. Through the use of Boussinesq's assumption, the subgrid scale tensor is then modeled as

$$F^{(LES)} = 2\,\nu_t\,\overline{S}$$

is employed, where ν_t is the eddy viscosity that needs to be modeled, and

$$\overline{S} \;=\; \left[\nabla\overline{u} + (\nabla\overline{u})^T\right]/2$$

is the rate of strain tensor of the resolved scales. The Smagorinsky model computes the eddy viscosity as

$$\nu_t = (C_S\;\Delta)^2\,|\overline{S}|$$

were $|\overline{S}| = \sqrt{\overline{S}_{ij}\overline{S}_{ij}}$, Δ is the grid spacing or filter width, and C_S is the Smagorinsky constant whose value is close to 0.2 in isotropic turbulence.

The main deficiencies of the Smagorinsky model are that (1) it requires the input of a model constant C_S, (2) it yields incorrect asymptotic behavior near walls and in

laminar flow, (3) does not allow for energy backscatter from the subgrid scales to the resolved eddies, and (4) it assumes that the principal axes of the subgrid-scale tensor are aligned with those of the resolved strain rate tensor.

Issue (2) is easily resolved by the used of *e.g.* a van Driest damping function as proposed by Lilly (1967) such that

$$C_S^2 = C_{S_0}^2 \left[1 - \exp\left(-y^+/A^+\right)\right]^2$$

where C_{S_0} is the undamped Smagorinsky constant, $y^+ = y\, u_\tau/\nu$ is the distance to the wall in wall units, and A^+ characterizes the damping magnitude with 25 a commonly used value.

The dynamic model originally proposed by Germano et al. (1991) addresses issue (1) by determining the model constant dynamically during the simulation through the assumption of scale invariance. It is thus a self-similarity model, and requires the cut-off level to be within the inertial sub-range as explained previously. The idea is to compute the Smagorinsky coefficient "by imposing that two different large eddy representations of a turbulent flow: the computed large eddy simulation and a tested large eddy simulation at a higher level, are equivalent from a statistical point of view" (Germano et al., 1991). The computed fields are filtered using a test filter whose width is larger than the mesh filter width Δ, commonly set to 2Δ. It is then assumed that the model constant is the same for the original filter and for the test filter. This approach also addresses issue (3) since it can result in negative values of C_S^2 and hence allows backscatter through a negative ν_t.

Another significant improvement in subgrid-scale modeling is provided by the scale-similarity model proposed by Bardina et al. (1980). The approach relies on the assumption that "the important interactions between the resolved and unresolved scales involve the smallest eddies of the former and the largest eddies of the latter, *i.e.* eddies that are a little larger or a little smaller than the length scale, Δ, associated with the filter". Thus, the entire structure of the field at the subgrid-scales is assumed to be similar to that of the large scales. Combining this approach with the Smagorinsky model yields a mixed model, and it resolves the problem of backscatter (issue (3)) while not assuming alignment between subgrid-scale stress and resolved strain rate (issue (4)).

Much effort has been put for a number of years on deriving better subgrid-scale models in particular in the 1990s (see for instance reviews by Lesieur and Métais, 1996; Meneveau and Katz, 2000), with dynamic mixed models providing results that

are closest to DNS data. The conclusion of Spalart (2000) that "there is little to gain by refining the SGS [subrgrid scale] models" is shared by many authors (*e.g.* Fureby et al., 1997).

All the models discussed here belong to the class of *functional* subgrid-scale models: they aim at reproducing the effects of the unresolved scales on the resolved field. Another approach is that of *structural* models which aim at directly predicting the subgrid scales. The interested reader is referred to Domaradzki and Adams (2002) and to Sagaut (2005) for a review of this other class of models.

C.4 Physical Justifications of ILES

Boris (2007) gives arguments as why the MILES approach (and other ILES) should work, and details five considerations which can be summarized as follows.

- "As the wavelength decreases, the [Kolmogorov energy] spectrum drops off so quickly that the shortest neglected scale lengths do not contain very much of the energy of the flow". Thus, most of the energy resides in eddies that can be resolved with the computational power of today's supercomputers.

- On the other hand, the energy decay at increasingly large wave number, $k^{-5/3}$, is "not too steep", such that small scales "mix large-scale inhomogeneities as fast as the large eddies can produce them", and energy is quickly dissipated as heat thus ensuring energy conservation. This was explained in detail in Section A.3.

- Furthermore, "the turbulent kinetic energy being transferred by the inertial-range cascade passes through all the intervening local scales to short wavelength where it is eventually dissipated"; a consequence of this is that "virtually all of the energy extraction from a given scale occurs as a result of interactions with eddies less than an order of magnitude smaller". Hence, "the small scales are not very important dynamically because the cascade of energy from large scales to short scales moves through the intervening scales".

- "There are only few features of the flow that are important at scales as small as η_K or even 10 times larger", and hence the Kolmogorov scale is "relatively unimportant dynamically because the turbulence energy has already been dissipated at larger wavelengths before it can reach η_K."

- Finally, nonlinear monotone fluid dynamic algorithms "properly connect the flow at the smallest computed scales to the flow at the smaller unresolved scales" and hence "the computed solution is expected to be reliable down to the small resolved scales" in spite of these being of size similar to the grid resolution, hence necessarily under-resolved and subject to Gibbs oscillations in the presence of sharp gradients. In particular, enforcing certain physical requirements on convection algorithms (*e.g.* conservation property: total quantity of a convected variable is unchanged by the convection algorithm when integrated over the domain) "seem to sufficiently constrain the numerical solution that resolved kinetic energy cascades off the grid into heat in a physically reasonable way." As a consequence, "the dissipation in the algorithm properly connects the large, energy-containing scales to the unresolved subgrid scales of motion", while we can rely on such methods "to compute the large scales correctly without significant contamination from numerical errors at the grid scale and from the segment of the physical inertial range that has been truncated."

The first three considerations are linked to the energy cascade in the inertial range as described by Kolmogorov's theory (see Appendix A), and thus underline the importance that the cut-off level of LES be in this range. If the cut-off is close or above k_K, then we are performing a DNS. On the other hand, if the cut-off is at a wave number smaller than the inertial range, nothing warranties that the energy contained in the unresolved scales is small enough and that all energy-producing eddies are accounted for.

The last consideration is very important, since one cannot expect to accurately resolve features that are, by the grid coarseness, necessarily under-resolved, but one can reasonably demand that resolved features be simulated accurately. In other words, the algorithm is to "do minimal damage to the larger wavelengths while still incorporating, at least qualitatively, most of the local and global effects of the unresolved turbulence one expects of a Large Eddy Simulation" (Boris, 1990) which is precisely what ILES certain methods have been found to do.

C.5 Mathematical Justifications of ILES

The idea of Modified Equation Analysis (MEA) is to consider the form that the governing partial differential equations (PDEs) take when the volume of integration is finite, as opposed to the assumption of an infinitely small volume that is used in the

derivation of the PDEs from the control volume equations. The finite volume PDEs correspond to the governing equations plus a term that is a function of the volume size and time step. These are referred to as *finite-volume equations* and the additional terms are called *finite-volume corrections* (Grinstein et al., 2007c). Once the finite-volume equations have been derived, MEA can be used to generate the PDEs "whose [exact] solution closely approximates the solution of a numerical algorithm" (see also Margolin and Rider, 2007; Fureby and Grinstein, 1999, 2002; Rider and Margolin, 2003).

In the case of the Navier-Stokes equations, the finite-scale corrections can be written as the divergence of a symmetric tensor which can be viewed as a subgrid-scale tensor that belongs to the class of similarity models (Grinstein et al., 2007c). As mentioned previously, this type of models have been successfully used to predict the dynamics of turbulent flows.

Thus, an important feature that a numerical algorithm must have in order to be suited for ILES is that a self-similar term must be present in the MEA; this term directly results from the use of a finite-volume representation (Grinstein et al., 2007c). Another important feature is that sufficient dissipation is needed to regularize the solution similarly to how a subgrid-scale model does it. The presence of a minimum amount of dissipation ensures that the solution is physically plausible, and is referred to as the entropy condition.

Only monotone algorithms have been mathematically proved to function as implicit subgrid-scales models, but it remains unclear whether monotonicity is an absolute requirement for an ILES algorithm, or whether a weaker property would suffice (Grinstein, 2007). The ILES approach was originally developed with finite-volume methods, and the unresolved scales were accounted through the use of a non-oscillatory finite-volume method (NFV), such as a total variation diminishing (TVD) scheme.

Mathematically, if the solution $u_j^{(n+1)}$ at point j is obtained from the solution $u^{(n)}$ at the previous step through a relation of the form

$$u_j^{(n+1)} = H\left(u_{j-l}^{(n)}, ..., u_j^{(n)}, ..., u_{j+r}^{(n)}\right),$$

the scheme is called *monotone* when $\partial H/\partial u_i \geq 0$ for all points $i = j-l, ..., j+r$. A monotone numerical algorithm does not lead to un-physical oscillations (Gibbs phenomenon) in the numerical solution which can appear due to the finite resolution. The appearance of this type of oscillations is a result of the finite resolution. The

term *monotonicity preserving* is used to indicate that new oscillations are not created near propagating discontinuities that have a monotone initial condition. Note that all monotone algorithms are TVD, and that all TVD schemes are monotonicity preserving.

The *total variation* of a continuous function u is

$$TV(u) = \int \left| \frac{\partial u}{\partial x} \right| dx$$

and is a measure of how much the function fluctuates with x. For a discontinuous function, the total variation at a given step n is given by

$$TV(u^{(n)}) = \sum_j \left| u_{j+1}^{(n)} - u_j^{(n)} \right| .$$

A numerical algorithm is called *total variation diminishing* (TVD) if the total variation of the solution at step $n+1$, $TV(u^{(n+1)})$, is not larger than the total variation $TV(u^{(n)})$ at the previous step, that is

$$TV(u^{(n+1)}) \leq TV(u^{(n)}) .$$

This is an important property of a numerical scheme since, as Lax (1973) showed, the total variation of any physical (entropy satisfying) solution is a non-increasing function of time, that is $d\,[TV(u)]/dt \leq 0$. Boris and Book (1973); Sweby (1985) showed that high-order TVD schemes can be derived by using a flux limiter approach that reduces the order of the scheme near discontinuities which are necessarily under-resolved.

Other classes schemes have been successfully used in ILES (for instance the one of the present work), but a strict mathematical proof of their suitability is often impossible.

References

Abid, R. (1993). Evaluation of two-equation turbulence models for predicting transitional flows. *Int. J. Engng Sci.*, 31:831–840.

Abu-Ghannam, B. and Shaw, R. (1980). Natural transition of boundary layers — the effects of turbulence, pressure gradient, and flow history. *Journal of Mechanical Engineering Science*, 22(5):213–228.

Alam, M. and Sandham, N. (2000). Direct Numerical Simulation of 'short' laminar separation bubbles with turbulent reattachment. *Journal of Fluid Mechanics*, 41:1–28.

Alexander, R. (1977). Diagonally Implicit Runge-Kutta methods for stiff O.D.E.'s. *SIAM J. Numer. Anal.*, 14(6):1006–1021.

Arnal, D. (1994). Predictions based on linear theory. In *AGARD Report No. 793*.

Bardina, J., Ferziger, J., and Reynolds, W. (1980). Improved subgrid scale models for Large Eddy Simulations. In *13th Fluid and Plasma Dynamics Conference, Snowmass, Colo., July 14-16, 1980, AIAA 80-1357*.

Bassi, F., Crivellini, A., Rebay, S., and Savini, M. (2005). Discontinuous Galerkin solution of the Reynolds-averaged Navier-Stokes and $k-\omega$ turbulence model equations. *Computers and Fluids*, 34:507–540.

Bassi, F. and Rebay, S. (1997). A high-order accurate discontinuous finite element method for the numerical solution of the compressible Navier-Stokes equations. *Journal of Computational Physics*, 131(2):267–279.

Bassi, F. and Rebay, S. (2000). GMRES discontinuous Galerkin solution of the compressible Navier-Stokes equations. In *Discontinuous Galerkin methods, theory, computation and applications*, volume 11 of *Lecture notes in computational science and eigineering. First International Symposium on Discontinuous Galerkin Methods, May 24–26, 1999, Newport, RI, USA*. Springer-Verlag.

Batchelor, G. (1953). *The Theory of Homogeneous Turbulence*. Cambridge University Press.

Boris, J. (1990). On Large Eddy Simulation using subgrid turbulence models. In Lumley, J., editor, *Whither Turbulence? Turbulence at the Crossroads*, pages 344–353. Springer-Verlag, New York.

Boris, J. (2007). More for LES: A Brief Historical Perspective of MILES. In Grinstein, F., Margolin, L., and Rider, W., editors, *Implicit Large-Eddy Simulation: computing turbulent flow dynamics*, pages 9–38. Cambridge University Press, New-York, NY, USA, 2007.

Boris, J. and Book, D. (1973). Flux-corrected transport i. shasta, a fluid transport algorithm that works. *Journal of Computational Physics*, 11:38–69.

Cebeci, T. (1989). Essential ingredients of a method for low Reynolds number airfoils. *AIAA Journal*, 27(12):1680–1688.

Cebeci, T. (2004). *Stability and Transition: Theory and Application*. Springer.

Chavent, G. and Cockburn, B. (1989). The local projection p^0-p^1-discontinuous Galerkin finite element method for scalar conservation laws. *Mathematical Modelling and Numerical Analysis*, 23(4):565–592.

Cockburn, B., Dong, B., and Guzman, J. (2008). A superconvergent LDG-Hybridizable Galerkin method for second-order elliptic problems. *Mathematics of Computations*, 77:1887–1916.

Cockburn, B., Gopalakrishnan, J., and Lazarov, R. (2009). Unified hybridization for discontinuous Galerki, mixed and continuous Galerkin methods for second-order elliptic problems. *SIAM J. Numer. Anal.*, 47(2):1319–1365.

Cockburn, B. and Shu, C.-W. (1991). The Runge-Kutta local projection p^1-discontinuous Galerkin method for scalar conservation laws. *RAIRE Modél. Math. Anal. Numé.*, 25:337–361.

Cockburn, B. and Shu, C.-W. (1998). The local discontinuous Galerkin method for time-dependent convection-diffusion systems. *SIAM J. Numer. Anal.*, 35(6):2440–2463.

Cockburn, B. and Shu, C.-W. (2001). Runge-Kutta discontinuous Galerkin methods for convection-dominated problems. *Journal of Scientific Computing*, 16(3):173–261.

Collis, S. S. (2002). The DG/VMS method for unified turbulence simulation. In *32nd AIAA Fluid Dynamics Conference and Exhibit, June 24-26, 2002, St. Louis, MO, AIAA-2002-3124*.

Dhawan, S. and Narasimha, R. (1958). Some properties of boundary layer flow during the transition from laminar to turbulent motion. *Journal of Fluid Mechanics*, 3:418–436.

Dini, P., Selig, M., and Maughmer, M. (1992). Simplified linear stability transition prediction method for separated boundary layers. *AIAA Journal*, 30(8):1953–1961.

Domaradzki, J. and Adams, N. (2002). Direct modeling of subgrid scales of turbulence in Large Eddy Simulations. *Journal of Turbulence*, 3:1–19.

Drazin, P. and Reed, W. (1981). *Hydrodynamic Stability*. Cambridge University Press.

Drela, M. (1995). Mises implementation of modified abu-ghannam/shaw criterion. *Dept. of Aeronautics and Astronautics, Massachusetts Institute of Technology, Cambridge, MA*.

Drela, M. (2002). *XFOIL Users Guide, Version 6.94*. MIT Aeronautics and Astronautics Department.

Drela, M. and Giles, M. (1987). Viscous-inviscid analysis of transonic and low Reynolds number airfoils. *AIAA Journal*, 25(10):1347–1355.

Drikakis, D., Marco, H., Grinstein, F., DeVore, C., Fureby, C., Liefvendahl, M., and Youngs, D. (2007). Numerics for ILES: Limiting Algorithms. In Grinstein, F., Margolin, L., and Rider, W., editors, *Implicit Large-Eddy Simulation: computing turbulent flow dynamics*, pages 94–129. Cambridge University Press, New-York, NY, USA, 2007.

Dubeif, Y. and Delcayre, F. (2000). On coherent-vortex identification in turbulence. *Journal of Turbulence*, 1(11):1–22.

Ekaterinaris, J. and Menter, F. (1994). Computation of separated and unsteady flows with one — and two — equation turbulence models. In *32nd AIAA Aerospace Sciences Meeting and Exhibit, Jan. 10-13, 1994, Reno, NV, AIAA-94-0190*.

Fureby, C. and Grinstein, F. (2002). Large-Eddy Simulation of high Reynolds-number free and wall bounded flows. *Journal of Computational Physics*, 181:68.

Fureby, C., Taylor, G., Weller, H., and Gosman, A. (1997). A comparative study of subgrid scale models in homogeneous isotropic turbulence. *Physics of Fluids*, 9(5):1416–1429.

Fureby, U. and Grinstein, F. (1999). Monotonically integrated Large Eddy Simulation of free shear flows. *AIAA Journal*, 37:544–556.

Galbraith, M. and Visbal, M. (2008). Implicit Large-Eddy Simulation of low Reynolds number flow past the SD7003 airfoil. In *46th AIAA Aerospace Sciences Meeting and Exhibit, Jan. 7-10, 2008, Reno, NV, AIAA-2008-225*.

Garmann, D. and Visbal, M. (2009). High-fidelity simulations of transitional flow over pitching airfoils. In *39th AIAA Fluid Dynamics Conference, June 22-25, 2009, San Antonio, TX, AIAA-2009-3693*.

Gaster, M. (1962). A note on the relation between temporally-increasing and spatially-increasing disturbances in hydrodynamic stability. *Journal of Fluid Mechanics*, 14:222–224.

Germano, M., Piomelli, U., Moin, P., and Cabot, W. (1991). A dynamic subgrid scale eddy viscosity model. *Physics of Fluids A*, 3(7):1760–1765.

Ghosal, S. (1996). An analysis of numerical errors in Large-Eddy Simulations of turbulence. *J. Comput. Phys.*, 125:187–206.

Ghosal, S. (1999). Mathematical and physical constraints on Large-Eddy Simulation of turbulence. *AIAA Journal*, 37(4):425–433.

Gleyzes, C., Cousteix, J., and Bonnet, J. (1985). Theoretical and experimental study of low Reynolds number transition separation bubbles. In *Conference in Low Reynolds Number Airfoil Aerodynamics, University of Notre Dame, Notre Dame, IN*.

Gregory, N., Stuart, J., and Walker, W. (1955). On the stability of three-dimensional boundary layers with applications to the flow due to a rotating disk. *Phil. Trans. Roy. Soc.*, A 248:155–199.

Grinstein, F. (2007). Vortex Dynamics and Transition to Turbulence in Free Shear Flows. In Grinstein, F., Margolin, L., and Rider, W., editors, *Implicit Large-Eddy Simulation: computing turbulent flow dynamics*, pages 265–291. Cambridge University Press, New-York, NY, USA, 2007.

Grinstein, F., Margolin, L., and Rider, W., editors (2007a). *Implicit Large-Eddy Simulation: computing turbulent flow dynamics*. Cambridge University Press, New-York, NY, USA, 2007.

Grinstein, F., Margolin, L., and Rider, W. (2007b). Introduction. In Grinstein, F., Margolin, L., and Rider, W., editors, *Implicit Large-Eddy Simulation: computing turbulent flow dynamics*, pages 1–6. Cambridge University Press, New-York, NY, USA, 2007.

Grinstein, F., Margolin, L., and Rider, W. (2007c). A Rationale for Implicit LES. In Grinstein, F., Margolin, L., and Rider, W., editors, *Implicit Large-Eddy Simulation: computing turbulent flow dynamics*, pages 39–58. Cambridge University Press, New-York, NY, USA, 2007.

Hain, R., Kähler, C., and Radespiel, R. (2009). Dynamics of laminar separation bubbles at low-Reynolds-number aerofoils. *Journal of Fluid Mechanics*, 630:129–153.

Helmholtz, H. (1868). Über discontinuirliche Flüssigkeitsbewegungen. *Monats. Königl. Preuss. Akad. Wiss. berlin*, 23:215–228.

Herbert, T. (1988). Secondary instability of boundary layers. *Annual Review of Fluid Mechanics*, 20:487–526.

Hirt, C. (1969). Computer studies of time-dependent turbulent flows. *Physics of Fluids*, II:219–227.

Horton, H. (1967). A semi-empirical theory for the growth and bursting of laminar separation bubbles. *Aeronautical Research Council, Britain, Current Paper 1073.*

Ingen, J. V. (1956). Suggested semi-empirical method for the calculation of the boundary layer transition region. *Dept. of Aerospace Engineering, Rept. VTH-74, Delft University of Technology, Delft, the Netherlands.*

Jordinson, R. (1970). The flat plate boundary layer, Part 1: numerical integration of the orr-sommerfeld equation. *Journal of Fluid Mechanics*, 43:801–811.

Jordinson, R. (1971). Spectrum of eigenvalues of the Orr-Sommerfeld equation for Blasius flow. *Physics of Fluids*, 14:2535–2537.

Kaplan, R. (1964). The stability of laminar incompressible boundary layers in the presence of compliant boundaries. *Aeroelastic and Structures Research Lab. Report ASRL-TR 166-1, M.I.T., Cambridge, MA.*

Kelvin, L. (1871). Hydrokinetic solutions and observations. *Phil. Mag. (4)*, 42:362–377.

Kessler, M. (2007). Engineering application oriented discontinuous Galerkin methods. In *45th AIAA Aerospace Sciences Meeting and Exhibit, Jan. 8-11, 2007, Reno, NV, AIAA-2007-511.*

Kolmogorov, A. (1941a). Dissipation of energy in a locally isotropic turbulence. *USSR Academy of Sciences*, 32:16–18.

Kolmogorov, A. (1941b). The local structure of turbulence in incompressible viscous fluid for very large reynolds numbers. *USSR Academy of Sciences*, 30:299–303.

Krimmelbein, N. and Radespiel, R. (2009). Transition prediction for three-dimensional flows using parallel computation. *Computers and Fluids*, 38:121–136.

Krimmelbein, N., Radespiel, R., and Nebel, C. (2005). Numerical aspects of transition prediction for three-dimensional configurations. In *35th AIAA Fluid Dynamics Conference and Exhibit, June 6-9, 2005, Toronto, Ontario, Canada, AIAA-2005-4764.*

Krumbein, A. (2006). Automatic transition prediction and application to 3D wing configurations. In *Proc. of the 44th AIAA Aerospace Sciences Meeting and Exhibit, 9-12 Jan. 2006, Reno, Nevada, AIAA 2006-914.*

Kurtz, E. and Candrall, S. (1962). Computer-aided analysis of hydrodynamic stability. *J. Math. Phys.*, 44:264–279.

Lalin, K., Klausmeyer, S., Zickuhr, T., Vassberg, J., Wahls, R., Morrison, J., Brodersen, O. P., Rakowitz, M., Tinoco, E., and Godard, J.-L. (2005). Data summary from the second AIAA Computational Fluid Dynamics Drag Prediction Workshop. *Journal of Aircraft*, 42(5):1165–1178.

Landmann, B., Kessler, M., Wagner, S., and Krämer, E. (2006). A parallel discontinuous Galerkin code for the Navier-Stokes equations. In *44th AIAA Aerospace Sciences Meeting and Exhibit, Jan. 9-12, 2006, Reno, NV, AIAA-2006-111.*

Landmann, B., Kessler, M., Wagner, S., and Krämer, E. (2008). A parallel, high-order discontinuous Galerkin code for laminar and turbulent flows. *Computers and Fluids*, 37:427–438.

Lang, M., Rist, U., and Wagner, S. (2004). Investigations on controlled transition development in a laminar separation bubble by means of lda and pvi. *Experiments in Fluids*, 36(1):43–52.

Lax, P. (1973). *Hyperbolic systems of conservation laws.* SIAM, Philadelphia, PA.

LeBlanc, P., Blackwelder, R., and Liebeck, R. (1989). A comparison between boundary layer measurements in laminar separation bubble flow and linear stability theory calculations. In Mueller, T., editor, *Low Reynolds Number Aerodynamics: Proceedings of the Conference, Notre Dame, IN, 5-7 June 1989.* Lectures in Engineering No. 54, Springer-Verlag.

Leonard, A. (1974). Energy cascade in Large Eddy Simulation of turbulent fluid flows. *Advances in Geophysics*, 18:237–248.

Lesieur, M. and Métais, O. (1996). New trends in Large-Eddy Simulations of turbulence. *Annual Review of Fluid Mechanics*, 28:45–82.

Lesieur, M., Métais, O., and Comte, P. (2005). *Large-Eddy Simulation of turbulence.* Cambridge University Press.

Lian, Y. and Shyy, W. (2007). Laminar-turbulent transition of a low Reynolds number rigid or flexible airfoil. *AIAA Journal*, 45(7):1501–1513.

Lilly, D. (1967). The representation of small-scale turbulence in numerical simulation experiments. In Goldstine, H., editor, *IBM Scientific Computing Symposium on Environmental Sciences, Yorktown Heights, NY*, pages 195–210.

Mack, L. (1977a). Transition and laminar instability. *Jet Propulsion Laboratory Publication 77-15, Pasadena, CA.*

Mack, L. (1977b). Transition prediction and linear stability theory. In *AGARD Conference Proceedings, CP-224, AGARD, London, 1977.*

Margolin, L. and Rider, W. (2007). Numerical Regularization: The Numerical Analysis of Implicit Subgrid Models. In Grinstein, F., Margolin, L., and Rider, W., editors, *Implicit Large-Eddy Simulation: computing turbulent flow dynamics*, pages 195–221. Cambridge University Press, New-York, NY, USA, 2007.

Mayle, R. and Schulz, A. (1997). The path to predicting bypass transition. *Journal of Turbomachinery*, 119:405–411.

Meneveau, C. and Katz, J. (2000). Scale-invariance and turbulence models for Large-Eddy Simulation. *Annual Review of Fluid Mechanics*, 32:1–32.

Menter, F., Langtry, R., Likki, S., Suzen, Y., Huang, P., and Völker, S. (2006). A correlation-based transition model using local variables — part i: model formulation. *Journal of Turbomachinery*, 128:413–422.

Monon, A. and Yaglom, A. (1975). *Statistical Fluid Mechanics: Mechanics of Turbulence*. MIT Press, Cambridga, MA, USA.

Nebel, C., Radespiel, R., and Wolf, T. (2003). Transition prediction for 3D flows using a Reynolds-averaged Navier-Stokes code and N-factor methods. In *33rd AIAA Fluid Dynamics Conference and Exhibit, June 23-26, 2003, Orlando, FL, AIAA-2003-3593*.

Nguyen, N., Peraire, J., and Cockburn, B. (2009). An implicit high-order hybridizable discontinuous Galerkin method for linear convection-diffusion equations. *Journal of Computational Physics*, 228:3232–3254.

Nguyen, N., Persson, P., and Peraire, J. (2007). RANS solutions using high order discontinuous Galerkin methods. In *45th AIAA Aerospace Sciences Meeting and Exhibit, Jan. 8-11, 2007, Reno, NV, AIAA-2007-914*.

Nürnberger, D. and Greza, H. (2002). Numerical investigation of unsteady transitional flows in turbomachinery components based on a RANS approach. *Flow, Turbulence and Combustion*, 69:331–353.

Ol, M., McAuliffe, B., Hanff, E., Scholz, U., and Kahler, C. (2005). Comparison of laminar separation bubbles measurements on a low Reynolds number airfoil in three facilities. In *Proc. of the 35th Fluid Dynamics Conference and Exhibit, Toronto, Ontario, Canada, AIAA-2005-5149*.

Oliver, T. and Darmofal, D. (2009). Impact of turbulence model irregularity on high-order discretizations. In *47th AIAA Aerospace Sciences Meeting, Jan. 5-8, 2009, Orlando, FL, AIAA-2009-953*.

Orr, W. M. (1907). The stability or instability of the steady motions of a perfect liquid and of a viscous liquid. *Proceedings of the Royal Irish Academy Sect. A*, 27:9–138.

Owen, P. and Randall, D. (1952). Boundary layer transition on the swept wing. In *RAE TM Aero 277*.

Peraire, J. and Persson, P.-O. (2008). The Compact Discontinuous Galerkin (CDG) method for elliptic problems. *SIAM Journal of Scientific Computing*, 30(4):1806–1824.

Persson, P.-O. (2009). Scalable parallel Newton-Krylov solvers for Discontinuous Galerkin discretizations. In *Proc. of the 47th AIAA Aerospace Sciences Meeting and Exhibit, Reno, Nevada, AIAA-2009-606*.

Persson, P.-O. and Peraire, J. (2006). Sub-cell shock capturing for Discontinuous Galerkin methods. In *44th AIAA Aerospace Sciences Meeting and Exhibit, Jan. 9-12, 2006, Reno, NV, AIAA-2006-112*.

Persson, P.-O. and Peraire, J. (2008). Newton-GMRES preconditioning for Discontinuous Galerkin discretizations of the Navier-Stokes equations. *SIAM Journal of Scientific Computing*, 30(6):2709–2733.

Prandtl, L. (1921). Bemerkind über die Entstehung der Turbulenz. *Z. Angew. Math. Mech.*, 1:431–436.

Probst, A. and Radespiel, R. (2008). Implementation and extension of a near-wall Reynolds-stress model for application to aerodynamic flows on unstructured meshes. In *46th AIAA Aerospace Sciences Meeting and Exhibit, Jan. 7-10, 2008, Reno, NV, AIAA-2008-770*.

Qin, S., Zhuang, M., Visbal, M., Galbraith, M., Lian, Y., and Shyy, W. (2009). Local and global stability analysis on flows around a SD7003 airfoil. In *47th AIAA Aerospace Sciences Meeting, Jan. 5-8, 2009, Orlando, FL, AIAA-2009-1470*.

Radespiel, R., Graage, K., and Brodersen, O. (1991). Transition predictions using Reynolds-averaged Navier-Stokes and linear stability analysis methods. In *AIAA 22nd Fluid Dynamics, Plasma Dynamics and Laser Conference, June 24-26, 1991, Honolulu, HI, AIAA-91-1641*.

Radespiel, R., Windte, J., and Scholz, U. (2007). Numerical and experimental flow analysis of moving airfoils with laminar separation bubbles. *AIAA Journal*, 45(6):1346–1356.

Radespiel, R., Windte, J., and Scholz, U. (Jan. 2006.). Numerical and experimental flow analysis of moving airfoils with laminar separation bubbles. *AIAA Paper 2006-501*.

Ramakrishnan, S. and Collis, S. S. (2004). Multiscale modeling for turbulence simulation in complex geometries. In *42nd AIAA Aerospace Sciences Meeting and Exhibit, Jan. 5-8, 2004, Reno, NV, AIAA-2004-241*.

Rayleigh, L. (1879). On the stability of jets. *Proc. London Math. Soc.*, 10:4–13.

Rayleigh, L. (1880). On the stability, or instability, of certain fluid motions. *Proc. London Math. Soc.*, 11:57–70.

Reed, H. and Saric, W. (1989). Stability of three-dimensional boundary layers. *Annual Review of Fluid Mechanics*, 21:235–284.

Reed, H. and Saric, W. (1996). Linear stability theory applied to boundary layers. *Annual Review of Fluid Mechanics*, 28:389–428.

Reed, W. and Hill, T. (1973). Triangular mesh methods for the neutron transport equations. In *Tech. Rept. LA-UR-73-479, Los Alamos Scientific Laboratory.*

Reshotko, E. (1994). Boundary instability, transition and control. In *32nd AIAA Aerospace Sciences Meeting and Exhibit, Jan. 10-13, 1994, Reno, NV, AIAA-94-0001.*

Richardson, L. (1922). *Weather Prediction by Numerical Process.* Cambridge University Press.

Rider, W. and Margolin, L. (2003). From numerical analysis to implicit subgrid turbulence modeling. In *16th AIAA Computational Fluid Dynamics Conference, June 23-26, 2003, Orlando, FL, AIAA-2003-4101.*

Roe, P. L. (1981). Approximate riemann solvers, parameter vectors, and difference schemes. *J. Comput. Phys.*, 43(1):357–372.

Sagaut, P. (2005). *Large-Eddy Simulation for Incompressible Turbulence.* Springer, Berlin, 3rd edition.

Sagaut, P. (2007). Subgrid-Scale Modeling: Issues and Approaches. In Grinstein, F., Margolin, L., and Rider, W., editors, *Implicit Large-Eddy Simulation: computing turbulent flow dynamics*, pages 61–93. Cambridge University Press, New-York, NY, USA, 2007.

Saric, W., Reed, H., and Kerschen, E. (2002). Boundary-layer receptivity to freestream disturbances. *Annual Review of Fluid Mechanics*, 34:291–319.

Saric, W., Reed, H., and White, E. (2003). Stability and transition of three-dimensional boundary layers. *Annual Review of Fluid Mechanics*, 35:413–440.

Savill, A. (1993). Some recent progress in the turbulence modelling of by-pass transition. In So, R., Speziale, C., and Launder, B., editors, *Near-Wall Turbulent Flows.* Elsevier Science, New York, NY.

Schlichting, H. (1933). Zur Entstehung der Turbulenz bei der Plattenstromung. *Nachr. Ges. Wiss. Göttingen Math.-Phys. Kl. II*, pages 182–208.

Schlichting, H. and Gersten, K. (2000). *Boundary Layer Theory.* Springer.

Selig, M., Donovan, J., and Fraser, D. (1989). *Airfoils at low speeds*. Soartech 8, H.A. Stokely publisher, Virginia Beach, VA, USA.

Selig, M., Guglielmo, J., Broeren, A., and Giguere, P. (1995). *Summary of low-speed airfoil data*. Soartech Aero Publications, H.A. Stokely, Virginia Beach, VA, USA.

Sengupta, K. and Mashayek, F. (2007). Large-Eddy Simulation using a discontinuous Galerkin spectral element method. In *45th AIAA Aerospace Sciences Meeting and Exhibit, Jan. 8-11, 2007, Reno, NV, AIAA-2007-402*.

Shum, Y. and Marsden, D. (1994). Separation bubble model for low Reynolds number airfoil application. *Journal of Aircraft*, 31(4):761–766.

Shyy, W. (2008). *Aerodynamics of low Reynolds number flyers*. Cambridge University Press, New-York, NY, USA.

Smagorinsky, J. (1963). General circulation experiments with the primitive equations, part i: the basic experiments. *Monthy Weather Review*, 91(3):99–164.

Smith, A. and Gamberoni, N. (1956). Transition, pressure gradient, and stability theory. *Douglas Aircraft Co., Rept. ES 26388*.

Sommerfeld, A. (1908). Ein Beitrag zur hydrodynamischen Erklaerung der turbulenten Fluessigkeitsbewegungen. *Proceedings of the Fourth International Congress of Mathematics, Rome*, III:116–124.

Spalart, P. (2000). Strategies for turbulence modelling and simulations. *International Journal of Heat and Fluid Flow*, 21:252–263.

Spalart, P. (2009). Detached-eddy simulation. *Annual Review of Fluid Mechanics*, 41:181–202.

Spalart, P. and Allmaras, S. (1994). A one-equation turbulence model for aerodynamic flows. *Recherche Aérospatial (also AIAA Paper 92-0429)*, pages 5–21.

Steelant, J. and Dick, E. (1996). Modelling of bypass transition with conditioned Navier-Stokes equations coupled to an intermittency transport equation. *International Journal for Numerical Methods in Fluids*, 23:193–220.

Stock, H. (2002). Airfoil validation using coupled Navier-Stokes and e^n transition prediction method. *Journal of Aircraft*, 39(1):51–58.

Stock, H. and Haase, W. (1999). Feasibility study of e^n transition prediction in Navier-Stokes methods for airfoils. *AIAA Journal*, 37(10):1187–2066.

Strokowsky, A. and Orszag, S. (1977). Mass flow requirements for lfc wing design. In *AIAA Aircraft Systems and Technology Meeting, Seattle, WA, Aug. 22-24*.

Sweby, P. (1985). High resolution TVD schemes using flux limiters. In Engquist, Osher, and Somerville, editors, *Lectures in Applied Mathematics, Large-Scale Computations in Fluid Mechanics*, volume 22, pages 289–309. American Mathematical Society.

Tang, L. (2006). RANS simulation of a low-Reynolds-number airfoil aerodynamics. In *44th AIAA Aerospace Sciences Meeting and Exhibit, Jan. 9-12, 2006, Reno, NV, AIAA-2006-249*.

Tennekes, H. and Lumley, J. (1972). *A First Course in Turbulence*. MIT Press, Cambridga, MA, USA.

Tollmien, W. (1929). Über die Entstehung der Turbulenz. *Nachr. Ges. Wiss. Göttingen Math.-Phys. Kl. II*, pages 21–44.

Uranga, A., Persson, P.-O., Drela, M., and Peraire, J. (2009). Implicit Large Eddy Simulation of transitional flows over airfoils and wings. In *19th AIAA Computational Fluid Dynamics Conference, June 22-25, 2009, San Antonio, TX, AIAA-2009-4131*.

Uranga, A., Persson, P.-O., Drela, M., and Peraire, J. (2010). Implicit Large Eddy Simulation of transition to turbulence at low reynolds numbers using a Discontinuous Galerkin method. *International Journal for Numerical Methods in Engineering, accepted*.

Vassberg, J., Tinoco, E., Mani, M., Brodersen, O. P., Eisfeld, B., Wahls, R., Morrison, J., Zickuhr, T., Laflin, K., and Mavriplis, D. (2008). Abridged summary of the third AIAA Computational Fluid Dynamics Drag Prediction Workshop. *Journal of Aircraft*, 45(3):781–798.

Visbal, M. (2009). High-fidelity simulation of transitional flows past a plunging airfoil. In *47th AIAA Aerospace Sciences Meeting, Jan. 5-8, 2009, Orlando, FL, AIAA-2009-391*.

Visbal, M., Gordnier, R., and Galbraith, M. (2009). High-fidelity simulations of moving and flexible airfoils at low Reynolds numbers. *Experiments in Fluids*, 46:903–922.

Walters, D. and Leylek, J. (2004). A new model for boundary layer transition using a single-point RANS approach. *Journal of Turbomachinery*, 126:193–202.

Warren, E. and Hassan, H. (1998). Transition closure model for predicting transition onset. *Journal of Aircraft*, 35(5):769–775.

Wazzan, A., Okamura, T., and Smith, A. (1968). The stability of water flow over heated and cooled flat plates. *J. Heat Tansfer*, 90:109–114.

White, F. (1991). *Viscous Fluid Flow, 2nd edition*. McGraw-Hill.

Wilcox, D. (1994). Simulation of transition with a two-equation turbulence model. *AIAA Journal*, 32(2):247–255.

Windte, J. and Radespiel, R. (2008). Propulsive efficiency of a moving airfoil at transitional low Reynolds number. *AIAA Journal*, 46(9):2165–2177.

Xu, Z., Stanescu, D., and Naughton, J. (2007). Development of a spectral element dns/les method for turbulent flow simulations. In *5th Joint ASME/JSME Fluids Engineering Conference, FEDSM2007, San Diego, CA, July 30 - Aug. 2, 2007*.

Yeung, P. and Zhou, Y. (1997). On the universality of the Kolmogorov constant in numerical simulations of turbulence. *Physical Review E*, 56:1746–1752.

Yuan, W., Khalid, M., Windte, J., Scholz, U., and Radespiel, R. (2005). An investigation of low-Reynolds-number flows past airfoils. In *23rd AIAA Applied Aerodynamics Conference, June 6-9, 2005, Toronto, Canada, AIAA 2005-4607*.

Yuan, W., Khalid, M., Windte, J., Scholz, U., and Radespiel, R. (2007). Computational and experimental investigations of low-Reynolds-number flows past an aerofoil. *The Aeronautical Journal*, pages 17–29.

Zang, Y., Street, R., and Koseff, J. (1993). A dynamic mixed subgrid-scale model and its application to turbulent recirculating flows. *Physics of Fluids*, A5(12):3186–3196.

Zheng, X., Liu, C., Liu, F., and Yang, C. (1998). Turbulent transition simulation using the $k-\omega$ model. *International Journal for Numerical Methods in Engineering*, 42:907–926.